Nuclear Fission with Inertial Confinement

D. G. Koshkarev* and B. Yu. Sharkov

Institute for Theoretical and Experimental Physics, ul. Bol'shaya Cheremushkinskaya 25, Moscow, 117218 Russia
* e-mail: koshkarev@vitep1.itep.ru
Received February 27, 2002

The possibility of inducing an explosive fission reaction in a small amount of fissionable material by a heavy-ion beam from a high-power accelerator driver developed for bringing about fusion in deuterium–tritium cylindrical targets with direct burning is analyzed. The consequences of the use of this method in the nuclear power industry are discussed. © 2002 MAIK "Nauka/Interperiodica".

PACS numbers: 28.85.Ge; 52.58.Hm

1. When the density $\rho = m n_f$ of a fissionable material increases, neutrons are multiplied more efficiently, because the neutron path before multiplication is $\lambda_f = 1/(n_f \sigma_f)$, where n_f is the concentration of fissionable nuclei and σ_f is the fission cross section. For fast neutrons with energy $E \geq 1$ MeV, the fission cross section depends slightly on energy. Neglecting the distribution of neutrons over energies, we take $E \approx 2$ MeV and $\sigma_f \approx 2$ b (for ^{239}Pu). Thus, an increase in the density of a fissionable material leads to the decrease in the critical size as $\rho^{-1}(R_k \sim \lambda_f \sim 1/\rho)$ and in the corresponding critical mass as $\rho^{-2}(M_k \sim \rho \lambda_f^3 \sim \rho^{-2})$. In this paper, to obtain the sub-milligram critical mass of a fissionable material, we suggest that the fissionable material must be strongly compressed by an intense beam of heavy ions from a high-power accelerator driver [1].

2. On the implosion of cylindrical direct-driven targets in the scheme of heavy-ion inertial thermonuclear synthesis [2], the heavy "pusher" made from Au or Pb is accelerated to velocities $V_{\text{imp}} \geq 3 \times 10^7$ cm/s directed to the axis of the cylindrical target owing to the hydrodynamic pressure of the absorber matter heated by a heavy-ion beam. At the stagnation instant [maximum compression, when the pressure of the pusher is equal to the pressure of the compressed deuterium–tritium (DT) mixture], the pusher matter achieves the density $\rho \approx 10^3$ g/cm³. It is substantial that the accelerator driver energy of ~ 5 MJ is sufficient to provide a strongly compressed matter of mass $M \approx 1$ g in the quasi-isentropic compression regime. Thus, when the matter of a pusher for a thermonuclear target is replaced by a fissionable material, intense heavy-ion beams with realistic parameters can provide physical conditions for the explosive fission of a small amount of fissionable material.

3. In order to reduce the critical mass, the shock compression of a fissionable material by chemical explosives is ordinarily used. Previously, it was suggested that the ablative pressure created by a high-power laser can be used [3]. We emphasize that an intense heavy-ion beam has a number of advantages over other pulsed methods of obtaining the super compressed state of a matter from the viewpoint of the efficiency of transforming driver energy to the energy of the compressed shell of a target (so-called hydrodynamic efficiency). First, the energy of ions is converted to the energy of the heated pusher with almost 100% efficiency, in contrast to laser radiation, for which this efficiency is much lower (≤10%). Second, heavy-ion beams are more appropriate than, e.g., laser radiation for the realization of the regime of so-called shockless compression [4]. Upon shockless compression, a matter is virtually not heated (entropy almost does not increase in this process) and the compression proceeds with minimum energy expenditure. Therefore, as compared to a laser, the "cold" compression of large masses of a heavy matter to comparable densities requires a considerably lower of energy expenditure.

4. The equation of neutron balance for the sphere of volume V and radius R can be written in the simplified form

$$\frac{d \int n \, dV}{dt} = \mu \sigma_f n_f \int n \nu \, dV - \frac{1}{4} \int n \nu \, dS, \qquad (1)$$

where t is time, n is the neutron density averaged over the sphere, ν is the mean velocity of neutrons, S is the surface of the sphere of radius R, n_f is the density of the compressed matter of a target, and μ is the efficient multiplication factor for neutrons in the target matter (according to data [5], $\mu = 2.03$ for ^{239}Pu).

Equation (1) was derived under the assumption that the neutron density is constant inside the sphere and is zero outside the sphere. Integrating Eq. (1), we find the number of neutrons $N(t)$ in the sphere of the radius R at time t:

$$N(t) = N_0 \exp(\alpha t), \qquad (2)$$

where

$$\alpha = \left(\mu n_f \sigma_f - \frac{3}{4R}\right)v, \tag{3}$$

and N_0 is the initial number of neutrons produced in the target volume by an additional external device representing a linear proton accelerator.

Since the product vt is the virtual free path of a neutron during the entire process, the quantity $x = vt/\lambda_f$ is the number of neutron generations. Therefore, the total number of neutrons is expressed in terms of the initial number and the number of generations as

$$N(t) = N_0\mu^x. \tag{4}$$

Combining Eqs. (2)–(4), one obtains the following expression for the "critical" radius R_b of a nuclear drop:

$$R_b = 0.75\lambda_f/(\mu - \ln\mu). \tag{5}$$

Substituting the value $\mu = 2.03$ for R_b into Eq. (5), we obtain the simple relationship $R_b = 0.567\lambda_f$. Relationship (5) was derived under the assumption that

$$\tau_i < \tau_b < \tau_{st}, \tag{6}$$

where τ_i is the time of introducing initial neutrons, τ_b is the time of the chain growth reaction of nuclear matter fission, and τ_{st} is the target stagnation time.

5. A scenario of achieving a positive energy yield from a fissionable material compressed by a heavy-ion beam almost coincides with the scenario described in [2]. An intense ion beam is focused at the end of a cylindrical target and releases an energy of about 5 MJ in the cylindrical layer of an absorber. The time profile of ion-beam energy deposition and the design of the target layers are selected so that the entropy of the compressed matter remains low when moving to the cylinder axis. In this cold compression mode, the stagnation time is $\tau_{st} \approx 2$ ns. The table presents the parameters of energy systems for four volume compression degrees: 300, 400, 500, and 600 (upper row). Row II gives the linear compression. Row III gives the density of the compressed matter. Row IV gives the atomic density measured in 10^{25} cm^{-3}. Row V gives the acceleration radius of the target.

Table

I	300	400	500	600
II	17.3	20	22.4	24.5
III, kg cm^{-3}	6	8	10	12
IV	1.5	2	2.5	3
V, μm	189	142	113	94.5
VI, mg	170	95	61	42
VII, GJ	4.2	2.4	1.5	1.0
VIII	840	480	300	200
IX, Hz	2.4	4.2	6.7	10

target. Row VII gives the energy release in the target. The energy gain for the target is calculated under the assumption that the deposited energy is independent of the mass of compressed nuclear fuel (row VI), and the burned fraction of the nuclear fuel is ≈30%. The operation frequency of the accelerator driver (row IX) was chosen so that the power plant had an average thermal power of 10 GW and an electric power of ≈4 GW. The number of reactors irradiated by one driver depends on the average thermal power absorbed by the cooling system of a reactor. When this power is equal to 2.5 GW, four reactors are obviously required for each variant presented in the table.

6. A short (duration $\tau_i = 0.1$ ns) proton beam with an energy of ≈0.5 GeV and an intensity of 10^9 protons per pulse is directed to the target axis ≈1 ns before the instant of the maximum target compression. The simplest method of obtaining such a high-power (1 GW) proton beam is the 50-fold longitudinal compression of a beam with a current of ≈40 mA at the exit from the linear accelerator. Acting on the compressed target, such a beam will ensure the generation of $N_0 \approx 10^{10}$ initial neutrons in spallation reactions. In this case, the acceleration time varies from ≈0.6 ns for variant 1 to ≈0.3 ns for variant 4, according to Eq. (4). It is seen that condition (6) is satisfied quite well for all four variants: $\tau_i \approx 0.1$ ns, $\tau_b \approx 0.5$ ns, and $\tau_{st} \approx 2$ ns.

7. The mass of a fissionable material can evidently be reduced due to a decrease in the rate of neutron losses into outer layers of a compressed target. With this aim, one can apply the effect of neutron reflection into the target volume from the outer light layers of the target, which have large reflection cross sections. In the best case, about a quarter of the outgoing neutron flux can be returned. In this case, Eq. (1) has the form

$$\frac{d\int ndV}{dt} = \mu\sigma_f n_f \int nvdV - \frac{3}{16}\int nvdS.$$

Correspondingly, $R_b = 0.56\lambda_f/\mu - \ln\mu$, which yields $R_b = 0.42\lambda_f$ for $\mu = 2.03$. The reflection factor $F = n_{ref}\sigma_{ref}\Delta \sim 1$ can practically be achieved with quite a small increase in the density of the beryllium layer up to ~$(1.6-2) \times 10^3$ g/cm^3 for a compression to the thickness $\Delta \sim 10^{-2}$ cm.

8. In order to produce fissionable material through the breeder scheme, the outer stabilizing layer of the target is made from natural ^{238}U. Fast neutrons produce ^{239}Pu in this layer. This accumulation ensures natural reproduction of the fissionable material.

The basic advantages of the above scheme are as follows.

(i) The uncontrolled development of an explosive process is completely excluded because the mass of the fissionable material is limited.

(ii) Only a small amount of major actinides (^{243}Am and ^{247}Cm) can be produced because the process has a high rate.

(iii) Finally, when the fissionable material is completely reproduced through the breeder scheme, natural uranium or thorium can be used as fuel.

The complete calculation of a reactor based on the above scheme of energy production with the optimization of all the parameters is evidently beyond the scope of this study.

We are grateful to Academicians V.I. Subbotin and L.P. Feoktistov[†] for stimulating discussions.

[†] Deceased

REFERENCES

1. D. G. Koshkarev and B. Yu. Sharkov, Application for Invention No. 2002100801 (2002).

2. D. G. Koshkarev and M. D. Churazov, At. Énerg. **91**, 47 (2001).

3. G. A. Askar'yan, V. A. Namiot, and M. S. Rabinovich, Pis'ma Zh. Éksp. Teor. Fiz. **17**, 597 (1973) [JETP Lett. **17**, 424 (1973)].

4. A. F. Sidorov, Dokl. Akad. Nauk SSSR **318**, 548 (1991) [Sov. Phys. Dokl. **36**, 347 (1991)].

5. *Physics of Nuclear Fission* (Atomizdat, Moscow, 1957), Supplement No. 1 to At. Énerg.

Translated by R. Tyapaev

Light Confinement and Supercontinuum Generation Switching in Photonic-Molecule Modes of a Microstructure Fiber

A. B. Fedotov[1], I. Bugar[2], A. N. Naumov[1], D. Chorvat, Jr.[2], D. A. Sidorov-Biryukov[1], D. Chorvat[2], and A. M. Zheltikov[1], *

[1] *Faculty of Physics, International Laser Center, Lomonosov Moscow State University, Vorob'evy gory, Moscow, 119899 Russia*
*e-mail: zheltikov@top.phys.msu.su
[2] *International Laser Center, Ilkovicova 3, Bratislava, 81219 Slovak Republic*
Received February 21, 2002

The modes guided in a ring system of microstructure-integrated fibers are shown to have much in common with electron wave functions in a two-dimensional polyatomic cyclic molecule. This photonic-molecule analogy provides, in particular, an illustrative and physically clear model of dispersion properties and the mode structure of an electromagnetic field in microstructure fibers of the considered type. A high degree of light confinement in waveguide modes of such a photonic molecule enhances nonlinear-optical processes, permitting an octave spectral broadening to be achieved for low-energy femtosecond laser pulses. © 2002 MAIK "Nauka/Interperiodica".

PACS numbers: 42.65.Wi; 42.81.Qb

Modern nanotechnologies open unique possibilities for the creation of new materials with desirable optical properties [1]. Micro- and nanostructuring may modify the spatial symmetry of optical characteristics [2], giving rise, in particular, to artificial birefringence [3] and suggesting the way of engineering new materials for laser physics and nonlinear optics [1]. Local-field enhancement in micro- and nanostructured materials increases nonlinear-optical susceptibilities [4], while dispersion tailoring possibilities allow nonlinear-optical interactions to be phase-matched [1, 3, 5].

Analysis of modes of the electromagnetic field in nanostructures and microcavities is one of the fundamental problems in the optics of micro- and nanostructured matter. The modes of electromagnetic radiation confined in such structures are often similar in many ways to the wave functions of electrons whose motion is bounded in space by a potential of an atom, molecule, or a crystal lattice. By analogy with different types of electron wave functions, the concepts of a photonic dot, photonic atom, photonic molecule [6, 7], and a photonic crystal [8] have been introduced in the optics of nanostructures. In particular, mode properties of a pair of coupled microcavities, as shown in [6], are similar to the properties of electronic states in a diatomic molecule. In this paper, we will generalize the concept of a photonic molecule (PM) to the case of a ring structure of coupled two-dimensional microcavities. We will show that the modes guided in a microstructure (MS) fiber with a cross section in the form of such a ring structure have much in common with electron wave functions of a two-dimensional polyatomic cyclic mol-

ecule. The results of our studies presented in this paper show that the high degree of light confinement in waveguide modes of a photonic molecule considerably enhances nonlinear-optical interactions, allowing an octave spectral broadening to be achieved for nanojoule femtosecond laser pulses.

In our experiments, we employed microstructure fibers [9–11] fabricated at the Technology and Equipment for Glass Structures Institute (Saratov, Russia) with the use of the technique that has now become standard [9, 12] and that involves stacking capillaries into a preform and then pulling this preform at elevated temperatures. A preform with a central capillary of a larger diameters surrounded by capillaries smaller diameter was employed to fabricate an MS fiber used in our experiments. Figure 1a shows a cross-sectional image of such a fiber. The ring system of fibers linked by narrow glass bridges at the center of this MS fiber (Fig. 1a) is reminiscent in its structure of the configuration of atoms linked by chemical bonds in a cyclic polyatomic molecule consisting of identical atoms (a generic diagram of such a molecule is shown in Fig. 1b). This photonic-molecule analogy will later prove to be quite rewarding by providing us with an illustrative and physically clear model of the dispersion properties and mode structure of the rather complicated optical fiber under consideration. Physical and mathematical aspects of the analogy between a bundle of coupled microstructure-integrated fibers and a polyatomic molecule should be emphasized. Physically, the action of a refractive-index step on a light field is similar to the influence of a potential distributed in space on an elec-
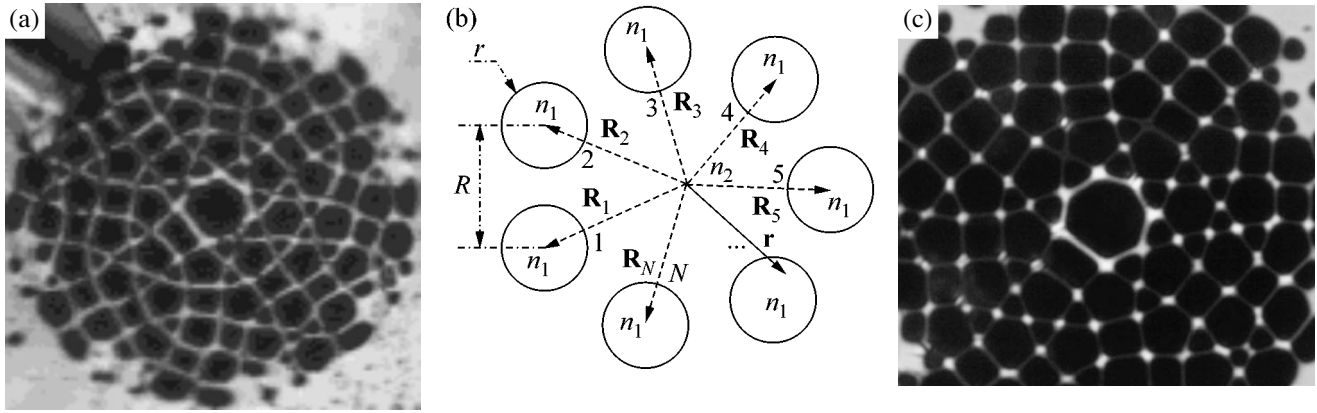
Fig. 1. (a) A cross-sectional microscopic image of a cobweb microstructure fiber. The ring system of glass channels at the center of this fiber forms a two-dimensional photonic molecule. The radius of each channel in the central ring is equal to 2 μm. The distance between the neighboring channels is 7.4 μm. (b) A photonic-molecule model of an optical fiber where the light is guided along a set of N coupled cores with the refractive index n_1 surrounded by a material of the cladding with the refractive index n_2. (c) The spatial distribution of He–Ne-laser radiation intensity at the output of the cobweb microstructure fiber corresponding to the fundamental photonic-molecule mode.

tron wave function in a molecular system. Mathematically, this analogy stems from the similarity of coupled-theory equations for electromagnetic radiation in an array of coupled fibers [13] to perturbation-theory equations for the electron wave function in a polyatomic molecule.

Our photonic-molecule microstructure-integrated bundle of fibers can guide the light through total internal reflection, providing a very high degree of light confinement due to the large refractive index step on the glass–air interface (Fig. 1c). Due to this property, MS fibers of the considered type are promising for enhancing nonlinear-optical interactions and reducing the lasing threshold in micro- and nanostructured laser materials.

In our analysis of mode properties of radiation guided in a PM fiber, we will neglect polarization effects and employ a scalar-wave-equation approximation [13] to consider a set of N cyclically coupled identical channels with the refractive index n_1 surrounded by a material with the refractive index n_2 (Fig. 1b). Since the strongest mode coupling is achieved for waveguide modes with equal propagation constants in a photonic-molecule fiber with identical cores, we will neglect also the coupling of modes with different propagation constants. The modes of the PM fiber can then be represented as superpositions of modes of isolated fibers:

$$\Psi(\mathbf{r}) = \sum_n A_n f(\mathbf{r} - \mathbf{R}_n), \qquad (1)$$

where $\mathbf{r}$ is the radius vector in the plane of a fiber cross section (the plane of Fig. 1b), $\mathbf{R}_n$ are the coordinates of the center of the nth fiber in the same plane, and A_n and $f(\mathbf{r} - \mathbf{R}_n)$ are the amplitude and the transverse distribu-

tion of the field in the guided mode in the nth fiber. Since only the neighboring fibers are coupled to each other in our photonic-molecule bundle, the coupled-mode equations for the field amplitudes can be written as [13]

$$dA_n/dz - i\beta A_n - i\alpha(A_{L(n)} + A_{R(n)}) = 0, \qquad (2)$$

where β is the propagation constant for the relevant guided mode of an isolated fiber,

$$\alpha = \frac{\omega^2}{2\beta c^2} \frac{\int \Delta\varepsilon(\mathbf{r}) f(\mathbf{r} - \mathbf{R}_{n'}) f^*(\mathbf{r} - \mathbf{R}_n) d\mathbf{r}}{\int |f(\mathbf{r} - \mathbf{R}_n)|^2 d\mathbf{r}} \qquad (3)$$

is the coefficient characterizing mode coupling for the nth and $(n + 1)$th fibers in the considered structure (ω is the radiation frequency and $\Delta\varepsilon(\mathbf{r})$ is the deviation from the unperturbed dielectric constant at a given point with a radius vector $\mathbf{r}$), and

$$L(n) = \begin{cases} n-1, & n > 1 \\ N, & n = 1, \end{cases}$$

$$R(n) = \begin{cases} n+1, & n < N \\ 1, & n = N. \end{cases}$$

The propagation constants can now be found from the characteristic equation corresponding to the set of equations (2). In the general case of arbitrary N, these propagation constants can be calculated with the use of numerical methods. There are several simple analytical solutions, however, that provide useful physical insight
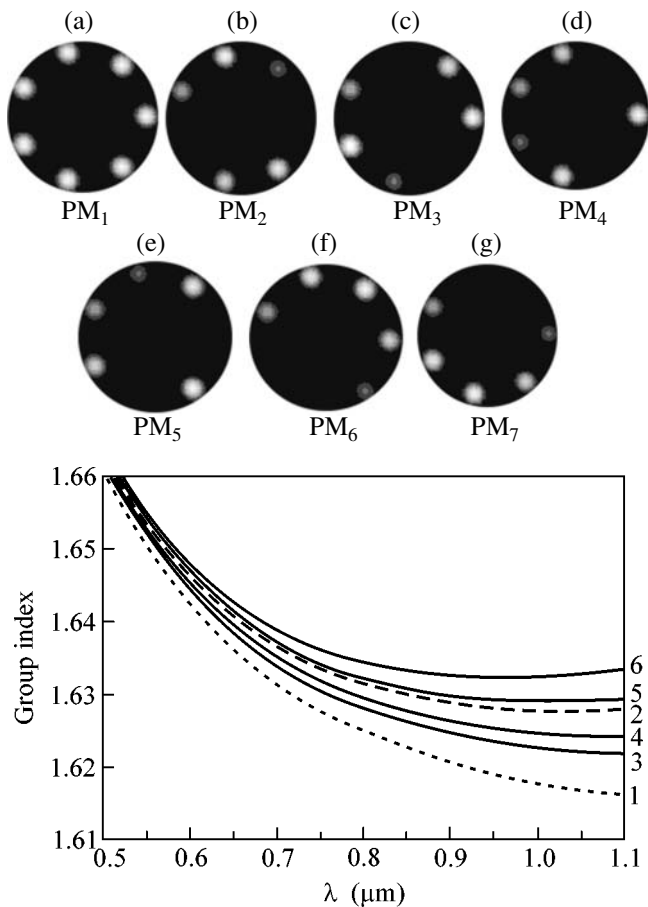
Fig. 2. The group index as a function of radiation wavelength for (*1*) the material of the fiber; (*2*) a single isolated fiber from the considered photonic-molecule structure; and (*3*) PM$_1$, (*4*) PM$_2$ and PM$_3$, (*5*) PM$_4$ and PM$_5$, and (*6*) PM$_6$ and PM$_7$ modes of a seven-core photonic-molecule fiber. The radius of a single fiber in the PM fiber structure is 2 μm. The distance between the neighboring fibers in the PM structure is 7.4 μm. The insets show light intensity distributions in (a) PM$_1$, (b) PM$_2$, (c) PM$_3$, (d) PM$_4$, (e) PM$_5$, (f) PM$_6$, and (g) PM$_7$ modes of a seven-core photonic-molecule fiber.

into the dispersion of the photonic-molecule fiber. In particular, a symmetric field distribution,

$$\Psi_1(\mathbf{r}) = A\sum_n f(\mathbf{r} - \mathbf{R}_n), \qquad (4)$$

where A is a constant, is allowed by Eq. (2) for any N. This symmetric mode of our fiber is similar to a symmetric wave function of a polyatomic molecule. The propagation constant for such a symmetric mode is given by

$$B_1 = \beta + 2\alpha. \qquad (5)$$

Expression (5) shows that mode coupling in the considered array of fibers results in a renormalization of propagation constants.

An antisymmetric solution

$$\Psi_N(\mathbf{r}) = A\sum_n (-1)^n f(\mathbf{r} - \mathbf{R}_n) \qquad (6)$$

is also allowed by Eq. (2) for even N. This antisymmetric mode also has an obvious analogy in quantum chemistry. The propagation constant is then renormalized in accordance with

$$B_N = \beta - 2\alpha. \qquad (7)$$

We identify the fundamental mode of our PM fiber as the mode with the largest propagation constant. The highest value of the propagation constant in the case under consideration is achieved for the symmetric mode. In terms of the point-group symmetry, this mode possesses the full rotational symmetry of an idealized PM fiber with perfect rotational symmetry (cf. Figs. 1a–1c). We introduce the mode index l to enumerate PM-fiber modes, which will be denoted as PM$_l$ modes, starting with $l = 1$, which corresponds to the fundamental PM mode.

Numerical simulations were performed for a PM fiber structure that modeled the MS fiber employed in our experiments and that consisted of seven identical glass cores with a radius $a = 2$ μm. The refractive index of the cladding was set equal to the refractive index of atmospheric-pressure air ($n_2 = 1$). The distance R between the neighboring cores was 7.4 μm. To estimate the coupling coefficient appearing in Eq. (2), we employed the expression for the coupling coefficient, $\alpha = C\lambda$, where λ is the wavelength, from the model of two coupled identical planar waveguides [13]. For characteristic geometric sizes of our structure, this model allows the parameter C to be estimated as 0.016 μm. Only lowest order modes of isolated fibers were included in our calculations. The inclusion of higher order modes will, of course, change dispersion branches of a PM fiber and make the analysis much more complicated. The model that includes only fundamental modes of each elementary fiber, on the other hand, allows the general physical features of dispersion of a PM fiber to be understood without reproducing the fiber dispersion in all the details.

Figure 2 displays the group index as a function of radiation wavelength for the material of the fiber (curve *1*), a single isolated fiber from the considered photonic-molecule structure (curve *2*), and PM$_1$–PM$_7$ modes of the considered seven-core MS fiber (curves *3–6*). The transverse light intensity distributions corresponding to these modes are shown in the insets a–g in Fig. 2. The lowest value of the group index, as can be seen from the results presented in Fig. 2, is achieved for the PM$_1$ fundamental mode. Higher order PM modes are characterized by lower group velocities, implying that nonlinear-optical processes should be enhanced for these modes.

This expectation has been fully justified by the results of our experiments devoted to the investigation
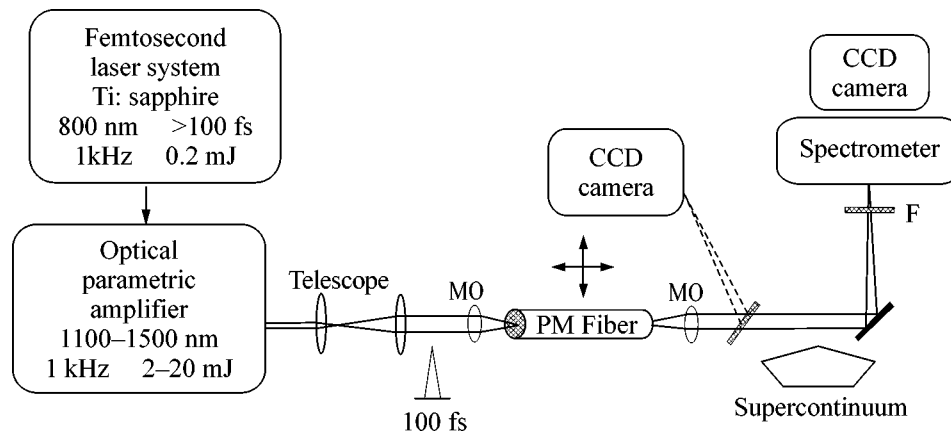
Fig. 3. Frequency-tunable femtosecond laser system based on an optical parametric amplifier: MO, microobjectives; F, system of optical filters.

of the spectral broadening of femtosecond pulses in a PM fiber. Femtosecond pulses were produced in our experiments by a laser system consisting of a Ti:sapphire master oscillator, a multipass amplifier, and an optical parametric amplifier (OPA) based on a BBO crystal (Fig. 3). This laser system generated laser pulses with a wavelength tunable from 1.1 to 1.5 μm. The best performance of the OPA system was achieved at the wavelength of 1.25 μm, where light pulses with a duration of approximately 80 fs were produced.

Laser radiation was coupled into an MS fiber sample placed on a three-coordinate translation stage with the use of a microobjective. The efficiency of waveguide mode excitation in the MS fiber was monitored by imaging the light field distribution at the output end of the fiber onto a CCD camera (Fig. 3) and by measuring the total energy of radiation coming out of the fiber. Varying the focusing geometry and shifting the fiber end with respect to the light beam coupled into the fiber, we were able to excite, in fact, all the PM_l fiber modes with $l = 1, 2, ..., 7$. We observed efficient spectral broadening of femtosecond OPA pulses and supercontinuum generation for all these modes. The efficiency of supercontinuum generation in higher order PM modes was noticeably higher than the efficiency of white-light generation in the fundamental PM mode. Figure 4 presents the spectra of supercontinuum emission produced in PM_1 and PM_6/PM_7 modes in a 4-cm PM-fiber sample (the spatial distributions of radiation intensity at the output of the fiber are shown in the insets in Fig. 4). Comparison of curves *1* and *2* in Fig. 4 shows that the supercontinuum emission generated in the PM_6 and PM_7 modes had a noticeably broader bandwidth than the supercontinuum generated in the fundamental mode. The spectrum of the supercontinuum generated by 80-fs pulses of 1.3-μm OPA radiation in the PM_6/PM_7 mode of our fiber reached approximately

one octave starting with the laser pulse energy of about 100 nJ.

Thus, we have demonstrated that the modes guided in a ring system of microstructure-integrated fibers have much in common with electron wave functions in a two-dimensional polyatomic cyclic molecule. The photonic-molecule model provides an illustrative qualitative description of dispersion properties and the mode structure of the electromagnetic field in micro-
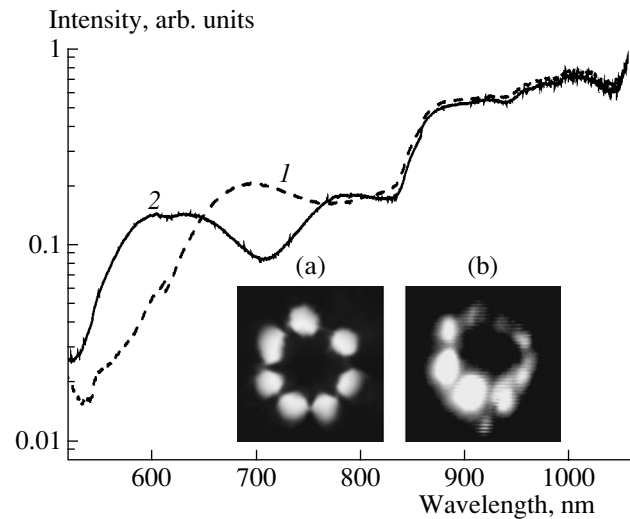
Fig. 4. The spectra of a supercontinuum generated in the (*1*) PM_1 and (*2*) PM_6/PM_7 modes of a photonic-molecule fiber with a length of 4 cm. OPA radiation pulses with a wavelength of 1.30 μm and an energy of 100 nJ are coupled into the fiber. The initial duration of light pulses is 80 fs. The radius of a single fiber in the PM fiber structure is 2 μm, and the distance between the neighboring fibers in the PM structure is 7.4 μm. The insets show white-light images of PM fibers produced with the use of a supercontinuum generated in (a) the PM_1 and (b) PM_6/PM_7 modes of such a fiber by 80-fs 100-nJ pulses of 1.3-μm OPA radiation.

structure fibers of the considered type. A high degree of light confinement in waveguide modes of such a photonic-molecule fiber enhances the nonlinear-optical processes, permitting an octave spectral broadening to be achieved for low-energy femtosecond laser pulses.

REFERENCES

1. *Nanoscale Linear and Nonlinear Optics*, Ed. by M. Bertolotti, C. M. Bowden, and C. Sibilia (American Inst. of Physics, New York, 2001).
2. A. Fiore, V. Berger, E. Rosencher, *et al.*, Nature **391**, 463 (1998).
3. L. A. Golovan, V. Yu. Timoshenko, A. B. Fedotov, *et al.*, Appl. Phys. B **B73**, 31 (2001).
4. J. E. Sipe and R. W. Boyd, Phys. Rev. A **46**, 1614 (1992).
5. A. M. Zheltikov, A. V. Tarasishin, and S. A. Magnitskiĭ, Zh. Éksp. Teor. Fiz. **118**, 340 (2000) [JETP **91**, 298 (2000)].
6. M. Bayer, T. Gutbrod, J. P. Reithmaier, *et al.*, Phys. Rev. Lett. **81**, 2582 (1998).
7. T. Mukaiyama, K. Takeda, H. Miyazaki, *et al.*, Phys. Rev. Lett. **82**, 4623 (1999).
8. J. Joannopoulos, R. Meade, and J. Winn, *Photonic Crystals* (Princeton Univ. Press, Princeton, 1995).
9. J. C. Knight, T. A. Birks, P. St. J. Russell, and D. M. Atkin, Opt. Lett. **21**, 1547 (1996).
10. J. C. Knight, J. Broeng, T. A. Birks, and P. St. J. Russell, Science **282**, 1476 (1998).
11. A. M. Zheltikov, Usp. Fiz. Nauk **170**, 1203 (2000).
12. A. B. Fedotov, A. M. Zheltikov, L. A. Mel'nikov, *et al.*, Pis'ma Zh. Éksp. Teor. Fiz. **71**, 407 (2000) [JETP Lett. **71**, 281 (2000)].
13. A. Yariv and P. Yeh, *Optical Waves in Crystals: Propagation and Control of Laser Radiation* (Wiley, New York, 1984; Mir, Moscow, 1987).

Translated by A. Zheltikov

Phase Problem in Three-Beam X-ray Diffraction

A. M. Afanas'ev[1], A. V. Zozulya[2], M. V. Koval'chuk[2], and M. A. Chuev[1, *]

[1] *Institute of Physics and Technology, Russian Academy of Sciences, Nakhimovskiĭ pr. 36, Moscow, 117218 Russia*
* e-mail: chuev@ftian.oivta.ru
[2] *Shubnikov Institute of Crystallography, Russian Academy of Sciences, Leninskiĭ pr. 59, Moscow, 117333 Russia*
Received February 22, 2002

It is shown that, apart from the purely elastic scattering of X-rays, their inelastic coherent scattering by phonons can play, in some cases, a significant part in the formation of reflection curves for multiple X-ray diffraction. This process may affect the interference pattern for weak reflection, and it must be taken into account when extracting the triplet phase, as was demonstrated by an analysis of the experimental rocking curves obtained for the coplanar three-beam diffraction by a KDP crystal. © *2002 MAIK "Nauka/Interperiodica".*

PACS numbers: 61.10.Dp

A knowledge of the phases of structure amplitudes is highly important for determining the crystal structure of complex materials, particularly, biological objects. Multiple X-ray diffraction is one of the few methods that make it possible to extract the phases of structure amplitudes, primarily, the so-called triplet phase (see, e.g., [1–10] and references cited therein). Despite the extensive theoretical literature on this problem, it cannot be considered as conclusively solved. Apart from the purely elastic diffraction scattering, there is also a contribution from the inelastic coherent scattering (ICS) by phonons, which is known to manifest itself in the diffraction curves obtained for the two-beam geometry [11, 12], for which ICS is usually taken into account to correct the extracted structure amplitudes [13–16]. It is shown below that the ICS in multiple diffraction also produces an interference pattern, which, however, was fully disregarded by previous researchers. In this work, this process is analyzed and the results of experimental and theoretical studies of three-beam diffraction in so-called coplanar geometry are reported. In this geometry, ICS has the greatest effect on the diffraction reflection curves and, as is seen below, clearly shows up in the experimental curves.

Figure 1 shows the experimental scheme of the coplanar three-beam diffraction by a KDP crystal. In this experiment, reflection planes (420) and (280) were chosen so that the incident and both diffracted beams lay in the same plane. In this geometry, no fine beam collimation in the vertical plane is necessary, thereby providing high luminosity of the method. Measurements were made using a double-crystal scheme with $CoK_{\alpha 1}$ radiation from the standard X-ray tube with a power as low as 2 kW. Preliminary angular collimation of the incident beam for the horizontal angle θ was provided by a collimator Ge crystal using asymmetric reflection (311), and after the collimator the radiation intensity incident on the crystal under study was on the

order of 10^6 count/s. The rocking curves were measured as functions of the angle of rotation of the crystal about the vertical axis (so-called θ scan). The setup also allowed the rotation about the axis perpendicular to the crystal surface (ψ scan), but the accuracy of the θ rotation was considerably higher than for the ψ rotation. In this case, the reflection curves were nicely recorded for both beams, as is seen from Fig. 2 (see [17] for more detail). A remarkable feature of our experiment was also that the collimator crystal was arranged in such a way that it provided a practically dispersionless (420) reflection, so that the corresponding rocking curve appeared as a very narrow peak with a width of less than 4" and a peak reflectivity on the order of 0.25. As for the diffraction reflection (280), it was strongly smeared in angle θ over several hundred of seconds of arc. Such a smearing was mostly due to the fact that the
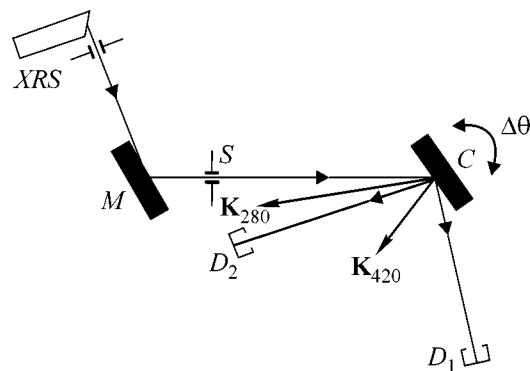
Fig. 1. Scheme of the experiment: *XRS* is the X-ray source, *M* is the Ge monochromator (collimator), *C* is the KDP crystal under study, D_1 and D_2 are the detectors, and *S* is the slit.
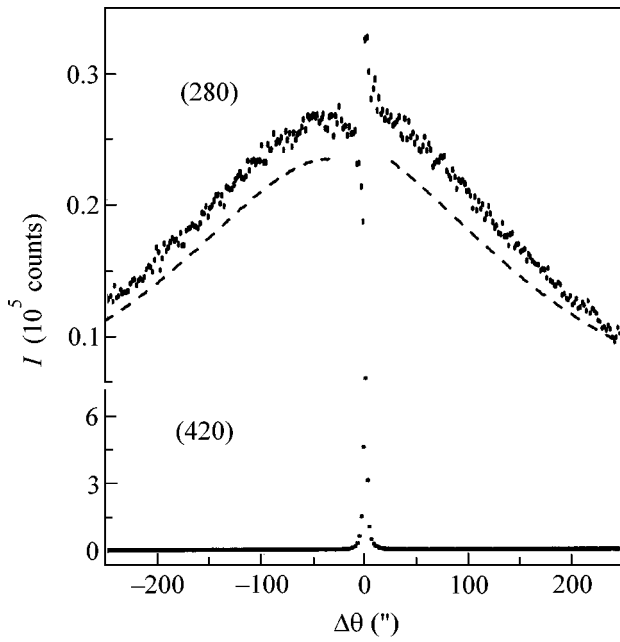
Fig. 2. Experimental rocking curves for the reflections from the KDP (420) and (280) planes, as measured over a wide angular range (the bars take into account statistical error). The dashed line corresponds to the calculation using the dynamical theory of elastic X-ray scattering in the three-beam approximation.
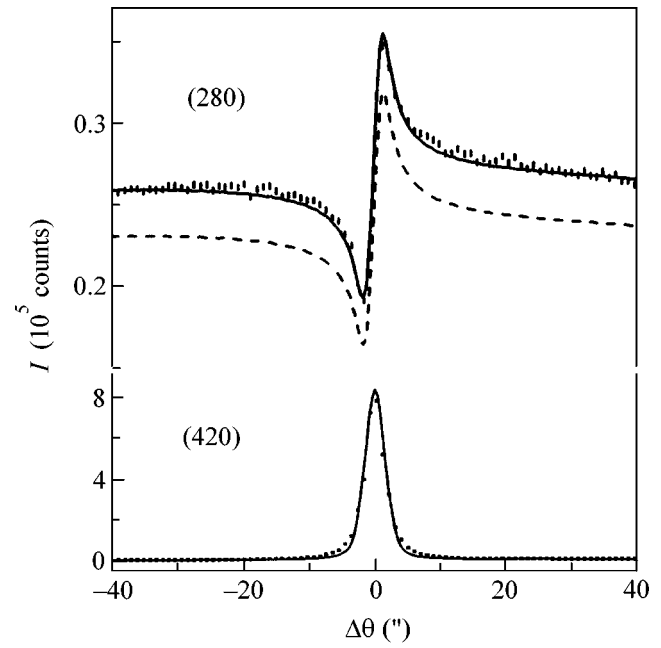
Fig. 3. (vertical bars) Experimental rocking curves for the reflections from the KDP (420) and (280) planes, as measured in a narrow angular interval. The dashed line corresponds to the calculation for a purely elastic X-ray scattering, and the solid line takes into account the additional contribution from the inelastic coherent scattering by phonons.

reflection planes (311) of the collimator and (280) of the sample were in highly dispersive positions: $\theta_B(311) = 31.6°$ and $\theta_B(280) = 81.8°$; i.e., the difference in the corresponding Bragg angles was about 50°. Besides, the $CoK_{\alpha 1}$ line (wavelength $\lambda = 1.789$ Å) has a rather large width $\Delta\lambda$ on the order of 0.71×10^{-3} Å. Due to these two circumstances, only a small fraction (about one percent) of the incident beam underwent strong reflection from the sample. Nevertheless, the interference pattern is clearly seen in the (280) reflection curve, because the reflection intensity results from the interference of two paths: the direct reflection from the (280) plane ($\kappa \longrightarrow \kappa_2$) and two sequential (420) and ($\bar{2}60$) reflections ($\kappa \longrightarrow \kappa_1 \longrightarrow \kappa_2$). These two scattering processes are coherent, and their amplitudes add up to form the interference pattern (see [1]). The character of interference depends on the so-called triplet phase

$$\Phi_3 = \arg(\chi_{420}\chi_{\bar{2}60}\chi_{280}^*), \tag{1}$$

where $\chi_h = \chi(\mathbf{K}_h)$ are the corresponding Fourier components of crystal polarizability and $\mathbf{K}_h$ are the reciprocal lattice vectors.

The observed (420) reflection curves are adequately described by the theoretical curves calculated using the dynamical theory of X-ray elastic scattering with allowance made for the three-beam scattering (which introduces only small corrections to these curves),

small dispersion between the Ge(311) and KDP(420) reflections, and small collimator line width. This is clearly seen from the rocking curves shown in Fig. 3, where the results of careful measurements in a relatively narrow angular interval are presented. As for the (280) reflection, similar calculations do not provide satisfactory agreement with the experiment. In this case, the theoretical intensities are appreciably lower than their experimental values, as is clearly seen in Fig. 3; this tendency persists over a broader angular range in Fig. 2. Below, a plausible explanation is proposed for this fact.

Let the plane wave with amplitude E_0, polarization $\boldsymbol{\eta}_0$, and wave vector $\boldsymbol{\kappa}$ be incident on the crystal,

$$\mathbf{E}(\mathbf{r}) = \boldsymbol{\eta}_0 E_0 \exp(i\boldsymbol{\kappa}\mathbf{r}). \tag{2}$$

In the three-beam approximation, the dynamical diffraction scattering in coplanar geometry gives rise to the field

$$\begin{aligned} \mathbf{D}(\mathbf{r}) = {} & E_0(\boldsymbol{\eta}_0 + \boldsymbol{\eta}_{420}d_{420}e^{i\mathbf{K}_{420}\mathbf{r}} + \boldsymbol{\eta}_{280}d_{280}e^{i\mathbf{K}_{280}\mathbf{r}}) \\ & \times \exp[i(\boldsymbol{\kappa}\mathbf{r} + \kappa z\varepsilon^{(1)}/\gamma_0)] \end{aligned} \tag{3}$$

in a crystal, where $\boldsymbol{\eta}_{420}$ and $\boldsymbol{\eta}_{280}$ are the respective polarization vectors, $\gamma_0 = \boldsymbol{\kappa}\mathbf{n}/\kappa$ ($\mathbf{n}$ is a unit vector normal to the crystal surface), and $\varepsilon^{(1)}$ is the so-called accommodation coefficient accounting for the refraction of the incident wave upon its passage from a vac-

uum into crystal [1]. The coefficient $\varepsilon^{(1)}$ and the amplitudes d_{420} and d_{280} can be found by solving the dynamical equations (see, e.g., [1, 18]). Generally speaking, in the coplanar diffraction by a crystal of an arbitrary thickness, not one but three modes of type (3) arise. In a thick crystal, only one mode corresponding to the maximal value of Im[$\varepsilon^{(i)}$] is left. In addition, the waves with polarizations lying in the scattering plane (π polarization) and perpendicular to it (σ polarization) differ in the strength of interaction with the crystal and should be calculated separately. In a thick crystal, the amplitudes d_{420} and d_{280} determine the reflected intensities,

$$I_h^{(s)} = E_0^2 |d_h^{(s)}|^2 / |\beta_h|, \qquad (4)$$

where $s = \sigma$ or π, $\beta_h = \gamma_0/\gamma_h$ is the so-called asymmetry parameter, and $\gamma_h = (\kappa + \mathbf{K}_h)\mathbf{n}/\kappa$ (see, e.g., [11, 12]).

To compare the results of theoretical calculations with the experimental data, one should (i) form the convolution of the reflected intensities (4) with the reflection curve P_M of the collimator crystal, (ii) take into account the dispersion, and (iii) sum over the two polarizations. Although the diffraction scheme is coplanar, one should also average over the angle ψ,

$$\bar{I}_h(\theta) = \sum_{s = \sigma, \pi} \int g(\omega) d\omega \int d\psi \int d\theta' \qquad (5)$$
$$\times P_M^{(s)}(\theta', \psi, \omega) I_h^{(s)}(\theta - \theta', \psi, \omega),$$

where $\omega = 2\pi c/\lambda$ and $g(\omega)$ is the X-ray line shape with the contributions from both $CoK_{\alpha1}$ and $CoK_{\alpha2}$ lines; the reflection curve P_M was calculated in the two-beam approximation. The theoretical curves for this scheme are represented in Figs. 2 and 3 by the dashed lines. As for the (420) reflection, the calculated amplitude and width of the corresponding Bragg peak reproduce rather well the corresponding experimental curve. The reflectivity of this peak proves to be quite high (on the order of 0.25), and its width is 3.3". For the pure (420) reflection (without convolutions), the corresponding values are equal to 0.8 and 1.1". The (311) reflection from the collimator crystal was chosen so as to realize the strongly asymmetric diffraction scheme (with the asymmetry parameter $\beta \approx 25$) and, thereby, provide the narrow θ collimation. However, despite the large asymmetry parameter, the beam reflected from the collimator was rather wide ($\Delta\theta_M \approx 1.6"$), as a result of which the KDP reflection curve broadened and its peak intensity decreased. The small additional broadening was also caused by the dispersions of the (311) and (420) reflections. A slight discrepancy between the calculated and experimental curves at the Bragg peak tails is likely caused by the lattice imperfections and not-too-high quality of surface treatment.

As for the (280) reflection, the results of calculation using the scheme described above with allowance for all the above-mentioned factors are distinctly inconsis-

tent with the experimental data (dashed curves in Figs. 2, 3). The experimental curves lie appreciably higher than the theoretical ones, and, in addition, the influence of interference is observed in a broader angular range than predicted by theory. The conclusion itself suggests that some additional process makes a contribution to the intensity of the (280) reflection. It will be shown below that the inelastic coherent X-ray scattering by phonons is such a process.

Lattice vibrations determine a very important characteristic of the diffraction X-ray scattering, namely, the Debye–Waller factor. It was shown by Zachariasen as early as 1945 [11] that the phonon-induced ICS makes an additional contribution to the scattering intensity in the region near the Bragg peak. As the Bragg peak is approached, the corresponding differential intensity diverges as $1/\Delta\theta$ ($\Delta\theta = \theta - \theta_B$), so that the integrated intensity diverges logarithmically. This fact is taken into account when correcting the data of elastic scattering in the standard structural analysis of small-sized crystallites. The diffuse scattering by phonons in ideal crystals was considered in the two-beam approximation, e.g., in [19–21]. As for the multiple dynamical scattering, the diffuse scattering remains to be analyzed for this case. It will be shown below that the phonon-induced ICS not only affects the reflected intensity but also gives rise to interference between different channels of this process.

Scattering by phonons is a typical process of the transition between the continuum states. Because it is weaker than the elastic coherent diffraction scattering, its intensity can be calculated using the quantum-mechanical "golden rule"; namely, the probability of an X-ray quantum with wave vector $\mathbf{k}$ and polarization s being scattered to the ($\mathbf{k}'$, s') state with the simultaneous emission or absorption of a phonon with wave vector $\mathbf{q}$ and polarization l can be calculated by the formula [22]

$$dw(\mathbf{k}, s, \mathbf{k}', s', \pm\mathbf{q}, l) = \frac{2\pi}{\hbar} |\langle \mathbf{k}', s', \pm\mathbf{q}, l | U | \mathbf{k}, s \rangle|^2$$
$$\times \delta(\hbar ck - \hbar ck' \pm \hbar c_q q) \frac{d^3k'}{(2\pi)^3} \frac{d^3q}{(2\pi)^3}, \qquad (6)$$

where U is the interaction responsible for the inelastic scattering, c is the velocity of light, and c_q is the sound velocity. The main contribution to the process of interest comes from the single-phonon scattering. For the corresponding matrix element in Eq. (6), one can easily obtain

$$U(\mathbf{k}, s, \mathbf{k}', s', \pm\mathbf{q}, l) = U_0(\mathbf{k}, s, \mathbf{k}', s')$$
$$\times \sum_j \sum_{\mathbf{q}} \sum_l \sqrt{\frac{\hbar(2\bar{n}_{\mathbf{q}, l} + 1)}{2\rho\omega_{\mathbf{q}, l}}} ((\mathbf{k}' - \mathbf{k})\xi_l) e^{i(\mathbf{k}' - \mathbf{k} \pm \mathbf{q})\mathbf{r}_j}, \qquad (7)$$

where $\bar{n}_{\mathbf{q}, l}$ is the mean number of ($\mathbf{q}$, l) phonons; $\omega_{\mathbf{q}, l}$ and ξ_l are the phonon frequency and polarization vector, respectively; ρ is the crystal density; $\mathbf{r}_j$ is the run-
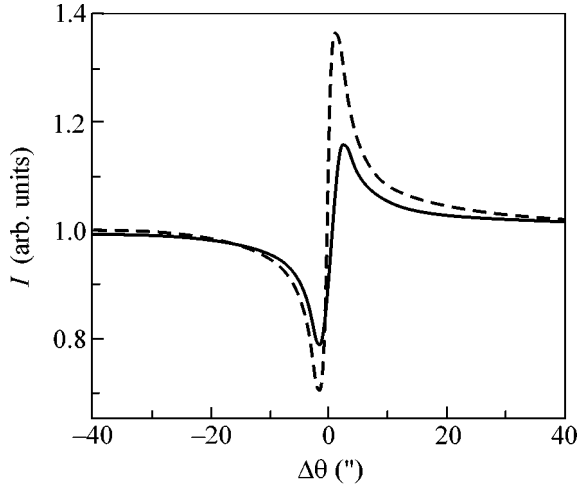
Fig. 4. The shapes of normalized rocking curves for the reflection from the KDP (280) plane, as calculated for the (dashed line) purely elastic scattering and (solid line) inelastic coherent scattering by phonons.

ning atomic coordinate in the unit cell; and the sum over j goes over all scattering atoms in the unit cell. The purely elastic contribution $U_0(\mathbf{k}, s, \mathbf{k'}, s')$ is determined by the well-known formula

$$U_0(\mathbf{k}, s, \mathbf{k'}, s') = \frac{2\pi\hbar c r_0}{\kappa} \sum_j \overline{\langle \psi_{\mathbf{k'}, s'}(\mathbf{r}_j) | \psi_{\mathbf{k}, s}(\mathbf{r}_j)\rangle}, \quad (8)$$

where r_0 is the classical electron radius, and the bar over the matrix element stands for the averaging over the atoms in the unit cell and over phonons. Note that Eq. (7) is only valid if we are interested in the contribution from acoustic phonons.

To calculate by formula (6), one must also know the states $\psi_{\mathbf{k}, s}$ and $\psi_{\mathbf{k'}, s'}$ between which the transition occurs. These states are usually taken as plane waves. As regards the initial state $\psi_{\mathbf{k}, s}$, it transforms, due to the coherent interaction, into the state of type (3). In our case, the final state $\psi_{\mathbf{k'}, s'}$ is a scattered wave with wave vector $\mathbf{k'}$ leaving the crystal. In the majority of cases, the matrix elements of operator U in Eq. (6) are calculated using the complex conjugate state. However, in dynamical theory, one cannot define any initial state that would correspond not to the incident radiation but to the radiation exiting from the crystal. This difficulty can be obviated by the method proposed by Sommerfeld as early as 1931 and described in detail in [22]. Instead of the state that is complex conjugate to $\psi_{\mathbf{k'}, s'}$, one should use the *time-inverse* state $\psi^-_{\mathbf{k'}, s'}$ (in the notation of [22]). As a result, the outgoing wave converts into an incoming wave, for which the wave fields in the crystal can be calculated by full analogy with the incident wave $\mathbf{k}$ [see Eqs. (2), (3)]. Since the majority of inelastically scattered waves are far away from the

Bragg conditions, one can use, instead of Eq. (3), the simplified formula

$$\mathbf{D}^-(\mathbf{r}) = \boldsymbol{\eta}_{s'} \exp[-i\boldsymbol{\kappa}\mathbf{r} + i\kappa z \chi_0/(2\gamma'_h)]. \quad (9)$$

By using Eqs. (3) and (6)–(9), one can obtain, after rather tedious though simple mathematics, the expression for the X-ray reflectivity corresponding to the phonon-induced ICS. In the case of three-beam diffraction and coplanar geometry, it can be written for a weak KDP (280) reflection as

$$P^{(ine)}_{280}(\mathbf{k}, \mathbf{k'}) = \frac{\kappa^2}{4\gamma_0\gamma_{280}}\frac{1}{\Gamma}$$

$$\times \sum_l \left| C_{280}\chi_{280}(\boldsymbol{\xi}_l\mathbf{K}_{280}) + d_{420}C_{\bar{2}60}\chi_{\bar{2}60}(\boldsymbol{\xi}_l\mathbf{K}_{\bar{2}60})\right|^2 \quad (10)$$

$$\times \frac{k_B T}{(2\pi)^2\rho}\iint \frac{dq_x dq_y}{c^2_{\mathbf{q}, l}q^2},$$

where $C_h = (\boldsymbol{\eta}_0\boldsymbol{\eta}_h)$ is the polarization factor (the polarization indices s are omitted), $c_{\mathbf{q}, l}$ is the sound velocity, T is temperature, x and y are the coordinates at the crystal surface, and

$$\Gamma = \kappa\left(\frac{2\mathrm{Im}(\varepsilon^{(1)})}{\gamma_0} - \frac{\mathrm{Im}(\chi_0)}{\gamma_{280}}\right). \quad (11)$$

The coefficients $\varepsilon^{(1)}$ and d_{420} should be calculated using the equations of dynamical theory, and the integrals over $\mathbf{q}$ should be taken with allowance for the anisotropy of elastic constants of the KDP crystal. To compare the calculated and experimental data, it is necessary to carry out, by full analogy with Eq. (5), averaging over (i) the reflection curve of the collimator crystal, (ii) dispersion, (iii) two polarizations of incident radiation, and (iv) the angle ψ.

The calculated shapes of rocking curves corresponding to the elastic and inelastic scattering are shown in Fig. 4 for the KDP (280) reflection. The interference pattern is clearly observed for both scattering channels. Note that the occurrence of interference for the phonon-induced ICS directly follows from Eq. (10). In the case under consideration, both interference patterns are similar, although the amplitude of the interference feature is slightly smaller for the inelastic scattering than in the purely elastic case. However, whereas the elastic interference pattern is fully determined by the triplet phase (1), the inelastic scattering depends also on the relations between the reciprocal lattice vectors involved in the multiple diffraction [see Eq. (10)].

As regards the comparison with the experiment, one can see from Eq. (3) that the rocking curve calculated for the (280) reflection with account taken of the contributions from the elastic and inelastic scattering channels describes the experimental data rather well. The average (over the angular interval near the Bragg angle) contribution of the phonon-induced ICS is about ~12%

of the total reflected intensity. One can, generally, find examples where the ICS shows up in the reflection curves much more pronouncedly than in the case considered above.

REFERENCES

1. S.-L. Chang, *Multiple Diffraction of X-rays in Crystals* (Springer-Verlag, Berlin, 1984).

2. K. Hümmer and H. W. Billy, Acta Crystallogr. A **38**, 841 (1982).

3. B. Post, Acta Crystallogr. A **39**, 711 (1983).

4. É. K. Kov'ev and V. I. Simonov, Pis'ma Zh. Éksp. Teor. Fiz. **43**, 244 (1986) [JETP Lett. **43**, 312 (1986)].

5. Q. Shen and R. Colella, Acta Crystallogr. A **44**, 17 (1988).

6. S.-L. Chang, H. E. King, M.-T. Huang, and Y. Gao, Phys. Rev. Lett. **67**, 3113 (1991).

7. A. Yu. Kazimirov, M. V. Kovalchuk, I. Yu. Kharitonov, *et al.*, Rev. Sci. Instrum. **63**, 1019 (1992).

8. A. Yu. Kazimirov, M. V. Koval'chuk, and V. G. Kon, Kristallografiya **39**, 258 (1994) [Crystallogr. Rep. **39**, 216 (1994)].

9. M. V. Kovalchuk, A. Kazimirov, V. Kon, *et al.*, Physica B (Amsterdam) **221**, 445 (1996).

10. E. Weckert and K. Hümmer, Acta Crystallogr. A **53**, 108 (1997).

11. W. H. Zachariasen, *Theory of X-ray Diffraction in Crystals* (Wiley, New York, 1945).

12. A. M. Afanas'ev, P. A. Aleksandrov, and R. M. Imamov, *X-ray Diffraction Diagnostics of Submicron Layers* (Nauka, Moscow, 1989).

13. K. D. Rouse and M. J. Cooper, Acta Crystallogr. A **25**, 615 (1969).

14. M. Sakata and J. Harada, Acta Crystallogr. A **32**, 426 (1976).

15. A. M. Afanas'ev, M. V. Koval'chuk, É. F. Lobanovich, *et al.*, Kristallografiya **26**, 28 (1981) [Sov. Phys. Crystallogr. **26**, 13 (1981)].

16. A. M. Afanas'ev, M. A. Chuev, R. M. Imamov, and A. A. Lomov, Kristallografiya **46**, 781 (2001) [Crystallogr. Rep. **46**, 707 (2001)].

17. A. V. Zozulya, M. V. Koval'chuk, V. V. Lider, and L. V. Samoĭlova, Poverkhnost (2002) (in press).

18. Z. G. Pinsker, *Dynamical Scattering of X-rays in Crystals* (Nauka, Moscow, 1974; Springer-Verlag, Berlin, 1978).

19. A. M. Afanas'ev, Yu. Kagan, and F. N. Chukhovskii, Phys. Status Solidi **28**, 287 (1968).

20. R. Köhler, W. Möhling, and H. Peibst, Phys. Status Solidi B **61**, 173 (1974).

21. A. M. Afanas'ev and S. L. Azizian, Acta Crystallogr. A **37**, 125 (1980).

22. L. D. Landau and E. M. Lifshitz, *Course of Theoretical Physics*, Vol. 3: *Quantum Mechanics: Non-Relativistic Theory* (Fizmatgiz, Moscow, 1963; Pergamon, New York, 1977).

Translated by V. Sakun

Collision of Rydberg Atom A** with Ground-State Atom B: Optical Potential[1]

G. V. Golubkov[1, *], A. Z. Devdariani[2], and M. G. Golubkov[1]

[1] Semenov Institute of Chemical Physics, RAS, Moscow, 117334 Russia
*e-mail: golubkov@chph.rus.ru
[2] Department of Optics and Spectroscopy, Institute of Physics, St. Petersburg State University, St. Petersburg, 199034 Russia
Received January 9, 2002; in final form, February 26, 2002

The method of optical potential was used to calculate the slow collision of Rydberg atom A** with ground-state atom B. As an example, calculations were carried out for the Na**(nl) + He system. © *2002 MAIK "Nauka/Interperiodica".*

PACS numbers: 34.10.+x; 34.20.Cf

In spite of the progress in solving some problems of the physics of Rydberg atom collisions, one of the most important problem, namely, elastic scattering, is still poorly understood, in contrast to the atomic scattering in the ground and low-lying excited states. The latter can be treated, in principle, using a close-coupling approximation on the basis of the adiabatic potential energy curves. However, for the Rydberg collisions, the inelastic transitions are not localized and the adiabaticity is broken. In this case, the three-particle approach seems to be most appropriate. This approach immediately leads to the effective energy-dependent two-particle optical potential. In this letter, the optical potential is derived for the elastic Rydberg atom collisions and a particular example of such potentials is given. In the standard theory, a nonlocal operator $\mathbf{V}_{opt}$ is introduced and the many-particle equation is constructed for its definition. This statement of the problem has a formal character, and it cannot be resolved without additional assumptions about the interacting system [1]. In this work, we consider a slow elastic collision of Rydberg atom A** ($n \gg 1$) with ground-state atom B (n is the principal quantum number of the Rydberg level). We restrict ourselves to the case where the total energy of the system is $E < 0$ and calculate the optical potential for a structureless B particle. The optical potential of the Na** (nl) + He system is calculated as an illustration.

The total energy of the system is ($\hbar = e = m_e = 1$)

$$E = -1/2\nu_l^2 + E_k, \qquad (1)$$

where $\nu_l = n - \mu_l$ is the effective principal quantum number, μ_l is the quantum defect, l is the electron angular momentum with respect to A$^+$, and E_k is the initial collision energy. The interaction potential U_{A+B} of ion

A$^+$ with atom B is assumed to be known. To solve the eigenvalue problem, we use the following integral equation for the level-shift operator $\boldsymbol{\tau}$ [2]:

$$\boldsymbol{\tau} = \mathbf{U}_{A+B}\mathbf{G}(E)\boldsymbol{\tau}. \qquad (2)$$

The interaction operator of the three-particle system (A$^+$–B) + free electron e^- is local and written as

$$\mathbf{U}_{A+B}(\mathbf{R}, \mathbf{R}'; \boldsymbol{\rho}, \boldsymbol{\rho}')$$
$$= (2\pi)^6 U_{A+B}(R)\delta(\mathbf{R} - \mathbf{R}')\delta(\boldsymbol{\rho} - \boldsymbol{\rho}'), \qquad (3)$$

where $\mathbf{R}$ and $\boldsymbol{\rho}$ are the A$^+$ ion and electron coordinates measured from atom B. The Green's operator $\mathbf{G}(E)$ describes the A** + B system without the interaction U_{A+B} and obeys the Dyson equation

$$\mathbf{G}(E) = \mathbf{G}_{A**B}(E) + \mathbf{G}_{A**B}(E)\mathbf{V}_{e^-B}\mathbf{G}(E), \qquad (4)$$

where $\mathbf{V}_{e^-B}$ is the operator of the e^-–B interaction, and the Green's operator $\mathbf{G}_{A**B}(E)$ describes the noninteracting A** + B system with a given energy E.

The energy-dependent operator of nonlocal optical interaction is introduced in the theory as

$$\boldsymbol{\tau} = \mathbf{V}_{opt}(E)\mathbf{G}_{A**B}(E)\boldsymbol{\tau}, \qquad (5)$$

$$\mathbf{V}_{opt}(E) = \mathbf{U}_{A+B} + \mathbf{U}_{A+B}\mathbf{G}_{A**B}(E)\mathbf{V}_{e^-B}\mathbf{G}(E)\mathbf{V}_{opt}(E). \qquad (6)$$

Using Eq. (4), the expression for the operator $\mathbf{G}$ in Eq. (6) can be rewritten as [2]

$$\mathbf{G} = \mathbf{G}_{A**B} + \mathbf{G}_{A**B}\mathbf{T}_{e^-B}\mathbf{G}_{A**B},$$

where $\mathbf{T}_{e^-B}$ is the collision operator between the weakly bound electron and atom B. This representation is exact. It is convenient to use the Heitler-type equation

---

[1] This article was submitted by the authors in English.

and transfer to the real scattering matrix $\mathbf{K}_{e^-\mathrm{B}}$ (which is constructed, as known, for standing waves)

$$\mathbf{T}_{e^-\mathrm{B}} = \mathbf{K}_{e^-\mathrm{B}} - i\mathbf{K}_{e^-\mathrm{B}}\mathbf{T}_{e^-\mathrm{B}}.$$

As a result, operator (6) takes the form

$$\mathbf{V}_{\mathrm{opt}} = \mathbf{U}_{\mathrm{A+B}} + \mathbf{U}_{\mathrm{A+B}}\mathbf{G}_{\mathrm{A**B}}$$
$$\times [(1 + i\mathbf{K}_{e^-\mathrm{B}})^{-1}\mathbf{K}_{e^-\mathrm{B}}]\mathbf{G}_{\mathrm{A**B}}\mathbf{V}_{\mathrm{opt}}. \tag{7}$$

It follows from Eq.(7) that the imaginary part of operator $\mathbf{V}_{\mathrm{opt}}$ appears due to the electron interaction with the perturbing atom B, leading to the virtual transitions accompanied by a change in its momentum and angular momentum. By definition, the function $\mathbf{G}_{\mathrm{A**B}}$ is a convolution

$$\mathbf{G}_{\mathrm{A**B}}(\mathbf{R}, \mathbf{R}'; E)$$
$$= \frac{1}{(2\pi)^3}\int e^{i\boldsymbol{\kappa}\mathbf{R}}\mathbf{G}_{\mathrm{A**}}(E - E_\kappa)e^{-i\boldsymbol{\kappa}\mathbf{R}'}d\boldsymbol{\kappa}, \tag{8}$$

$$E_\kappa = \kappa^2/2M_c,$$

where $\mathbf{G}_{\mathrm{A**}}$ is the Green's operator of the isolated Rydberg atom and M_c is the reduced mass of particles A^+ and B. Expanding Eq. (8) in terms of spherical harmonics, we have

$$\mathbf{G}_{\mathrm{A**B}}(E) = \frac{2}{\pi}Y_{\tilde{L}\tilde{M}}(\mathbf{R}/R)Y^*_{\tilde{L}\tilde{M}}(\mathbf{R}'/R)$$
$$\times \int_0^{\kappa_{\max}} j_{\tilde{L}}(\kappa R)j_{\tilde{L}}(\kappa R')\mathbf{G}_{\mathrm{A**}}(E - E_\kappa)\kappa^2 d\kappa. \tag{9}$$

Here, $\tilde{L}$ and $\tilde{M}$ are the momentum and its projection onto the vector $\mathbf{R} - \mathbf{R}'$, respectively; $j_L(x)$ is the Bessel spherical function of the first kind of order L; and $Y_{LM}(\theta, \varphi)$ is the spherical function. This expression is real, because, according to Eq. (1), the Green's function of Rydberg atom $\mathbf{G}_{\mathrm{A**}}$ is defined for negative energy and corresponds to the electron bound state in the entire region of electron coordinates and the coordinates of atom B. Since the main contribution to integral (9) comes from the classically allowed region, the maximum momentum is determined from the condition

$$0 \le E + \frac{1}{R} - \frac{\kappa^2}{2M_c}$$

and is equal to

$$\kappa_{\max} = \sqrt{2M_c(E + 1/R)}, \tag{10}$$

where $I_\mathrm{A}^{-1} \le R \le 2\nu_l^2$, and I_A is the ionization potential of atom A.

The behavior of a weakly bound electron near the perturbing atom B, i.e., at $\rho, \rho' \ll R$, is of greatest interest.

In this region, the following general representation takes place [2]:

$$\mathbf{G}_{\mathrm{A**}}(\boldsymbol{\rho}, \boldsymbol{\rho}'; \mathbf{R}, \varepsilon)$$
$$= \mathbf{G}_0^{(c)}(\boldsymbol{\rho}, \boldsymbol{\rho}'; \varepsilon) + 2\sum_{s, s'}|s\rangle\langle s'|g_{ss'}(\mathbf{R}, \varepsilon). \tag{11}$$

The matrix elements are

$$g_{ss'}(\mathbf{R}, \varepsilon)$$
$$= [p_e(\varepsilon)\cot\pi\nu(\varepsilon)\delta_{ss'} + \alpha_{LL'}^{ll'}(\mathbf{R}, \varepsilon)\delta_{M0}\delta_{M'0}]. \tag{12}$$

Here, $p_e(\varepsilon) = [2(\varepsilon + 1/R)]^{1/2}$ is the electron quasiclassical momentum; $\nu(e) = (-2\varepsilon)^{-1/2}$ is the effective principal quantum number; $|s\rangle$ is the electron wave function

$$|s\rangle = |lmLM\rangle = j_L(p_e\rho)Y_{lm}(\mathbf{R}/R)Y_{LM}(\theta, \varphi);$$

θ is the angle between the vectors $\mathbf{p}_e(\varepsilon)$ and $\boldsymbol{\rho}$; L and M are the electron orbital momentum with respect to atom B and its projection onto the vector $\mathbf{R}$, respectively; and $\mathbf{G}_0^{(c)}$ is the smooth part of the Coulomb Green's function

$$\mathbf{G}_0^{(c)}(\boldsymbol{\rho}, \boldsymbol{\rho}'; \varepsilon) = -\frac{\cos(p_e|\boldsymbol{\rho} - \boldsymbol{\rho}'|)}{2\pi|\boldsymbol{\rho} - \boldsymbol{\rho}'|}.$$

The matrix $\alpha_{LL'}^{ll'}(\mathbf{R}, \varepsilon)$ in Eq. (12) is defined as

$$\alpha_{LL'}^{ll'}(\mathbf{R}, \varepsilon) = 2\pi^2\sqrt{(2L + 1)(2L' + 1)}$$
$$\times \frac{(-1)^{l+l'+1}(\nu(\varepsilon))^3}{\sin^2\pi\nu(\varepsilon)}\frac{\tan\pi\nu(\varepsilon)\tan\pi\mu_l}{\tan\pi\nu(\varepsilon) + \tan\pi\mu_l} \tag{13}$$
$$\times \tilde{\varphi}_{L\varepsilon}^{(l)}(R)\tilde{\varphi}_{L'\varepsilon}^{(l')}(R)|Y_{lm}(\mathbf{R}/R)|^2\delta_{ll'},$$

where the radial wave functions

$$\tilde{\varphi}_{L\varepsilon}^{(l)}(R) = \begin{cases} Q_{l\varepsilon}(R, \nu), & L = 2k \\ Q_{l\varepsilon}(R, \nu - 1/2), & L = 2k + 1 \end{cases}$$
$$(k = 0, 1, 2 \ldots)$$

differ from each other by the phase shift $\pi/2$ and are expressed in terms of the Whittaker functions

$$Q_{l\varepsilon}(r, \nu) = \frac{W_{\nu, l+1/2}(2r/\nu)}{r\nu\sqrt{\Gamma(\nu - l)\Gamma(\nu + l + 1)}},$$

where $\Gamma(x)$ is the gamma function.

To find the explicit form of optical potential, we introduce the basis wave functions of the $(\mathrm{A}^+ + \mathrm{B}) +$ free electron system in the following form

$$|q(\mathbf{R}, \boldsymbol{\rho})\rangle = \frac{1}{(2\pi)^3}\exp[i(\mathbf{k}\mathbf{R} + \mathbf{p}_e(\varepsilon_k)\boldsymbol{\rho})].$$

Let us use the first-order perturbation theory and replace the operator $\mathbf{V}_{\mathrm{opt}}$ on the right-hand side of Eq. (6) by the local operator (3). Then, the optical potential is defined as the matrix element

$$V_{\mathrm{opt}} = \langle q|\mathbf{V}_{\mathrm{opt}}|q\rangle. \tag{14}$$
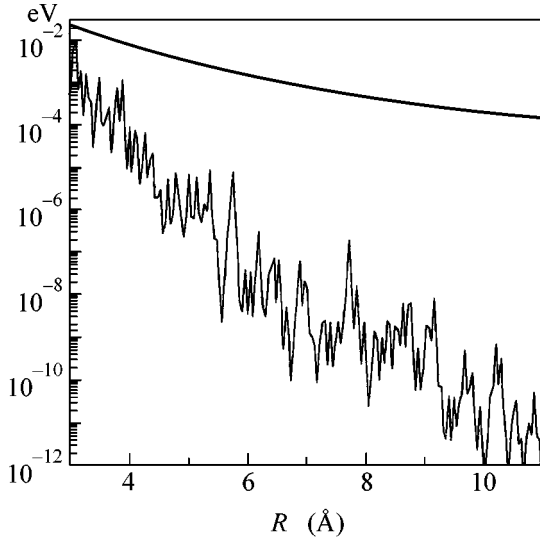
The dependence of negative value of interaction potential $-U_{Na^+He}$ (thick solid line) and Γ (thin solid line) on the interatomic distance R, as calculated for the Na(10d) + He system. The calculations were carried out for $E_k = 2.72 \times 10^{-2}$ eV and $\tilde{L} = 0$.

Integrating over the interatomic coordinates and using the symmetry property of operator

$$\langle s|K_{e^-B}|s'\rangle = (\mathbf{K}_{e^-B})_{ss'}\delta_{ss'},$$

one gets

$$V_{opt}(E, k, l, \tilde{L}, R) = U_{A+B}(R) + 2^{14}\pi^4 U_{A+B}^2(R)$$

$$\times |Y_{\tilde{L}0}(\theta = 0)|^4 [(1 - i\mathbf{K}_{e^-B})^{-1}\mathbf{K}_{e^-B}]_{LL}$$

$$\times \left\{ \int_0^{\kappa_{max}} \kappa^2 d\kappa \kappa'^2 d\kappa' j_{\tilde{L}}^2(\kappa R) j_{\tilde{L}}^2(\kappa' R) \right. \tag{15}$$

$$\times \left. \sum_{mM} g_{ss}(R, \varepsilon_\kappa)g_{ss}^*(R, \varepsilon_{\kappa'})|Y_{lm}(\mathbf{R}/R)|^2|Y_{LM}(\boldsymbol{\rho}/\rho)|^2 \right\},$$

where $\varepsilon_\kappa = E - \kappa^2/2M_c$ and $\tilde{L}$ is the initial orbital momentum of colliding particles A** and B. The spherical function $Y_{lm}(\mathbf{R}/R)$ in Eqs. (13) and (15) should be replaced by $Y_{lm}(0)$. This is due to the fact that, under condition $l \ll v_l^{3/2}$, the electron motion near atom B is described by a plane wave with the wave vector directed along the vector $\mathbf{R}$.

Under the conditions considered ($n \gg 1$), it is sufficient to restrict oneself to the case $L = 0$. The $\mathbf{K}_{e^-B}$ matrix can be replaced by the $\mathbf{K}_{e^-B}^{(0)}$ matrix of a free electron scattering with energy $\varepsilon_e = E + 1/R - \kappa^2/2M_c$, because the Rydberg electron behaves near atom B as a free particle [3]. Assuming for simplicity that atom B is a structureless particle, one can restrict oneself only by the first term in the long-wavelength expansion of the $(\mathbf{K}_{e^-B}^{(0)})_{ss}$ amplitude, i.e., by the e^-–B scattering length α [4]. In this case, Eq. (14) for a given E_k takes the simple form

$$V_{opt} = U_{A+B} + \Delta - i\Gamma/2,$$

$$\Delta(E, n, l, \tilde{L}, R) = \frac{\pi a}{1 + a^2}S_{l\tilde{L}}(E, n, R), \tag{16}$$

$$\Gamma(E, n, l, \tilde{L}, R) = \frac{2\pi a^2}{1 + a^2}S_{l\tilde{L}}(E, n, R),$$

where the factor $S_{l\tilde{L}}(E, n, R)$ is equal to

$$S_{l\tilde{L}}(E, n, R) = \left[64\pi U_{A+B}(R)Y_{\tilde{L}0}^2(\theta = 0)Y_{l0}(\theta = 0) \right.$$

$$\left. \times \int_0^{\kappa_{max}} j_{\tilde{L}}^2(\kappa R)g_{ss}(R, \varepsilon_\kappa)\kappa^2 d\kappa \right]^2. \tag{17}$$

In accordance with Eq. (16), the real part of the shift is proportional to the scattering length a and depends on its sign. The width Γ is proportional to a^2 and is always positive. Note that the expression $S_{l\tilde{L}}(E, n, R)$ is an oscillating function of distance R and equals zero outside the classically allowed region of electron motion [i.e., at $R \ge (-E)^{-1}$]. It is easy to see that the shift and broadening of ion potential are nonzero in the limit $k \longrightarrow 0$. This result is physically understandable, because the weakly bound electron may always undergo a virtual transition to the lower energy state (with smaller principal quantum number).

As an illustration, the potential U_{A+B} [5] and the width of the optical potential are shown in the figure as functions of the interatomic distance for the Na(nl) + He system with $n = 10$, $\tilde{L} = 0$, and $l = 2$ at energy $E_k = 10^{-3}$, as calculated by Eqs. (16) and (17) with $a = 1.15$ [6].

REFERENCES

1. N. F. Mott and H. S. W. Massey, *The Theory of Atomic Collisions* (Clarendon, Oxford, 1965; Mir, Moscow, 1969).
2. G. V. Golubkov and G. K. Ivanov, Z. Phys. A **319**, 17 (1984).
3. V. A. Alekseev and I. I. Sobelman, Zh. Éksp. Teor. Fiz. **49**, 1274 (1965) [Sov. Phys. JETP **22**, 882 (1966)].
4. T. O'Malley, L. Sprach, and L. Rosenberg, Phys. Rev. **125**, 130 (1962).
5. M. Krauss, P. Maldonado, and A. C. Wahl, J. Chem. Phys. **54**, 4944 (1971).
6. B. M. Smirnov, *Physics of Weakly Ionized Gas* (Nauka, Moscow, 1972).

Deformation-Induced Thermomagnetic Effects in a Twisted Weak-Link-Bearing Superconductor[1]

S. A. Sergeenkov

Bogoliubov Laboratory of Theoretical Physics, Joint Institute for Nuclear Research, Dubna, 141980 Russia
Received February 21, 2002

Based upon the recently introduced thermophase and piezophase mesoscopic quantum effects in Josephson junctions, several novel phenomena in a twisted superconductor (containing a small annular SIS-type contact) under the influence of a thermal gradient and applied magnetic field are predicted. Namely, we consider a torsional analog of Josephson piezomagnetism (and related magnetomechanical effect), as well as the possible generation of a heat-flux-induced magnetic moment in a weakly coupled superconductor under torsional deformation (analog of Zavaritskii effect) along with the concomitant phenomena of piezothermopower and piezothermal conductivity. The conditions under which the predicted effects can be experimentally measured in conventional superconductors and nanostructure materials with implanted Josephson contacts are discussed. © 2002 MAIK "Nauka/Interperiodica".

PACS numbers: 74.50.+r; 74.62.Fj; 74.80.Bj; 75.80.+q

In 1972, Zavaritskii [1] observed for the first time a very interesting phenomenon (the so-called deformation-induced thermomagnetic effect): the appearance of a heat flux Q-induced magnetic field $\Delta H = H_q(\alpha)Q$ in rodlike tin samples (both in the normal and superconducting state) under a torsional deformation $\mathcal{M}$ (related to a torsional angle $\alpha(\mathcal{M}) = \mathcal{M}/C_0$, where C_0 is the respective elastic modulus of the material). A tangible value of ΔH was registered under the maximum load of $\mathcal{M} = 0.2 N/m$ (which corresponds to $\alpha = 0.01$ rad/cm). This phenomenon was attributed to generation of circular (nonpotential) currents in a deformed sample (which, in turn, lead to observable magnetic moments; see [2] for discussion) and was further investigated by Lebedev [3] on the basis of kinetic theory.

At the same time, in response to the rapidly growing interest in the important applications of Josephson and proximity effects in novel mesoscopic quantum devices (such as, e.g., quantum computers), substantial progress has been made recently in the measuring of (and manipulating with) extremely small magnetic fields, thermal gradients, and mechanical deformations [4, 5].

Based upon the recently introduced thermophase [6, 7] and piezophase [8, 9] effects (suggesting, respectively, the direct influence of a thermal gradient and an applied stress on the phase difference through a Josephson junction), in this Letter we discuss an analog of the above-mentioned Zavaritskii effect in a twisted superconductor containing a single SIS-type contact and its possible realization in conventional superconductors. Moreover, we also consider the concomitant phenomena of Josephson piezomagnetism and the magnetomechanical effect, as well as the change of transport properties of the SIS-type junction under torsional deformation (piezothermopower and piezothermal conductivity).

The model. To follow the original paper of Zavaritskii [1] as close as possible, let us consider a tin rod (of length L and radius R) with an annular Sn–SnO–Sn contact [10] incorporated into the middle of the rod (due to the high pliability of tin, it should be quite easy to achieve), with a thin insulating SnO layer (of thickness l). Assuming the usual cylindrical geometry (with the z axis taken along the rod length and $A = \pi R^2$ being the junction area), we can present the total Josephson energy on the contact as follows (for the sake of simplicity, in this paper we will concentrate on zero-temperature effects, only and will ignore the role of Coulomb interaction effects, assuming that the grain charging energy $E_c \ll E_J$, where $E_c = e^2/2C_J$, with C_J being the capacitance of the junction):

$$E_J = \int_0^\tau \frac{dt}{\tau} \int_{-R}^R \frac{dx}{A} \int_{-\sqrt{R^2-x^2}}^{\sqrt{R^2-x^2}} dy \int_0^L \frac{dz}{L}[\mathcal{H}(\mathbf{x}, t)], \qquad (1)$$

where the local Josephson energy is given by

$$\mathcal{H}(\mathbf{x}, t) = J[1 - \cos\phi(\mathbf{x}, t)], \qquad (2)$$

with the resulting phase difference

$$\phi(\mathbf{x}, t) = \phi_0 + \frac{2\pi d B x}{\Phi_0} + \alpha(\mathcal{M})z + \frac{2\pi S_0 \nabla T \mathbf{x}}{\Phi_0}t \qquad (3)$$

accounting for the change of the initial phase difference ϕ_0 under the influence of an applied magnetic field $\mathbf{B} =$

(0, B, 0), thermal gradient $\nabla T = (\nabla_x T, 0, \nabla_z T)$, and applied torsional deformation $\mathcal{M}$ (through the corresponding torsional angle $\alpha(\mathcal{M})$) taken along the z axis.

Here, $\Phi_0 = h/2e$ is the quantum of flux with h being Planck's constant and e the electronic charge, $d = 2\lambda_L + l$ is the junction size with λ_L being the London penetration length, τ is a characteristic Josephson time [9], J is the Josephson coupling energy, and S_0 is the field-free thermoelectric power (Seebeck coefficient) on the junction.

The origin of the third term in Eq. (3) is quite obvious. Indeed, under the influence of a homogeneous torsional deformation $\mathcal{M}$, the superconducting phase difference will change with z as follows: $d\phi/dz = (d\phi/d\theta)(d\theta/dz) = N\alpha(\mathcal{M})$, where [11] $\alpha(\mathcal{M}) \equiv d\theta/dz = \mathcal{M}/C_0$ is the corresponding torsional angle variable and $N \equiv d\phi/d\theta$ is the geometrical factor (in most cases [8], $N \simeq 1$). As a result, the superconducting phase difference will acquire the additional contribution $\delta\phi(z) = \alpha(\mathcal{M})z$. (Notice that practically the same result can be obtained by using the arguments from [9] and invoking an analogy with a conventional linear torsional piezoelectric effect, which predicts [12] $P(\mathcal{M}) = a\mathcal{M}$ for an induced electric polarization.)

To neglect the influence of the self-field effects and ensure uniformity of the applied deformation $\mathcal{M}$ (and the related torsional angle $\theta(L) \equiv \alpha(\mathcal{M})L$), we have to assume that $\lambda_J > R$ and $L \gg R$, where $\lambda_J = \sqrt{\Phi_0/2\pi d\mu_0 j_c}$ is the Josephson penetration depth with j_c being the Josephson critical current density. As we will see below, these conditions can be met reasonably well experimentally.

Torsional piezomagnetic effect. Before turning to the main subject of this paper, let us briefly discuss two preliminary issues: (i) deformation-induced behavior of the Josephson current and (ii) torsional analog of Josephson piezomagnetism (which takes place in a twisted SIS-type contact and manifests itself through the appearance of deformation-induced susceptibility) in the absence of a thermal gradient through the junction ($\nabla T = 0$). Recalling the definition of the Josephson current density $j_s(\mathbf{x}) = j_c \sin\phi(\mathbf{x}, 0)$ in this particular case, Eq. (3) gives

$$I_s(B, \theta) = 2I_c\left[\frac{J_1(B/B_0)}{B/B_0}\right]\left(\frac{\sin\theta}{\theta}\right) \qquad (4)$$

for the maximum (with $\phi_0 = \pi/2$) Josephson current in a twisted cylindrical contact (under a torsional deformation $\mathcal{M}$ producing angle $\theta = \mathcal{M}L/C_0$) with $I_c = j_cA = 2eJ/\hbar$. Here, $B_0 = \Phi_0/2\pi dR$ is a characteristic Josephson field of annular contact, and $J_1(x)$ is the Bessel function. We notice that, as a function of torsional angle θ, the induced current $I_s(B, \theta)$ follows a quasiperiodic Fraunhofer-like pattern and reduces to the well-known [13] result for the magnetic-field dependence of an annular

Josephson contact upon the removal of a mechanical load (in the deformation-free case when $\theta \longrightarrow 0$).

Moving on to the second issue, we find that, in addition to the above-discussed angle-dependent Josephson current, an induced magnetic moment will appear in a twisted contact (torsional piezomagnetic effect)

$$M_s(B, \theta) \equiv -\frac{1}{V}\left[\frac{\partial E_J}{\partial B}\right]_{\nabla T = 0}, \qquad (5)$$

where $V = AL$ is the sample volume.

To capture the very essence of this effect, in what follows we assume for simplicity that an *unloaded sample* does not possess any spontaneous magnetization at zero magnetic field (that is $M_s(0, 0) = 0$) and that its Meissner response to a small applied field B is purely diamagnetic (that is $M_s(B, 0) \simeq -B$). According to Eqs. (1)–(5), this condition implies $\phi_0 = 2\pi m$ for the initial phase difference with $m = 0, \pm1, \pm2, \dots$. As a result, for the change of magnetization under torsional deformation, we obtain

$$M_s(B, \theta) = -M_0 f_1(B/B_0) g_0(\theta). \qquad (6)$$

Here,

$$M_0 = 2J/VB_0, \quad f_1(x) = -\frac{d}{dx}[f_0(x)],$$

$$f_0(x) = J_1(x)/x, \quad g_0(x) = \sin x/x.$$

For the low-field (Meissner) region, we can linearize the above equation and define the deformation-induced angle-dependent susceptibility $\chi(\theta)$. Indeed, for $B \ll B_0$, Eq. (6) gives $M_s(B, \theta) \simeq \chi(\theta)B$, where $\chi(\theta) = -\chi_0 g_0(\theta)$ with $\chi_0 = J/4VB_0^2$. As follows from the above equations, the superconducting (Meissner) phase of piezomagnetization $M_s(B, \theta)$ (and the corresponding susceptibility $\chi(\theta)$) gradually dwindles with increasing angle θ, shifting towards the paramagnetic phase (and reaching it eventually at $\theta \simeq \pi$).

Magnetomechanical effect. Let us consider the converse (to piezomagnetism) magnetomechanical effect, that is, the field-induced change of torsional angle $\theta_s(B, \mathcal{M})$ (and corresponding compliance $C_s^{-1}(B)$; see below). In view of Eqs. (1)–(3), we obtain

$$\theta_s(B, \mathcal{M}) \equiv \left[\frac{\partial E_j}{\partial\mathcal{M}}\right]_{\nabla T = 0} = \theta_0 f_0(B/B_0) g_1(\mathcal{M}/\mathcal{M}_0), \quad (7)$$

where $\theta_0 = J/\mathcal{M}_0$ with $\mathcal{M}_0 = C_0/L$ and $g_1(x) = -(d/dx)[g_0(x)]$.

We notice that in the absence of an applied magnetic field (when $B = 0$) the above equation establishes the so-called "torque–angle" relationship (torsional analog of the "stress–strain" law [8]) for a twisted weak-link-bearing superconductor $\theta_s(0, \mathcal{M}) = \theta_0 g_1(\mathcal{M}/\mathcal{M}_0)$. For sufficiently small torsional deformations (when $\mathcal{M} \ll \mathcal{M}_0$, which is usually the case in realistic experiments),

the above model relationship reduces to the more familiar Hooke law, $\theta_s(0, \mathcal{M}) = \mathcal{M}L/C_s(0)$ with $C_s(0) = (3C_0/JL)C_0$ being the appropriate (zero-field) elastic modulus (inverse torsional compliance), whose magnetic-field dependence is governed by the following equation:

$$\frac{1}{C_s(B)} \equiv \frac{1}{L}\left[\frac{\partial\theta_s(B, \mathcal{M})}{\partial\mathcal{M}}\right]_{\mathcal{M}=0} = \frac{1}{C_s(0)}\left[\frac{2J_1(B/B_0)}{B/B_0}\right]. \quad (8)$$

It would be rather interesting to try to observe the above-discussed piezomagnetic and magnetomechanical effects (including torsional analog of the paramagnetic Meissner effect [9]) in a twisted weak-link-containing superconductor.

Deformation-induced thermomagnetic effects. Let us now turn to the main subject of this paper and consider the influence of a thermal gradient ∇T on the above-discussed piezomagnetic and magnetomechanical effects. Hereafter, we restrict our consideration to the case of small values of the applied thermal gradient ∇T, which leads to linear thermoelectric effects (for a discussion of possible nonlinear Seebeck effects in Josephson junctions and granular superconductors, see [7]). For a thermal gradient applied normally and parallel to the torsional deformation [see Eq. (3)], we obtain two contributions (transverse and longitudinal) for the deformation-induced thermomagnetization emerging in the vicinity of the Josephson contact:

$$\Delta M(\theta, B, \nabla T) \equiv -\frac{1}{V}\left[\frac{\partial E_J}{\partial B}\right]_{\nabla T \neq 0} \quad (9)$$

$$= M_\perp^q(\theta, B)\nabla_x T + M_\parallel^q(\theta, B)\nabla_z T,$$

where

$$M_\perp^q(\theta, B) = M_{0\perp}^q f_2(B/B_0)g_0(\theta) \quad (10)$$

and

$$M_\parallel^q(\theta, B) = M_{0\parallel}^q f_1(B/B_0)g_1(\theta). \quad (11)$$

Here, $M_{0\parallel}^q = (L/R)M_{0\perp}^q$ with $M_{0\perp}^q = 2eJS_0\tau R/B_0V\hbar$ and $f_2(x) = (d/dx)[f_1(x)]$.

We notice that, within the geometry adopted in this paper, the true analog of the Zavaritskii effect is given by a zero-field limit of the transverse (paramagnetic) contribution, $M_\perp^q(\theta, 0) = (1/8)M_{0\perp}^q(\sin\theta/\theta)$. Its evolution with the torsional angle follows the corresponding behavior of the induced susceptibility $\chi(\theta)$ [cf. Eq. (6)], and, thus, it also undergoes a "diamagnetic–paramagnetic" transition upon reaching a critical angle $\theta_c \simeq \pi$. On the other hand, the field-dependent longitudinal component $M_\parallel^q(\theta, B)$ changes with θ linearly for $\theta \ll 1$. It describes the appearance of the deformation-induced thermomagnetic component normal to the applied magnetic field $\mathbf{B} = (0, B, 0)$. It disappears when $B \longrightarrow 0$, and for a nonzero fields it closely follows the behavior

of the (initially diamagnetic) torsional piezomagnetization $M_s(B, \theta)$ considered in the previous section [cf. Eq. (6)].

Likewise, for a thermal gradient applied normally and parallel to the torsional deformation [see Eq. (3)], we obtain two contributions for the heat-flux-induced magnetomechanical effect

$$\Delta\theta(\mathcal{M}, B, \nabla T) \equiv \left[\frac{\partial E_J}{\partial\mathcal{M}}\right]_{\nabla T \neq 0} \quad (12)$$

$$= \theta_\perp^q(\mathcal{M}, B)\nabla_x T + \theta_\parallel^q(\mathcal{M}, B)\nabla_z T,$$

where

$$\theta_\perp^q(\mathcal{M}, B) = \theta_{0\perp}^q f_1(B/B_0)g_1(\mathcal{M}/\mathcal{M}_0) \quad (13)$$

and

$$\theta_\parallel^q(\mathcal{M}, B) = \theta_{0\parallel}^q f_0(B/B_0)g_2(\mathcal{M}/\mathcal{M}_0). \quad (14)$$

Here, $\theta_{0\parallel}^q = (L/R)\theta_{0\perp}^q$ with $\theta_{0\perp}^q = 2eS_0JR\tau/\hbar\mathcal{M}_0$ and $g_2(x) = -(d/dx)[g_1(x)]$.

Once again, the true (deformation-free) heat-flux-induced magnetomechanical effect is given by the zero-deformation limit of the longitudinal component $\theta_\parallel^q(0, B)$, while the small-angle expansion of the transverse component describes a thermal analog of the Hooke law $\theta_\perp^q(\mathcal{M}, B) \simeq \mathcal{M}/C_\perp^q(B)$, with $C_\perp^q(B)$ being the appropriate compliance coefficient.

Piezothermopower. Let us now briefly discuss one more interesting phenomenon of *piezothermopower*, which can occur in a twisted superconducting rod with a SIS-type junction. According to Eqs. (1)–(3), the transverse and longitudinal contributions to a (magnetic-field-dependent) change of the junction's Seebeck coefficients under torsional deformation are

$$\Delta S_\perp(\theta, B) \equiv -\frac{1}{eR}\left[\frac{\partial E_J}{\partial\nabla_x T}\right] = S_J f_1(B/B_0)g_0(\theta) \quad (15)$$

and

$$\Delta S_\parallel(\theta, B) \equiv -\frac{1}{eL}\left[\frac{\partial E_J}{\partial\nabla_z T}\right] = -S_J f_0(B/B_0)g_1(\theta) \quad (16)$$

with $S_J = (2\tau J/\hbar)S_0$.

Like in the previous paragraph, the deformation-free transverse component $\Delta S_\perp(0, B)$ describes the evolution of conventional thermopower in an unloaded $\theta = 0$ sample with an applied magnetic field, while the true piezothermopower is given by the zero-field limit of the longitudinal component $\Delta S_\parallel(\theta, 0)$. Moreover, the above analysis allows us to introduce a deformation-induced AC Josephson effect (as a generalization of the more familiar thermal AC effect [14]) in a twisted SIS-contact-bearing superconductor. Indeed, as soon as the thermal current exceeds the critical current, which will happen when ΔT becomes larger than $\Delta T_c(\theta, B) =$

$I_c R_n / \Delta S_\parallel(\theta, B)$ (where R_n is the normal-state resistance), a new type of Josephson generation with frequency $\omega(\theta, B) = 2e\Delta S_\parallel(\theta, B)\Delta T/\hbar$ should occur in the junction area (see below for more discussion).

Piezothermal conductivity. Finally, let us briefly consider the influence of mechanical deformation on magnetothermal conductivity of the twisted weak-link-bearing superconducting rod. To this end, we recall that the local heat-flux density $\mathbf{q}(\mathbf{x}, t)$ is related to the local Josephson energy density $\mathcal{H}(\mathbf{x}, t)$ via the energy conservation law

$$\nabla \mathbf{q}(\mathbf{x}, t) + \dot{\mathcal{H}}(\mathbf{x}, t) = 0, \qquad (17)$$

where $\dot{\mathcal{H}} = \partial\mathcal{H}/\partial t$.

The above equation allows us to introduce an effective thermal flux

$$\mathbf{Q}(t) \equiv \frac{1}{V}\int d^3x\, \mathbf{q}(\mathbf{x}, t) = \frac{1}{V}\int d^3x\, \dot{\mathcal{H}}(\mathbf{x}, t)\mathbf{x}, \qquad (18)$$

which, in turn, is related to the thermal conductivity tensor $\kappa_{\alpha\beta}$ as ($\{\alpha, \beta\} = x, y, z$)

$$\langle Q_\alpha \rangle \equiv \frac{1}{\tau}\int_0^\tau dt\, Q_\alpha(t) = -\kappa_{\alpha\beta}\nabla_\beta T. \qquad (19)$$

Straightforward calculations based on Eqs. (1)–(3) yield the following explicit expressions for nonzero components of the thermal conductivity tensor:

$$\kappa_{xx}(\theta, B) = \kappa_0\left(\frac{R}{L}\right)J_1'(B/B_0)g_c(\theta),$$

$$\kappa_{xz}(\theta, B) = \kappa_{zx}(\theta, B) = \kappa_0 J_1(B/B_0)g_c'(\theta) \qquad (20)$$

$$\kappa_{zz}(\theta, B) = \kappa_0\left(\frac{L}{R}\right)J_0(B/B_0)g_c''(\theta),$$

where $\kappa_0 = 8eS_0JRL/hV$, $J_1'(x) = J_0(x) - J_1(x)/x$, with $J_n(x)$ being the corresponding Bessel functions, $g_c(x) = (1 - \cos x)/x$,

$$g_c'(x) = \frac{d}{dx}[g_c(x)], \quad g_c''(x) = \frac{d^2}{dx^2}[g_c(x)].$$

For small torsional deformations (with $\theta \ll 1$), $g_c(\theta) \simeq \theta/2$, $g_c'(\theta) \simeq (1 - \theta^2/4)/2$, and $g_c''(\theta) \simeq \theta/4$. So, $\kappa_{xz}(0, B)$ describes conventional (deformation-free) magnetothermal conductivity in an unloaded junction [15], while true (magnetic-field-free) piezothermal conductivity is given by $\kappa_{xx}(\theta, 0)$ and $\kappa_{zz}(\theta, 0)$ components (both increasing linearly with θ for small angles). In a sense, the piezothermal conductivity introduced here is a converse effect with respect to the original Zavaritskii effect [1, 2] and it seems very interesting to try to realize it experimentally using tin rods (with and without weak links).

Discussion. To estimate the magnitudes of the predicted effects, we make use of the fact that for thermoelectric processes the characteristic time τ is related to the thermal AC frequency $\omega_T = 2eS_0\Delta T/\hbar$ (assuming $\nabla_x T \simeq \Delta T/R$ and $\nabla_z T \simeq \Delta T/L$) as $\tau = 2\pi/\omega_T$. As a result, the deformation-induced thermomagnetic field (Josephson analog of Zavaritskii effect) reads

$$\Delta H_\perp \equiv 4\pi M_\perp^q(\theta, 0)\nabla_x T \simeq H_J\left(\frac{R}{L}\right)\left(\frac{\sin\theta}{\theta}\right), \qquad (21)$$

where $\mu_0 H_J = \Phi_0/2\pi\lambda_J^2$ is the critical Josephson field.

Furthermore, combining the experimental parameters for the Sn–SnO–Sn annular Josephson junction considered by Matisoo [10] (namely, $R_n = 10^{-9}\,\Omega$, $j_c(0) = 10^4$ A/m^2, $\lambda_L(0) = 40$ nm, and $\lambda_J(0) = 5$ mm) with typical parameters from Zavaritskii experiments on tin rods [1, 2] (namely, $2R = 5$ mm, $L = 8$ cm, and $\theta_{max} = 0.1$ rad), we obtain $\Delta B_\perp = \mu_0\Delta H_\perp \simeq 10^{-12}$ T, which is equivalent to quite a sizable value of the deformation-induced thermomagnetic flux through the junction $\Delta\Phi_\perp = \pi R^2\Delta B_\perp \simeq 10^{-2}\Phi_0$. The same set of parameters yields $B_0 = \Phi_0/2\pi dR \simeq 10^{-6}$ T and $B_J = \Phi_0/2\pi\lambda_J^2 \simeq 10^{-10}$ T for estimates of characteristic and critical Josephson fields, respectively. Finally, using some typical [14] experimental data describing the physics of conventional Josephson contacts (with $S_0 \simeq 10^{-8}$ V/K and $\Delta T \simeq 10^{-4}$ K), we can estimate the orders of magnitude of the piezothermal conductivity and deformation-induced AC Josephson generation (related to piezo-thermopower). The result is as follows: $\kappa_{zz}(\theta, 0) \simeq (2eS_0JL^2/hV)\theta \simeq (2/\pi)S_0j_c\theta \simeq 10^{-2}$ W/mK and $\omega(\theta, 0) = 2e\Delta S_\parallel(\theta, 0)\Delta T/\hbar \simeq (\omega_J\tau/3)\theta\omega_T \simeq 10^{11}$ Hz, where $\omega_J = 2J/\hbar \simeq 10^{12}$ Hz and $\omega_T = 2eS_0\Delta T/\hbar \simeq 1$ kHz are characteristic (Josephson and thermal, respectively) frequencies. The above estimates suggest a quite optimistic possibility observing the predicted effects experimentally through a comparative study of conventional superconductors with and without SIS-type junctions.

At the same time, to check the validity of some other interesting predictions (like Fraunhofer patterns given by a set of $g_n(\theta)$ functions; see the text), much larger torsional deformations (reaching critical angles on the order of $\theta_c \simeq \pi$) are needed. Hopefully, this will become possible in the near future with the further development of experimental techniques and new technologies for manufacturing nanostructure superconducting materials with implanted atomic-scale Josephson junctions and other weak links [4].

In conclusion, a few novel mesoscopic quantum phenomena which are expected to occur in a weak-link-bearing superconductor under the influence of torsional deformation, thermal gradient, and applied magnetic field were presented, including the angle-dependent Josephson current, torsional piezomagnetism, magne-

tomechanical effect, an analog of the Zavaritskii effect (appearance of a deformation-induced thermomagnetic moment in zero magnetic field), piezothermopower (and the related deformation-induced AC Josephson effect), and piezothermal conductivity. The observability of the predicted effects using conventional superconductors, as well as novel materials with well-controlled mesoscopic Josephson junctions, has been discussed.

REFERENCES

1. N. V. Zavaritskii, Pis'ma Zh. Éksp. Teor. Fiz. **16**, 99 (1972) [JETP Lett. **16**, 67 (1972)].

2. N. V. Zavaritskii, Zh. Éksp. Teor. Fiz. **67**, 1210 (1974) [Sov. Phys. JETP **40**, 601 (1975)].

3. V. V. Lebedev, Zh. Éksp. Teor. Fiz. **67**, 1161 (1974) [Sov. Phys. JETP **40**, 577 (1975)].

4. *Proceedings of the Conference "Mesoscopic and Strongly Correlated Electron Systems," Chernogolovka, 1997*, Ed. by V. F. Gantmakher and M. V. Feigel'man; Usp. Fiz. Nauk **168** (2) (1998) [Phys. Usp. **41** (2) (1998)]; *Mesoscopic and Strongly Correlated Electron Systems-II*, Ed. by M. V. Feigel'man, V. V. Ryazanov, and V. B. Timofeev; Phys. Usp. (Suppl.) **44** (10) (2001).

5. S. Sergeenkov, in *Studies of High Temperature Superconductors*, Ed. by A. Narlikar and F. Araujo-Moreira (Nova Science, New York, 2001), Vol. 39, pp. 117–131.

6. G. D. Guttman, B. Nathanson, E. Ben-Jacob, *et al.*, Phys. Rev. B **55**, 12691 (1997).

7. S. Sergeenkov, Pis'ma Zh. Éksp. Teor. Fiz. **67**, 650 (1998) [JETP Lett. **67**, 680 (1998)].

8. S. Sergeenkov, J. Phys.: Condens. Matter **10**, L265 (1998).

9. S. Sergeenkov, Pis'ma Zh. Éksp. Teor. Fiz. **70**, 36 (1999) [JETP Lett. **70**, 36 (1999)].

10. J. Matisoo, J. Appl. Phys. **40**, 1813 (1969).

11. L. D. Landau and E. M. Lifshitz, *Course of Theoretical Physics*, Vol. 7: *Theory of Elasticity* (Nauka, Moscow, 1982; Pergamon, New York, 1986).

12. L. D. Landau and E. M. Lifshitz, *Course of Theoretical Physics*, Vol. 8: *Electrodynamics of Continuous Media* (Nauka, Moscow, 1982; Pergamon, New York, 1984).

13. A. Barone and G. Paterno, *Physics and Applications of the Josephson Effect* (Wiley, New York, 1982; Mir, Moscow, 1984).

14. G. I. Panaitov, V. V. Ryazanov, A. V. Ustinov, *et al.*, Phys. Lett. A **100**, 301 (1984).

15. S. Sergeenkov and M. Ausloos, Phys. Rev. B **48**, 4188 (1993).

Nematic Emulsion in a Magnetic Field

B. Lev, A. Nych, U. Ognysta, D. Reznikov, S. Chernyshuk, and V. Nazarenko*

Institute of Physics, National Academy of Sciences of Ukraine, Kiev-39, 03650 Ukraine
* *e-mail: vnazaren@iop.kiev.ua*
Received February 22, 2002

Magnetic-field-induced mutual transformations of a hexagonal structure into linear chains were experimentally observed in a system of glycerol droplets freely suspended in the layer of a nematic liquid crystal with hybrid orientation. A qualitative explanation is suggested for the observed effect. © *2002 MAIK "Nauka/Interperiodica".*

PACS numbers: 61.30.Gd

It is known that the droplets of an isotropic liquid suspended in a nematic liquid crystal (NLC) interact with one another [1–4]. This interaction is anisotropic, and its nature is closely connected to the elastic properties of the mesophase medium. For example, the droplets of an isotropic liquid suspended in an NLC induce elastic distortions of the director. The character of these distortions and, correspondingly, the type of the defect produced by the droplet depend on the boundary conditions at the droplet surface [5–11]. The homeotropic director orientation at the droplet is characterized by the presence of a hyperbolic hedgehog or a disclination ring near the droplet. The type of one or another defect depends on both the director distribution in the whole sample and the cohesive energy. In the case of planar orientation, two boojums were observed at the droplet poles. The character of interaction between the droplets is determined by the structure of the defects or, strictly speaking, by the symmetry of the director distribution around the droplet [4]. In particular, a droplet with normal boundary conditions and the corresponding hyperbolic hedgehog have a dipolar symmetry in a homogeneous nematic layer; as a result, the interaction between the droplets has a dipolar and/or quadrupolar character [7, 8]. For a system of such droplets suspended in a nematic matrix, the formation of droplet chains along the director direction was experimentally observed in [12]. In this example, the dipolar attraction was responsible for the linear ordering of droplets. Of particular interest is the case where not only the quadrupolar but also the dipolar symmetry is broken, e.g., due to inhomogeneous global director distribution. In this case, the droplet ordering becomes more intricate [8–13]. In [13], the stable hexagonal crystal structure formed by the glycerol droplets in a nematic layer with hybrid orientation is described. In this work, we report on the experimental study of the behavior of hexagonal droplet structures in a magnetic field.

Experiments were carried out with a ~5-mm-thick layer of pure glycerol covered with a layer of 5CB NLC. A cuvette with glycerol and liquid crystal was placed in a thermostat, and the system was observed using a microscope. The temperature was measured with an accuracy of 0.03 K. The thickness of NLC layer ranged from 60 to 100 μm. As soon as the thermodynamic equilibrium had been established in the system, the sample was heated to 50°C. The glycerol molecules are able to diffuse into the liquid crystal, with the diffusion efficiency increasing with temperature. To initiate diffusion, the cuvette was allowed to stand at the indicated temperature for ~10 min, after which the heater was switched off. As the temperature decreased, the glycerol droplets intensively condensed and grew, because the amount of glycerol capable of dissolving in the mesophase decreases with decreasing temperature. This very simple procedure gave a homogeneous suspension of glycerol droplets in the NLC. In [13], this process is described in more detail. In the stationary state, the droplet ordering became detectable within 4–6 h after the beginning of cooling. The resulting hexagonal lattice formed by the droplets is shown in Fig. 1a.

Let us now dwell on the director distribution in the nematic layer in more detail. At the boundary with air, the liquid crystal molecules are oriented homeotropically, while at the boundary with glycerol their orientation is planar [14–17]. Therefore, the orientation in the nematic layer is hybrid. However, this is true only for the polar cohesion. The azimuthal cohesion is degenerate at both surfaces, because air and glycerol are both isotropic. The degenerate azimuthal cohesion has no crucial effect on the NLC homeotropic orientation at the upper boundary. At the lower boundary (NLC–glycerol interface), the azimuthal degeneracy of boundary conditions gives rise to spatial director variations in the sample plane and, as a result, to the inhomogeneous global orientation in the sample (this can easily be observed in the experiment [14]). Thus, the stationary orientation of the nematic layer is determined both by the surface state and elastic distortions inside the layer and by the distribution of glycerol droplets in the layer.
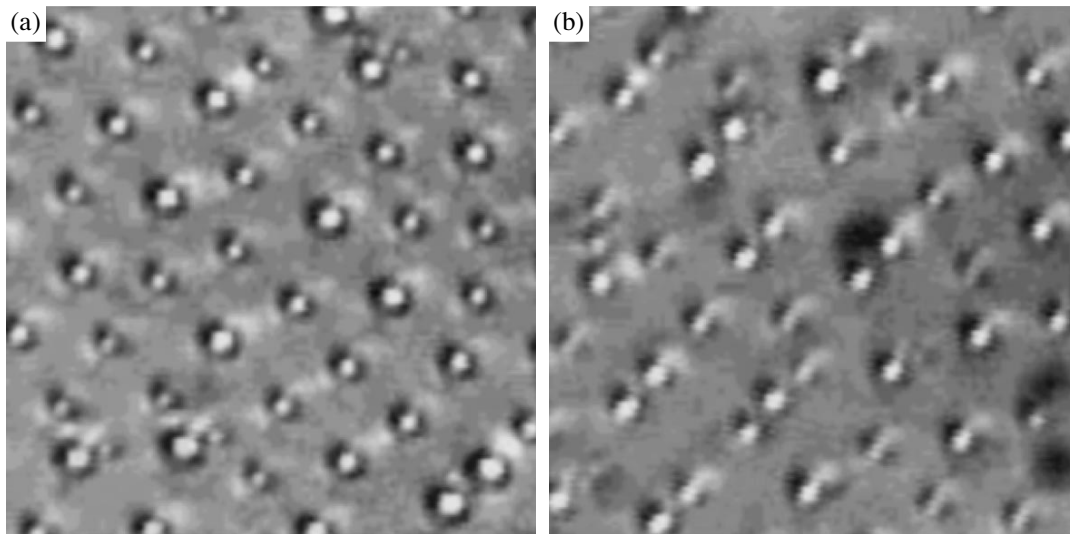
Fig. 1. Photographs of the structures formed by glycerol droplets suspended in a nematic liquid crystal: (a) without field and (b) in an external magnetic field ($H = 2$ kG).

Moreover, the hybrid orientation of the nematic layer governs the droplet distribution. The droplets, in turn, introduce additional distortions in the director distribution and, thus, change this orientation and their own distribution. It is precisely this mutual interaction that can explain the long times of establishing the crystal structure for a system of droplets in a nematic layer.

The external magnetic field alters the director distribution in the NLC layer, thereby changing the ordering of glycerol droplets. First, the azimuthal degeneracy of director orientation is removed. As a result, the influence of the distortions produced by the droplets is suppressed by the orienting effect of the magnetic field. Second, the NLC molecules themselves are partially reoriented along the magnetic field to establish a new equilibrium director distribution with the preferred orientation along the magnetic field. Thus, the effect of a magnetic field amounts to changing the global director orientation and, eventually, to changing the effective interaction between the droplets. Figure 1b shows the new droplet distribution obtained after applying a magnetic field to the hexagonally ordered structure. It should be noted that the droplets tend to form linear chains aligned with the magnetic field, with a fixed spacing both between the chains and between the droplets in the chain. The droplet size in this experiment was 7 μm, and the thickness of the liquid-crystal layer was 60 μm.

The behavior of macroinclusions in a mesophase placed in an external magnetic field is a rather complicated theoretical problem. This is primarily due to the fact that a macroinclusion generates large-scale deformations around it, causing its effective interaction with another analogous inclusion. The inhomogeneous director distribution around the inclusion is also modified upon applying the external magnetic field, resulting in a change of the effective interaction. The effective interaction itself depends on the equilibrium director distribution in the liquid crystal and changes with changing director orientation [18–20]. This problem was solved in [20], where the magnetic-field dependence of effective interaction was determined for the cylindrical inclusions. However, if the magnetic field strength is sufficient for changing the global equilibrium director distribution, the effective interaction will be determined only by the orientations and arrangement of macroinclusions relative to the new director distribution.

Although this problem has not been solved analytically as yet, one can qualitatively form a reasonable physical picture of how a collective of glycerol droplets behaves in a hybrid cell in the presence of an external magnetic field. It is known [21, 22] that the global director orientation in a hybrid cell shows nonthreshold behavior in the magnetic field and changes continuously (in some cases nonmonotonically) with changing the field. Considering that the magnetic correlation length is $\xi = \sqrt{K/\Delta\chi}/H$, one has $\xi \approx 1.5$ μm for the experimental $K \sim 10^{-11}H$, $\Delta\chi \sim 10^{-7}$, and $H \sim 1.6 \times 10^6$ Oe, so that one can state that, at distances where the glycerol droplets are concentrated, the director orientation changes appreciably in the magnetic field. This induces a change in the orientation of the spindle-shaped director distribution around an individual droplet and causes the new equilibrium boojum positions at its surface. Since, generally, all symmetry elements of director distribution around the droplet are broken, the

effective pair interaction involves all terms of the multipolar expansion [23, 24]

$$W(\rho) = -\frac{Q^2}{\rho} \pm \frac{\beta^2}{\rho^5}(3(\mathbf{n}\cdot\boldsymbol{\rho})^2 - \rho^2)$$

$$+ \frac{\gamma^2}{\rho^9}(8(\mathbf{n}\cdot\boldsymbol{\rho})^4 24(\mathbf{n}\cdot\boldsymbol{\rho})^2(\mathbf{n}\times\boldsymbol{\rho})^2 + 3(\mathbf{n}\times\boldsymbol{\rho})^4),$$
(1)

describing the dependence on the mutual orientation of the director and the vector $\boldsymbol{\rho} = \mathbf{r} - \mathbf{r}'$ between the macroinclusions. The first term corresponds to the Coulomb-type attraction with charge $Q \sim \sin 2\psi$, where ψ is the angle of mutual deviation of boojums from the global director orientation. This term appears only if all symmetry elements in the director distribution around the inclusion are broken. The next terms in the general Eq. (1) correspond to the well-known [8, 18] dipole–dipole and quadrupolar interactions caused by changing the overall director distribution. In [18, 23], the explicit expressions are presented for all coefficients as functions of the geometric characteristics of the macroinclusion shape and the director cohesive energy. For the spindle-shaped region of director deformation around the macroinclusion [13, 18], the dipolar interaction can be attractive in the plane perpendicular to the director. In the absence of an external magnetic field and in the $Q = 0$ approximation, one arrives at a result similar to that used for explaining the formation of the hexagonal crystal structure in a system of glycerol droplets introduced into an NLC with hybrid boundary conditions [13]. As we have already established, the external magnetic field alters the equilibrium orientation of the director and forces it to align with the field and, thereby, assists in the appearance of the Coulomb-type attraction [23, 25] and changes the magnitude of both quadrupolar and dipolar interactions. In the presence of a magnetic field, the influence of $(\mathbf{n}\cdot\boldsymbol{\rho})$ along the field is enhanced and the anisotropy of the dipolar and quadrupolar interactions comes into play [24]. Denoting $(\mathbf{n}\cdot\boldsymbol{\rho}) \equiv \alpha = \cos\theta$, where θ is the angle between the director and the applied field, one can represent the approximate effective pair interaction in the field direction as

$$W(\rho) = -\frac{Q^2}{\rho} \pm \frac{\beta^2}{\rho^3}(3\alpha^2 - 1) + \frac{\gamma^2}{\rho^5}(3 - 30\alpha^2 + 35\alpha^4). \quad (2)$$

This expression has a minimum at

$$\rho_c^2 = -\frac{3\beta^2(3\alpha^2 - 1)}{2Q^2}$$

$$\times\left(1 \pm \sqrt{1 + \frac{5}{9}\frac{4\gamma^2 Q^2}{\beta^4}\frac{(3 - 30\alpha^2 + 35\alpha^4)}{(1 - 3\alpha^2)}}\right). \quad (3)$$

For $\gamma^2 Q^2/\beta^4 \ll 1$, this gives the previous result

$$\rho_c^2 \approx \frac{5}{3}\frac{\gamma^2}{\beta^2}\frac{3 - 30\alpha^2 + 35\alpha^4}{(1 - 3\alpha^2)}. \quad (4)$$

If $\alpha \sim H^2$, then the new equilibrium value in the field direction decreases following the law $\rho = \rho_0(1 - kH^2)$, in accordance with the experiment. It is quite possible that the Coulomb-type attraction can appear in the absence of an external field and play a decisive role in the formation of the hexagonal structure. However, we have no direct experimental evidence of this. Physically, the behavior of the structure in a magnetic field can be imagined as follows. The initial two-dimensional structure is formed by the attractive and repulsive forces acting via the deformed elastic field of the director. The lattice elastic moduli change anisotropically in the magnetic field. This picture fits in well with the explanation given in [26] for the mutual transformations of two-dimensional structures; the only difference is in the nature of the internal interaction in the system.

REFERENCES

1. P. Poulin, H. Stark, T. C. Lubensky, and D. A. Weitz, Science **275**, 1770 (1997).

2. P. Poulin and D. A. Weitz, Phys. Rev. E **57**, 626 (1998).

3. P. Poulin, V. Cabuil, and D. A. Weitz, Phys. Rev. Lett. **79**, 4862 (1997).

4. S. P. Meeker, W. C. K. Poon, J. Crain, and E. M. Terentjev, Phys. Rev. E **61**, R6083 (2000).

5. O. D. Lavrentovich, Liq. Cryst. **24**, 117 (1998).

6. M. V. Kurik and O. D. Lavrentovich, Usp. Fiz. Nauk **154**, 381 (1988) [Sov. Phys. Usp. **31**, 196 (1988)].

7. R. W. Ruhwandl and E. M. Terentjev, Phys. Rev. E **56**, 5561 (1997).

8. T. C. Lubensky, D. Pettey, N. Currier, and H. Stark, Phys. Rev. E **57**, 610 (1998).

9. E. M. Terentjev, Phys. Rev. E **51**, 1330 (1995).

10. H. Stark, Eur. Phys. J. B **10**, 311 (1999).

11. R. W. Ruhwandl and E. M. Terentjev, Phys. Rev. E **55**, 2958 (1997).

12. Y. Ch. Loudet, P. Barois, and P. Poulin, Nature **407**, 611 (2000).

13. V. G. Nazarenko, A. B. Nych, and B. I. Lev, Phys. Rev. Lett. **87**, 075504 (2001).

14. S. Faetti and L. Fronzoni, Solid State Commun. **25**, 1087 (1978).

15. P. Chiarelli, S. Faetti, and L. Fronzoni, Phys. Lett. A **101**, 31 (1984).

16. O. D. Lavrentovich and V. M. Pergamenshchik, Int. J. Mod. Phys. **9**, 2389 (1995).

17. O. D. Lavrentovich, Phys. Scr. **39**, 394 (1991).

18. B. I. Lev and P. M. Tomchuk, Phys. Rev. E **59**, 591 (1999).

19. J. Fukuda and H. Yokoyama, Eur. Phys. J. E **4**, 389 (2001).

20. S. L. Lopatnikov and V. A. Namiot, Zh. Éksp. Teor. Fiz. **75**, 361 (1978) [Sov. Phys. JETP **48**, 180 (1978)].

21. D. Sabacius, V. M. Pergamenshchik, and O. D. Lavrentovich, Mol. Cryst. Liq. Cryst. **288**, 129 (1996).

22. P. Ziherl, D. Sabacius, A. Strigazzi, *et al.*, Liq. Cryst. **24**, 607 (1998).

23. B. I. Lev, S. B. Chernyshuk, P. M. Tomchuk, and H. Yokoyama, Phys. Rev. E **65**, 021709 (2002).

24. J. Fukuda, B. I. Lev, K. M. Aoki, and H. Yokoyama, submitted to Phys. Rev. E.

25. S. B. Chernyshuk, B. I. Lev, and H. Yokoyama, Zh. Éksp. Teor. Fiz. **120**, 871 (2001) [JETP **93**, 760 (2001)].

26. L. Radzilovsky, E. Frey, and D. R. Nelson, Phys. Rev. E **63**, 031503 (2001).

Translated by V. Sakun

Subgap Anomaly and Above-Energy-Gap Structure in Chains of Diffusive SNS Junctions[1]

T. I. Baturina[1], *, D. R. Islamov[1, 2], and Z. D. Kvon[1]

[1] *Institute of Semiconductor Physics, Novosibirsk, 630090 Russia*
e-mail: tatbat@isp.nsc.ru
[2] *Novosibirsk State University, Novosibirsk, 630090 Russia*
Received February 26, 2002

We present the results of low-temperature transport measurements on chains of superconductor–normal constriction–superconductor (SNS) junctions fabricated on the basis of superconducting PtSi film. A comparative study of the properties of the chains, consisting of 3 and 20 SNS junctions in series, and single SNS junctions reveals essential distinctions in the behavior of the current–voltage characteristics of the systems: (i) a gradual decrease of the effective suppression voltage for the excess conductivity observed at zero bias as the quantity of the SNS junctions increases; (ii) a rich fine structure on the dependences dV/dI–V at dc bias voltages higher than the superconducting gap and corresponding to some multiples of $2\Delta/e$. A model explaining this above-energy-gap structure based on the energy relaxation of electrons via Cooper-pair-breaking in the superconducting island connecting normal metal electrodes is proposed. © *2002 MAIK "Nauka/Interperiodica".*

PACS numbers: 73.23.-b; 74.80.Fp; 74.50.+r

In the past few years, the mesoscopic systems consisting of a normal metal (N) or heavily doped semiconductor in contact with a superconductor (S) have attracted increased interest mainly because of the richness of the involved quantum effects [1]. The key mechanism governing the carrier transport through the NS contact is the Andreev reflection [2]. In this process, an electronlike excitation with an energy ϵ smaller than the superconducting gap Δ moving from the normal metal to the NS interface is retro-reflected as a holelike excitation, while a Cooper pair is transmitted into the superconductor. This phenomenon is the basis of the proximity effect, which generally implies the influence of a superconductor on the properties of a normal metal when being in electrical contact. The consequences of an Andreev reflection on the current–voltage characteristics (CVC) of a NS junction are studied in detail in the so-called BTK theory [3], which describes the subgap current transport in terms of ballistic propagation of quasiclassical electrons through the normal metal region, accompanied by Andreev and normal reflections from the NS interface. The probability of Andreev and normal reflections are energy-dependent quantities and the relation between them depends on the barrier strength at the NS interface, which is characterized by a parameter Z ranging from 0 for a perfect metallic contact to ∞ for a low-transparency tunnel barrier. For a perfect contact ($Z = 0$), the probability of an Andreev reflection is equal to unity for particles with an energy ϵ smaller than the superconducting gap Δ, and the subgap conductance is found to be twice the normal state

conductance, thus demonstrating the double charge transfer. In the other limit, when $Z \longrightarrow \infty$, the conductivity is very small.

When a normal metal is placed between two superconducting electrodes, another mechanism is involved in charge transfer—multiple Andreev reflection process (MAR). The concept of MAR was first introduced by Klapwijk, Blonder, and Tinkham [4] in order to explain the subharmonic energy-gap structure observed as dips in the differential resistance dV/dI of SNS junctions at the voltages $V_n = 2\Delta/ne$ ($n = 1, 2, 3, ...$). In all systems, diffusive as well as ballistic, the MAR mechanism relies on the quasiparticles being able to add up energy gained from multiple passages. This energy gain results in strong quasiparticle nonequilibrium. Calculations of the CVC, within the approach developed in [3], and taking into account the MAR process was performed in [5] (OTBK theory). It was shown that the MAR process results not only in a subharmonic energy gap structure (SGS) at voltages $V_n = 2\Delta/ne$ but affects the general form of CVC at all voltages as well. Although BTK theory does not intend to describe diffusion transport in a normal metal region, a suitable value, $Z \sim 0.55$, of the barrier strength gives results very close to those obtained by the Green's function method for microconstriction in the dirty limit [6]. Experimentally, in some cases BTK theory was successful in providing a method to extract the junction reflection coefficients based on experimental CVC [7, 8].

At present, a large variety of SNS junctions (most of them are diffusive) are being fabricated and studied [7–14]. The investigations of these junctions focus prima-

---

[1] This article was submitted by the authors in English.

rily on the nonlinear behavior of the current–voltage characteristics, which exhibit an anomalous resistance dip at zero bias [zero bias anomaly (ZBA)], the SGS, etc. These experiments have revealed a number of peculiar properties of diffusive SNS junctions, the explanation of which is beyond the ballistic BTK and OTBK theories. Nowadays, the properties of diffusive SNS junctions are considered to be determined not only by the parameters of the NS interface, but nonlocal coherent effects as well, namely, (i) the superposition of multiple coherent scattering at the NS interfaces in the presence of disorder (so-called reflectionless tunneling [15]) and (ii) electron–electron interaction in the normal part. The latter is one of the important points of a recently developed "circuit theory" when applied to diffusive superconducting hybrid systems [16]. Within this approach, which is based on the use of nonequilibrium Green's functions, the electron–electron interaction induces a weak pair potential in the normal metal. It results not only in a change of the resistance, but also in a nontrivial distribution of the electrostatic and chemical potentials in the structure, which implies nonlocal resistivity. Following the spirit of Nazarov's circuit theory, Bezuglyi *et al.* [17] have developed a consistent theory of carrier transport in long diffusive SNS junctions with arbitrary transparency of NS interfaces. Although much work, both theoretical and experimental, has been done on single SNS junctions, it is a challenge to fabricate and carry out comparative measurements on multiply connected SNS systems. In this paper, we present the results of low-temperature transport measurements on chains of SNS junctions and on single SNS junctions and perform a comparative analysis of their properties.

The design of our samples is based on the fabrication technique of SNS junctions, which we recently proposed and realized for the preparation of single SNS junctions and two-dimensional arrays of SNS junctions [13, 14]. The main idea employed in those experiments was to use superconductive and normal regions made of the same material. The point is the suppression of superconductivity in the submicron constrictions made in an ultrathin polycrystalline PtSi superconducting film by means of electron beam lithography and subsequent plasma etching. Here, we use the same fabrication technique to prepare chains of SNS junctions.

The original PtSi film (thickness 6 nm) was formed on a Si substrate. The film was characterized using Hall bridges 50 μm wide and 100 μm long. The film had a critical temperature $T_c = 0.56$ K. The resistance per square was 104 Ω. The carrier density obtained from Hall measurements was 7×10^{22} cm^{-3}, which corresponds to a mean free path $l = 1.2$ nm and a diffusion constant $D = 6$ cm^2/s, estimated using the simple free-electron model.

A single SNS junction is a constriction between two holes made in the film and placed in the Hall bridge. The hole diameters are 1.7 μm and the distance
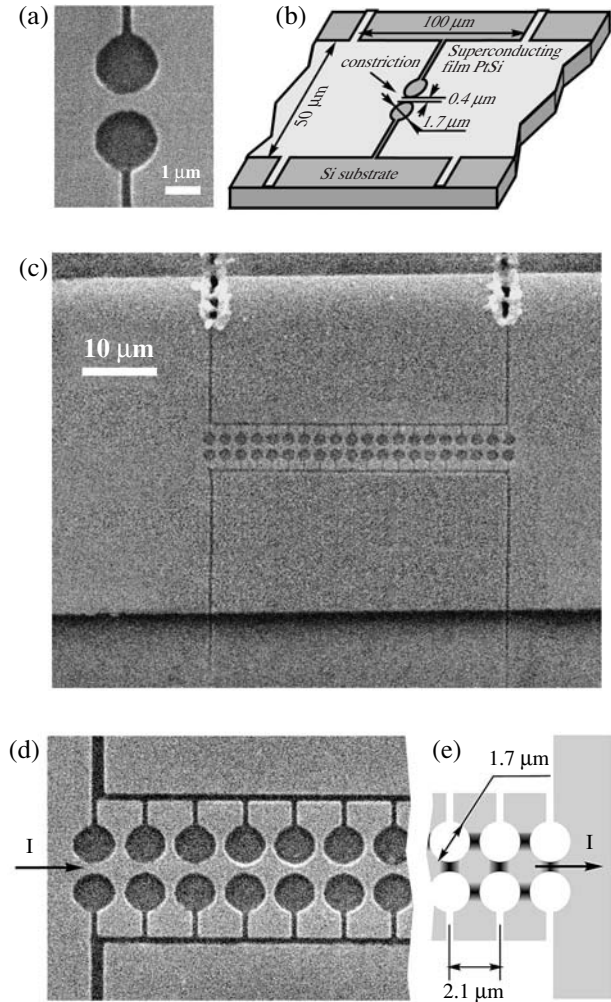

Fig. 1. (a) Scanning electron micrograph of the sample with a single constriction formed by electron-beam lithography and subsequent plasma etching of the 6-nm PtSi film grown on a Si substrate. (b) Schematic view of a junction (not to scale) showing the layout of the constriction in the Hall bridge. (c) Scanning electron micrograph of the sample with 20 constrictions. (d) SEM subimage of the sample represented in (c). (e) The layout of a chain of SNS junctions showing the dimensions of the structure. Regions of the normal metal constrictions are dark, and the superconducting islands are light gray.

between centres of holes is 2.1 μm, resulting in a width of the narrowest part of the constriction of 0.4 μm. A scanning electron micrograph and a schematic view of the sample are presented in Figs. 1a and 1b. The chains of SNS junctions are a series of constrictions connected by the islands of the film (Figs. 1c, 1d). They are designed to provide the possibility of comparative study. The dimensions of constrictions are identical with those of the single SNS junction, and the characteristic size of the islands of the film is ~1.3 μm. As the constrictions are not superconducting, we have a chain of SNS junctions (Fig. 1e).
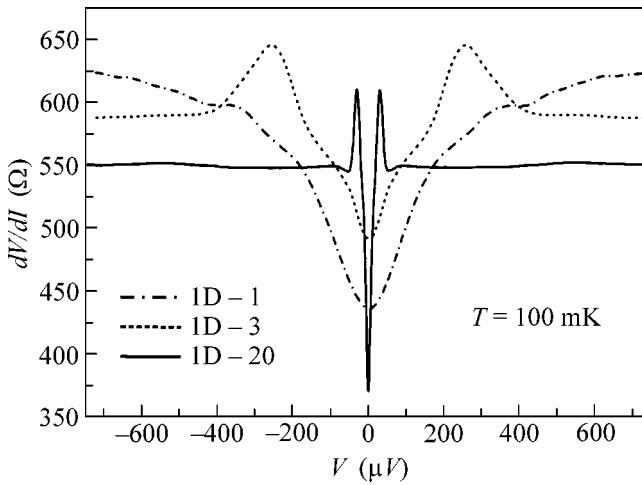
Fig. 2. Differential resistance vs. dc bias voltage for samples: (1D-1) with single constriction, (1D-3) with three constrictions in series, and (1D-20) with twenty constrictions in series. $T = 100$ mK. Differential resistance and dc bias voltage are divided by 3 and 20 for samples 1D-3 and 1D-20, respectively.

The measurements were carried out with the use of a phase-sensitive detection technique at a frequency of 10 Hz, which allowed us to measure the differential resistance (dV/dI) as a function of the dc current (I). The ac current was equal to 1–10 nA. Figure 2 shows typical dependences of dV/dI–V for the samples with single constriction (1D-1) and chains consisting of 3 (sample 1D-3) and 20 (sample 1D-20) SNS junctions in series. On the abscissa, the value of the voltage obtained by numerical integration of the experimental dependences dV/dI–I and divided afterward by the number of SNS junctions is plotted. The measured differential resistance is also divided by the number of SNS junctions (by 3 for structure 1D-3 and by 20 for structure 1D-20). Thus, for the chains, the data presented in Fig. 2 are average dependences of the differential resistance on the dc bias voltage per SNS junction. As is seen, at a high voltage for chains, the average resistances of an SNS unit of chains obtained in such a way are close to each other and to the value dV/dI of the structure with a single SNS junction. A common feature for all structures studied is a minimum of the differential resistance at zero bias voltage. It points to the
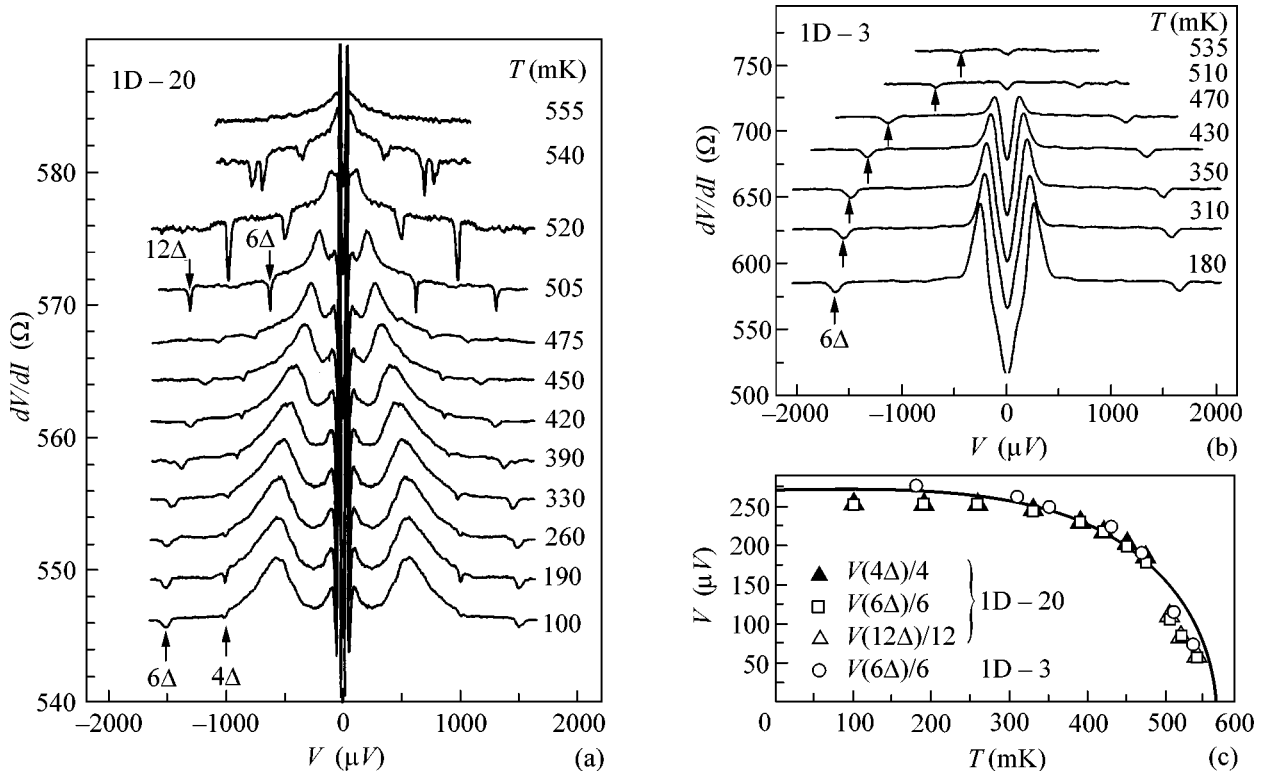

Fig. 3. (a) Temperature evolution of the differential resistance of the sample 1D-20 as a function of the average bias voltage dropping at one SNS junction. All traces except the lowest trace are shifted up for clarity. (b) The same for the sample 1D-3. The differential resistance reveals symmetrical minima at voltages exceeding 2Δ. The arrows indicate the above-energy-gap structure (AGS), corresponding to integer multiples of the 2Δ. The temperature dependence of the AGS at $eV = m \times 2\Delta$ divided by m for both samples is depicted in (c) by symbols and compared to the BCS temperature dependence of the gap (solid line).

high transparency of NS interfaces in these samples. The data for a single SNS junction (1D-1) exhibit a behavior very similar to that reported in our previous work [13]. In [17], the differential resistance of a long diffusive SNS junction with perfect NS interfaces at zero voltage was estimated by the following expression:

$$dV/dI(0) = R_N(1 - 2.64\xi_N/L), \qquad (1)$$

where $\xi_N = \sqrt{\hbar D/2\pi kT}$ is the decay length for the pair amplitude, L is the length of the normal metal region, and R_N is its resistance at $T > T_c$. Equation (1) is obtained on the condition that the inelastic length l_ϵ exceeds the junction length L. The energy relaxation is described by the time $\tau_\epsilon^{-1} = \pi\epsilon^2/(8\hbar E_F)$. This is the time it takes for a "hot" quasiparticle with energy ϵ much larger than temperature T to thermalize with all other electrons. For the excitation energy $\epsilon = 2\Delta$ ($\Delta/e \sim 270\,\mu\mathrm{V}$), we obtain $l_\epsilon = \sqrt{D\tau_\epsilon} \sim 4.6\,\mu\mathrm{m}$. The magnitude of l_ϵ significantly exceeds the characteristic length of the constriction. As R_N we take the difference between the resistance of the whole structure with constriction and the resistance of the original film without constriction measured between the same probes at $T > T_c$. This gives $R_N \sim 530\,\Omega$. Assuming $L \sim 1\,\mu\mathrm{m}$, we find from Eq. (1) at $T = 100\,\mathrm{mK}$ the differential resistance at zero bias $dV/dI(0) \sim 0.8R_N = 420\,\Omega$. As is seen in Fig. 2, this value is a close fit to the measured $dV/dI(0)$ for the sample with single constriction 1D-1. A clear-cut distinction between dependences dV/dI–V of the single SNS junction and the chains consists in the nonmonotonic behavior of dV/dI–V characteristics of the latter. The differential resistance of the chains has a minimum at zero bias voltage and shows a maximum at a finite bias voltage of about 250 μV for the sample 1D-3 and 30 μV for 1D-20. The second feature is the gradual decrease of the effective suppression voltage for the excess conductivity observed at zero bias as the quantity of the SNS junctions increases. The same behavior—nonmonotonic dV/dI–V characteristics and the decrease of the effective suppression voltage for the excess conductivity in comparison with that in single SNS junctions—was observed in two-dimensional arrays of SNS junctions [14].

The most unexpected result obtained for chains of SNS junctions is the presence of a fine and fully symmetric structure in the form of dips in the differential resistance at high biases (Fig. 3a, 3b). The positions of these dips approximately correspond to multiples of 4, 6, and 12 of the superconducting gap. As is seen in Fig. 3c, the temperature dependence of the positions of these dips actually reflects the dependence $\Delta(T)$. To our knowledge, the results presented in this paper represent the first investigation of chains of SNS junctions and the first observation of such an above-energy-gap structure (AGS). To offer an explanation of the AGS, let us
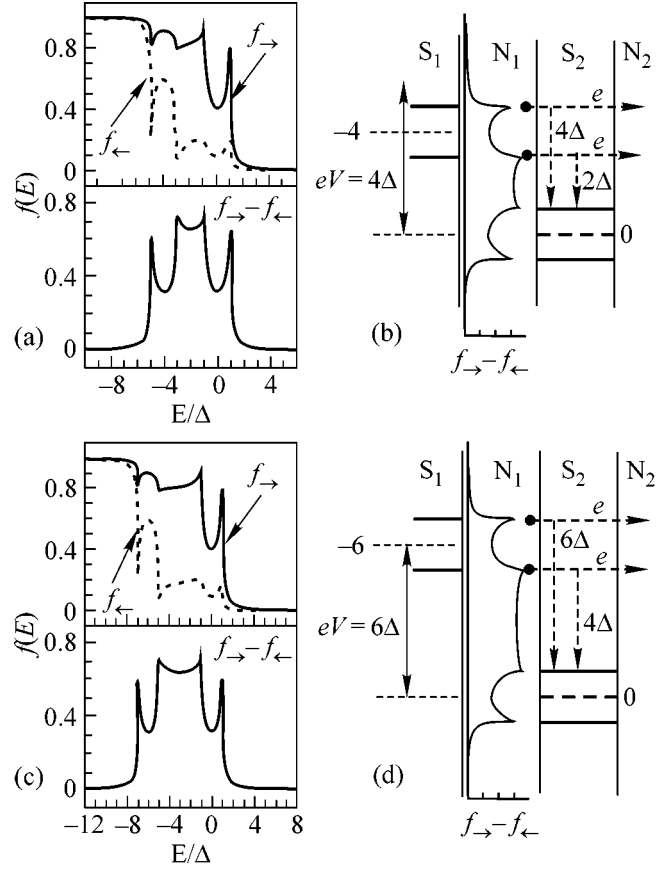
Fig. 4. Nonequilibrium distributions in normal region for SNS junction with $Z = 0.55$: (a, b) at $eV = 4\Delta$; (c, d) at $eV = 6\Delta$ and $T = 0$. In (b) and (d) the function $[f_\rightarrow(E) - f_\leftarrow(E)]$ is depicted in the region N_1. The energy scale is plotted vertically.

consider a current driven in the normal region at high voltages. As the inelastic length is larger than the normal metal region, at finite voltage, a quasiparticle passing through N_1 between two superconductors S_1 and S_2 (Figs. 4b, 4d) results in a nonequilibrium energy distribution of quasiparticles. We begin by addressing this problem using the ballistic OTBK theory [5]. In this approach, the quasiparticles are divided into two subpopulations which depend on their direction of motion $f_\rightarrow(E)$ and $f_\leftarrow(E)$, with all energies measured with respect to the local chemical potential. The current through the junction is

$$I \propto \int_{-\infty}^{+\infty} [f_\rightarrow(E) - f_\leftarrow(E)]dE. \qquad (2)$$

In Figs. 4a and 4c, we have plotted $f_\rightarrow(E)$, $f_\leftarrow(E)$, and $[f_\rightarrow(E) - f_\leftarrow(E)]$, assuming a parameter $Z = 0.55$. The voltage across the junction equals $4\Delta/e$ and $6\Delta/e$ in Fig. 4a and Fig. 4c, respectively. The function $[f_\rightarrow(E) - f_\leftarrow(E)]$ is depicted in the region N_1 in Figs. 4b and 4d, with the energy scale being plotted vertically. These

calculations clearly show that the nonequilibrium distributions are sharply peaked at the four gap edges. What happens to quasiparticles injected into the superconducting electrode S_2 and which has an energy more than 2Δ measured with respect to the gap edge of S_2? It can decay under spontaneous phonon emission into states of lower energy [18]. Phonons emitted in the process of energy relaxation of injected quasiparticles can be reabsorbed via Cooper-pair breaking. Depending on the volume of finite states, the probability of this process is a nonmonotonic function of the primary energy of injected quasiparticles. It takes the peak values at the energies multiplied by 2Δ for the density of quasiparticle states to have a singularity at the gap edge. As a result, one quasiparticle injected into S_2 with an energy higher than the gap edge by $m \times 2\Delta$ can cause up to $1 + 2m$ quasiparticles injected into N_2 (Figs. 4b, 4d) and consequently an decrease of the differential resistance. The realization of this scenario requires the length of energy relaxation to be comparable to the dimensions of the superconductor. This is actually fulfilled in the SNS systems studied. The proposed mechanism supposes a system consisting of two SNS junctions in series to be sufficient in order to observe the AGS.

In summary, we have performed the first comparative study of the properties of chains and single SNS junctions. Our experiments reveal essential distinctions in the behavior of the current–voltage characteristics of these systems. A detailed quantitative analysis needs to take into account the contributions of nonlocal coherent transport and the effect of quasiparticle injection in both the superconducting and normal regions of chains of the SNS junctions.

REFERENCES

1. B. Pannetier and H. Courtois, J. Low Temp. Phys. **118**, 599 (2000).

2. A. F. Andreev, Zh. Éksp. Teor. Fiz. **46**, 1823 (1964) [Sov. Phys. JETP **19**, 1228 (1964)].

3. G. E. Blonder, M. Tinkham, and T. M. Klapwijk, Phys. Rev. B **25**, 4515 (1982).

4. T. M. Klapwijk, G. E. Blonder, and M. Tinkham, Physica B & C (Amsterdam) **109-110**, 1657 (1982).

5. M. Octavio, M. Tinkham, G. E. Blonder, and T. M. Klapwijk, Phys. Rev. B **27**, 6739 (1983); K. Flensberg, J. Bindslev Hansen, and M. Octavio, Phys. Rev. B **38**, 8707 (1988).

6. S. N. Artemenko, A. F. Volkov, and A. V. Zaitsev, Pis'ma Zh. Éksp. Teor. Fiz. **28** (10), 637 (1978) [JETP Lett. **28**, 589 (1978)]; Solid State Commun. **30**, 771 (1979).

7. W. M. van Huffelen, T. M. Klapwijk, M. J. de Boer, and N. van der Post, Phys. Rev. B **47**, 5170 (1993).

8. J. Kutchinsky, R. Taboryski, T. Clausen, *et al.*, Phys. Rev. Lett. **78**, 931 (1997).

9. H. Courtois, Ph. Gandit, D. Mailly, and B. Pannetier, Phys. Rev. Lett. **76**, 130 (1996).

10. P. Charlat, H. Courtois, Ph. Gandit, *et al.*, Phys. Rev. Lett. **77**, 4950 (1996).

11. A. Frydman and R. C. Dynes, Phys. Rev. B **59**, 8432 (1999).

12. T. Hoss, C. Strunk, T. Nussbaumer, *et al.*, Phys. Rev. B **62**, 4079 (2000).

13. Z. D. Kvon, T. I. Baturina, R. A. Donaton, *et al.*, Phys. Rev. B **61**, 11340 (2000).

14. T. I. Baturina, Z. D. Kvon, and A. E. Plotnikov, Phys. Rev. B **63**, 180503(R) (2001).

15. B. J. van Wees, P. de Vries, P. Magnee, and T. M. Klapwijk, Phys. Rev. Lett. **69**, 510 (1992); C. W. J. Beenakker, Phys. Rev. B **46**, 12841 (1992); I. K. Marmorkos, C. W. J. Beenakker, and R. A. Jalabert, Phys. Rev. B **48**, 2811 (1993).

16. Yu. V. Nazarov and T. H. Stoof, Phys. Rev. Lett. **76**, 823 (1996); T. H. Stoof and Yu. V. Nazarov, Phys. Rev. B **53**, 14496 (1996).

17. E. V. Bezuglyi, E. N. Bratus', V. S. Shumeiko, *et al.*, Phys. Rev. B **62**, 14439 (2000).

18. W. Eisenmenger, in *Physical Acoustics*, Ed. by W. P. Mason and R. N. Thurston (Academic, New York, 1976), Vol. XII, p. 79.

Experimental Evidence for a Magnetic Two-Phase State in Manganites

R. V. Demin[1], L. I. Koroleva[1, *], R. Szymszak[2], and H. Szymszak[2]

[1]Moscow State University, Vorob'evy gory, Moscow, 119899 Russia
[2]Institute of Physics, Polish Academy of Sciences, Warsaw, 02668 Poland
*koroleva@ofef343.phys.msu.su
Received February 26, 2002

It is found that samples of manganites $La_{0.9}Sr_{0.1}MnO_3$ (single crystal), $Eu_{0.7}A_{0.3}MnO_3$ (A = Ca, Sr; ceramics), and $La_{0.1}Pr_{0.6}Ca_{0.3}MnO_3$ and $La_{0.84}Sr_{0.16}MnO_3$ (thin epitaxial films) that are either field-cooled (in a magnetic field) or zero-field-cooled differ in low-temperature magnetization, and the hysteresis loop of field-cooled samples exhibits a displacement. This displacement signifies that a ferro–antiferromagnetic state occurs in these samples. The exchange integral $J \sim 10^{-6}$ eV is calculated from this displacement, which describes the exchange Mn–O–Mn coupling through the interface ferromagnetic droplet–antiferromagnetic matrix. The magnetoresistance and volume magnetostriction of $La_{1-x}Sr_xMnO_3$ single crystals exhibit similar dependences on x, temperature, and the magnetic field in the vicinity of the Curie point, which points to the fact that these dependences are due to the same reason, namely, the occurrence of a magnetic two-phase ferro–antiferromagnetic state caused by strong s–d exchange. © *2002 MAIK "Nauka/Interperiodica"*.

PACS numbers: 72.20.My; 75.50.Pp; 75.80.+q

Interest in manganites is primarily due to colossal magnetoresistance (CMR), which has been observed in some compositions at room temperatures. This allows the use of manganites in various sensor devices. At present, various viewpoints exist concerning the physical processes that lead to CMR in manganites. The matter is that the pattern in manganites becomes more complicated as compared to conventional magnetic semiconductors (EuO, EuS, EuSe, EuTe, $CdCr_2Se_4$, and $CdCr_2S_4$), in which giant magnetoresistance is explained with the use of special magnetic impurity states, i.e., ferrons [1]. This complication in manganites is due to the presence of the Jahn–Teller effect, which favors the localization of charge carriers, and the relative softness of the crystal lattice, because of which a change of the crystal lattice type was observed in a number of compositions under the action of a magnetic field, pressure, and temperature. Therefore, different explanations of CMR in manganites have been advanced, and these are associated with the melting of charge ordering, the transition from Zener double exchange to polaron conduction, etc. These explanations were described in reviews [1–5] and in references therein. However, it should be emphasized that CMR and, especially, its peak are observed in the vicinity of the Curie point T_C and result in suppressing the resistance peak in the vicinity of T_C. These facts cannot be explained using the hypotheses mentioned above.

At present, an increasing number of researchers associate CMR in manganites with the existence of a magnetic two-phase ferro–antiferromagnetic state in these materials such that charge carriers are contained in the ferromagnetic (FM) part. It can be insulating (an FM droplet in the antiferromagnetic (AFM) matrix) and conducting at a higher level of doping (an FM conducting matrix in which insulating AFM microdomains are located). However, the cause of the magnetic two-phase state (MTPS) is interpreted differently by different researchers: as a strong s–d exchange in the works by Nagaev [1, 2], Dagotto *et al.* [3], Yanase and Kasuya [6], etc., and as a strong electron–phonon interaction in the works by Gor'kov [4], De Teresa *et al.* [7], etc. The latter interpretation is supported by the great isotopic effect found in a small number of compositions. Our studies corroborate the first point of view: we found a giant shift of ~0.4 eV in the absorption edge in the $La_{0.9}Sr_{0.1}MnO_3$ composition due to FM ordering [8]. The occurrence of a red shift in the absorption edge reflects, in this case, a shift exactly in the valence band top and indicates that the energy of mobile holes decreases with an increasing degree of FM order. At a moderately high concentration of impurities, it becomes energetically profitable to localize holes in the vicinity of impurities and thus maintain FM ordering. In addition to the gain in the energy of s–d exchange, the localization of holes near impurities is favored by the Coulomb attraction to acceptors. Yanase and Kasuya showed [6] that the lattice constant inside the FM droplets are reduced, because the new charge distribution leads to a decrease in energy in the droplets through an increase in the overlap of charge clouds
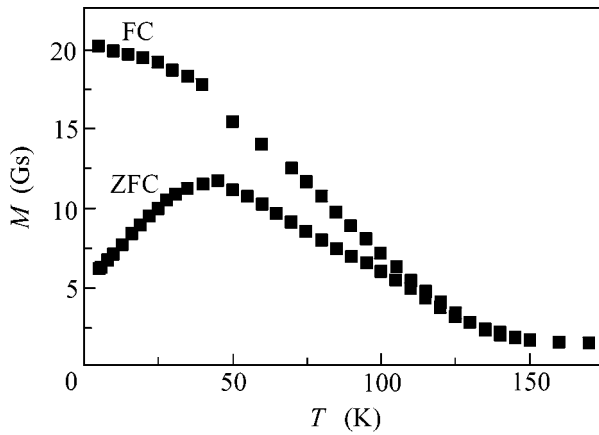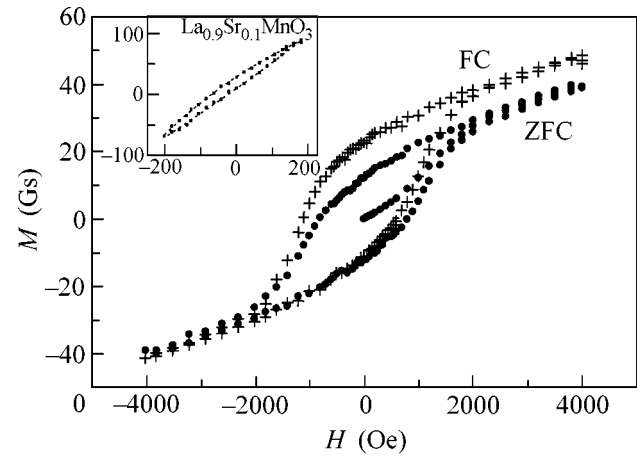
Fig. 1. (*1*) Temperature dependence of magnetization in a magnetic field of 0.6 kOe obtained under various cooling conditions for a $La_{0.1}Pr_{0.6}Ca_{0.3}MnO_3$ thin film on a (001)SrTiO₃ substrate. The ZFC curve: the film was cooled from room temperature to 5K in the absence of field; the FC curve: the film was cooled from room temperature to 5 K in a magnetic field of 0.6 kOe.

Fig. 2. Hysteresis loops for a $La_{0.1}Pr_{0.6}Ca_{0.3}MnO_3$ thin film on a (001)SrTiO₃ substrate at 5 K obtained under various cooling conditions. The ZFC curve: the film was cooled from room temperature to 5K in the absence of field; the FC curve: the film was cooled from room temperature to 5 K in a magnetic field of 4 kOe. Inset: the hysteresis loop for a $La_{0.9}Sr_{0.1}MnO_3$ single crystal at 5 K obtained after cooling from room temperature to 5K in a magnetic field of 20 kOe.

between the central impurity ion and its nearest neighbors (magnetic ions).

This paper reports experimental evidence for MTPS in the following manganite compositions: $La_{1-x}Sr_xMnO_3$ ($x = 0.1, 0.15$, and 0.3) single crystals, $Eu_{1-x}A_xMnO_3$ (A = Ca, Sr; $x = 0.3$) ceramics, and $La_{0.84}Sr_{0.16}MnO_3$ and $La_{0.1}Pr_{0.6}Ca_{0.3}MnO_3$ epitaxial thin films. Single crystals were grown by A.M. Balbashov using crucibleless floating-zone melting, and the ceramics were obtained by Ya.M. Mukovskiĭ using conventional ceramic technology. Epitaxial thin films were prepared by O.Yu. Gorbenko and A.R. Kaul' using the MOCVD technique. All the samples were single-phase according to x-ray diffraction data.

The magnetization and paramagnetic susceptibility of bulk samples were measured using a vibrating-coil magnetometer and a Weiss balance with electromagnetic compensation, respectively. The magnetization of thin films was obtained using a SQUID magnetometer. The electric resistance of all samples was measured by the four-point probe method. Magnetostriction and thermal expansion were measured using strain gauges.

For a $La_{0.9}Sr_{0.1}MnO_3$ single crystal, $Eu_{0.7}A_{0.3}MnO_3$ (A = Ca, Sr), and $La_{0.1}Pr_{0.6}Ca_3MnO_3$ and $La_{0.84}Sr_{0.16}MnO_3$ thin films, we observed a difference between the magnetizations *M* of a field-cooled sample cooled in a field *H* ((FC) sample) and without a field (zero-field-cooled (ZFC) sample) and a displacement of the low-temperature hysteresis loop of the FC sample with respect to the *H* axis, which is shown in Figs. 1 and 2. It was also found that the remanent magnetization of a FC sample is higher than the remanent magnetization of a ZFC sample. A similar displacement

of the hysteresis loop was observed in [9] in partially oxidized cobalt and was associated with exchange interaction between FM Co particles and AFM shells of CoO coating these particles. This phenomenon was given the name "exchange anisotropy."

The displaced hysteresis loops observed in this work unambiguously point to the existence of a ferro–antiferromagnetic magnetic two-phase state in the $La_{1-x}Sr_xMnO_3$ system with exchange interaction between the FM and AFM parts of the crystal. The exchange anisotropy constant K_u was calculated for all the samples listed above from the displacement of the hysteresis loop

$$\Delta H = \frac{K_u}{M_s}, \qquad (1)$$

where K_u is the exchange anisotropy constant and M_s is the saturation magnetization. It was found that the exchange anisotropy constant is on the order 10^4 erg/cm³. The exchange integral *J* describing one Mn–O–Mn bond through the FM droplet–AFM matrix interface can be calculated from the K_u value if the concentration of FM droplets and their surface area are known. Unfortunately, these data are unavailable at present. Nevertheless, the value of *J* can be estimated if some simplifying assumptions are made as follows: the compositions under study have the ideal cubic perovskite structure, whose unit cell contains one formula unit with lattice constants $a = b = c = 3.88$ Å (Fig. 3); a FM droplet consists of eight unit cells with one impurity Sr(Ca) ion at the center (see Fig. 3); to ensure that the FM droplets do not overlap, their total volume should not exceed 25% of the sample volume under the condi-

tion that the droplets are uniformly distributed in the sample. Then, 1 cm³ of a sample contains 8×10^{21} FM droplets, and an exchange coupling energy of ~10^{-5} eV corresponds to one droplet. Eight manganese ions in a FM droplet have 24 exchange bonds through oxygen ions with manganese ions of the AFM matrix. However, it should be taken into account that the AFM part of a sample has a layered AFM structure and, therefore, only half of the bonds are reoriented at the FM droplet–AFM matrix interface. Therefore, $|J| \sim 10^{-6}$ eV is two orders of magnitude smaller than the value of the negative exchange integral between the FM layers in LaMnO₃ $|J_2| = 5.8 \times 10^{-4}$ eV obtained from neutron scattering experiments [10]. This means that the occurrence of a layer with oblique spins at the interface mentioned above is highly improbable.

The temperature dependence of the resistivity $\rho(T)$ for the compositions listed above, except La₀.₇Sr₀.₃MnO₃, is of the semiconductor type with a maximum in the $\rho(T)$ curve and CMR in the vicinity of T_C (our measurements and the data from [11–13]). It is evident that these compositions represent AFM LaMnO₃, La₀.₁₅Pr₀.₈₅MnO₃, and EuMnO₃ semiconductors doped with Sr^{2+} or Ca^{2+} ions. It may be suggested that an insulating MTPS occurs in these materials: FM droplets surrounding acceptor ions are arranged in the insulating AFM matrix. CMR in this case is explained by an increase in the radii of FM droplets in the magnetic field, which facilitates hole tunneling among FM droplets. In addition, the magnetic moments of FM droplets are ordered by the external field, which also facilitates tunneling. Finally, a magnetic field tends to destroy FM droplets, increasing the energy of holes inside the droplets and thus promoting their transition to a delocalized state [2]. It is evident in Fig. 1 that the $M(T)$ curves for a ZFC sample exhibit a maximum at $T = T_f$, whereas such a maximum is not observed for a FC sample. As was indicated above, the remanent magnetization of a FC sample is higher than that for a ZFC sample. The magnetic properties listed above are similar to the magnetic properties of cluster spin glasses. Nevertheless, there are also significant distinctions. Thus, the value of M in the case of spin glasses is independent of T at $T < T_f$. In the case under consideration, the magnetization of a FC sample increases with decreasing temperature and at 4.2 K exceeds the value of M for a ZFC sample by approximately an order of magnitude. This fact can be explained by an increase in the volume of the FM phase of the MTPS sample with decreasing temperature.

Additional evidence for MTPS in manganites is in the fact that the paramagnetic Curie point θ increases with the doping level. It is known that θ is determined by the sum of exchange interactions in the crystal. The contribution of FM exchange from the FM droplets to the total exchange in the crystal increases θ. Thus, the Neel and paramagnetic Curie points T_N and θ in
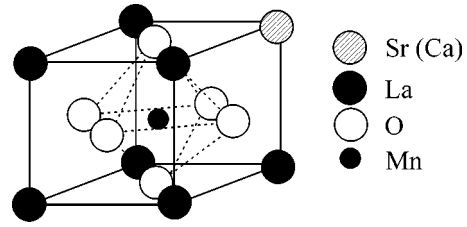

Fig. 3. Ideal cubic ABO₃ perovskite structure.

Eu₁₋ₓAₓMnO₃ are equal, respectively, to 41 and −100 K for the composition with $x = 0$; 52 and 110 K for the composition with $x = 0.3$, A = Ca; and 65.5 and 175 K the composition with $x = 0.3$, A = Sr. Thus, as x varies from 0 to 0.3, θ increases approximately three times, whereas T_N varies only slightly. In a crystal that occurs in a conducting MTPS, T_C is the Curie point of the singly connected FM part of the crystal. At the same time, the contribution of AFM exchange from AFM microdomains to the total exchange of the crystal decreases θ; therefore, T_C must exceed the paramagnetic Curie point. Thus, we obtained $T_C = 371$ K and $\theta = 364$ K for a conducting La₀.₇Sr₀.₃MnO₃ crystal. The relationship $T_C \leq \theta$ is commonly observed in samples with FM ordering.

In this work, new experimental data are reported for the La₁₋ₓSrₓMnO₃ system which point to the existence of a MTPS in this system caused by strong s–d exchange. It should be noted that Zhao et al. [14] did not find an isotope effect in the La₁₋ₓSrₓMnO₃ system; therefore, it is hardly probable that electron–phonon interaction is the reason for the MTPS in this system. Magnetostriction and thermal expansion $\Delta l/l$ were measured in single crystal bulk samples with $x = 0.1$, 0.15, and 0.3. In the course of measurements, a strain gauge was glued parallel to the c axis. The longitudinal ($\lambda_\parallel$) and transverse ($\lambda_\perp$) magnetostrictions were measured for a sample with $x = 0.1$ in magnetic fields $H \leq 35$ kOe, for a sample with $x = 0.15$ at $H \leq 120$ kOe by some of us in the laboratory of R. Ibarra at the Saragossa University (Spain), and for a sample with $x = 0.3$ at $H \leq 10$ kOe. Isotherms for the anisotropic magnetostriction $\lambda_t = \lambda_\parallel - \lambda_\perp$ and the bulk magnetostriction $\omega = \lambda_\parallel + 2\lambda_\perp$ were constructed from experimental $\lambda_\parallel(H)$ and $\lambda_\perp(H)$ curves. The anisotropic magnetostriction is positive for all the samples studied and smoothly decreases to zero in the vicinity of T_C, whereas the bulk magnetostriction is negative and reaches a maximum in absolute value in the vicinity of T_C (Fig. 4). On heating above T_C, $|\omega|$ decreases rapidly. It is evident in Fig. 4 that the maximum value of $|\omega|$ strongly depends on x: the smaller x, the larger $|\omega|$. The $\omega(H)$ curves are not saturated up to the highest fields of measurement (Fig. 5). Thus, it is clear in the figure that the $\omega(H)$ curves for the composition with $x = 0.15$ are not saturated up to 120 kOe, whereas magnetization isotherms are saturated for sam-
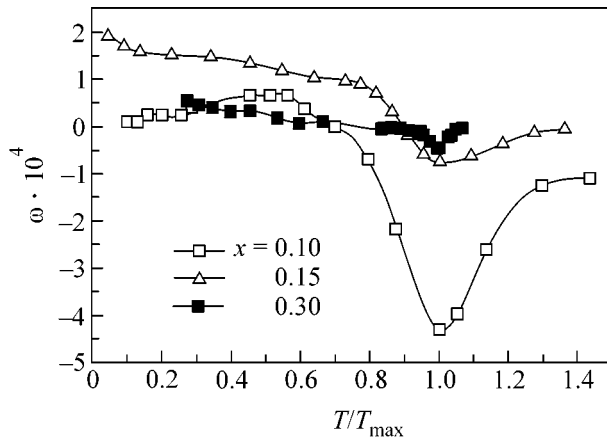
Fig. 4. Temperature dependence of the bulk magnetostriction ω normalized to the temperature of the maximum in the $\omega(T)$ curve for three single crystal samples of the $La_{1-x}Sr_xMnO_3$ system differing in composition.
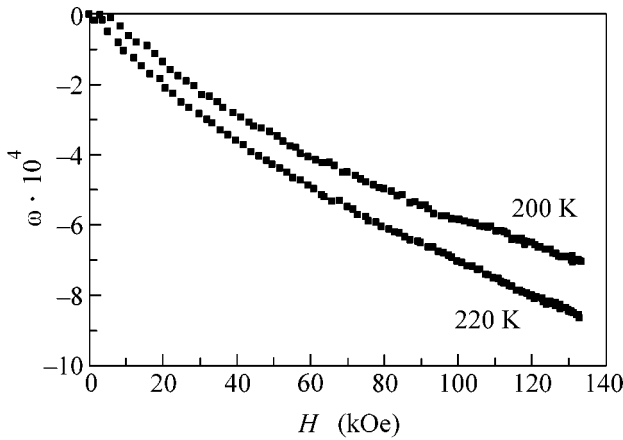
Fig. 5. Bulk magnetostriction isotherms of a $La_{0.85}Sr_{0.15}MnO_3$ single crystal in the vicinity of the Curie point.
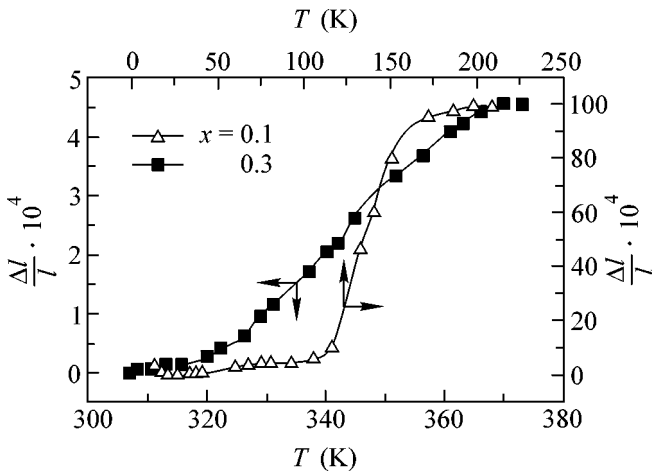
Fig. 6. Temperature dependence of the thermal expansion $\Delta l/l$ for samples of single crystal $La_{0.9}Sr_{0.1}MnO_3$ and $La_{0.7}Sr_{0.3}MnO_3$ single crystals.

ples of this system even in fields of 2–4 kOe [12, 13]. The temperature dependence of the thermal expansion of the samples under study is shown in Fig. 6. It is evident that, at $T \leq T_C$, $\Delta l/l$ significantly exceeds the thermal expansion which is linear in temperature, and which is characteristic of diamagnetic and paramagnetic systems. From a comparison of Figs. 4 and 6, it is evident that the bulk magnetostriction represents the suppression of this excessive contribution to the thermal expansion by the magnetic field.

Many aspects of the behavior of CMR and the large bulk magnetostriction are similar in the $La_{1-x}Sr_xMnO_3$ system. The temperature dependence of ρ and $\Delta\rho/\rho$ on this system was studied in [11–13]. Thus, the bulk magnetostriction in the vicinity of T_C represents the suppression of excessive thermal expansion by the magnetic field, whereas CMR resides in the suppression of the maximum in the $\rho(T)$ curve in the vicinity of T_C. The magnetoresistance and bulk magnetostriction isotherms in the vicinity of T_C are not saturated up to the highest fields of measurement, whereas saturation in the magnetization curves has long been attained. The maximum values of $|\omega|$ and $\Delta\rho/\rho$, which are attained in the vicinity of T_C, decrease with increasing x. Similar behavior of the ω and $\Delta\rho/\rho$ special features in the vicinity of T_C indicates fact that these are caused by the same reason. These features can be explained by the existence of a MTPS caused by strong s–d exchange in the indicated system. At T_C, the FM ordering is thermally destroyed only in the FM part of the magnetically two-phase sample, so here the notion of the Curie point becomes rather conventional. As was indicated above, the lattice parameters are reduced in the FM droplets [6]. That is why the excessive thermal expansion (as compared to the expansion linear in T) of a sample is observed in the vicinity of T_C (Fig. 6). However, the application of an external magnetic field at $T \geq T_C$ increases the degree of FM ordering more strongly in the vicinity of impurities than that, on average, over the crystal, because the action of the field is strengthened by s–d exchange. That is, the magnetic field creates both the MTPS destroyed by heating and the compression of the lattice inherent in its FM part. This explains the sharp increase in the negative bulk magnetostriction in the vicinity of T_C. However, the process of creating a MTPS by the field indicated above takes place only within a limited temperature range slightly above T_C. Therefore, the $|\omega|(T)$ curves pass through a maximum and rapidly decrease as the temperature further increases. It is shown in [1, 2] that a maximum of ρ in a material that occurs in an insulating MTPS is reached at temperatures at which the FM droplets dissociate on heating. This commonly occurs at $T \geq T_N$. An explanation of CMR for this case was given above. In manganites with metallic-type conduction, that is, occurring in a conducting MTPS, impurity-magnetic interaction can affect the resistance by two mechanisms: the scattering of charge carriers, which decrease their mobility, and

the formation of band tail consisting of localized states. In the vicinity of T_C, the mobility of charge carriers sharply decrease and they become partially localized in the band tail. CMR is explained by the increase in the mobility of charge carriers and an increase in their number due to the delocalization of electrons from the band tail indicated above under the action of the magnetic field. The increase in the radii of FM droplets in a magnetic field apparently takes place up to very high fields; that is why saturation is absent in the ω and $\Delta\rho/\rho$ isotherms. It is known that giant magnetoresistance in magnetic semiconductors is caused mainly by the change in the concentration of charge carriers under the action of a magnetic field [1, 2]. The concentration of charge carriers in a crystal occurring in a conducting MTPS increases with increasing magnetic field significantly more slowly than in a crystal occurring in an insulating MTPS; therefore, the magnitude of magnetoresistance in the first case is smaller than in the second. It is seen in Figs. 4 and 6 that the value of |ω| at the minimum in the |ω|(T) curve and the excessive contribution to the thermal expansion in the vicinity of T_C for the conducting composition with $x = 0.3$ are approximately an order of magnitude smaller than for the composition with $x = 0.1$, for which these values reach a maximum. It is likely that the conclusion made in [6] about the compression of the lattice inside the FM droplets is also applicable to the singly connected FM part of the crystal with $x = 0.3$, though this compression is smaller in this case.

REFERENCES

1. É. A. Nagaev, *Physics of Magnetic Semiconductors* (Nauka, Moscow, 1979); Usp. Fiz. Nauk **166**, 833 (1996) [Phys. Usp. **39**, 781 (1996)].
2. E. L. Nagaev, Phys. Rep. **346**, 381 (2001).
3. E. Dagotto, T. Hotta, and A. Moreo, Phys. Rep. **344**, 1 (2001).
4. L. P. Gor'kov, Usp. Fiz. Nauk **168**, 665 (1998) [Phys. Usp. **41**, 589 (1998)].
5. J. M. D. Coey, M. Viret, and S. von Molnar, Adv. Phys. **48**, 167 (1999).
6. A. Yanase and T. Kasuya, J. Phys. Soc. Jpn. **25**, 1025 (1968).
7. J. M. De Teresa, M. R. Ibarra, P. A. Algarabel, *et al.*, Nature **386**, 256 (1997).
8. R. V. Demin, L. I. Koroleva, and A. M. Balbashov, Pis'ma Zh. Éksp. Teor. Fiz. **70**, 303 (1999) [JETP Lett. **70**, 314 (1999)].
9. W. H. Meiklejohn and C. P. Bean, Phys. Rev. **105**, 904 (1957).
10. F. Moussa, M. Hennion, J. Rodriguez-Carvajal, *et al.*, Phys. Rev. B **54**, 15149 (1996).
11. A. Urushibara, Y. Moritomo, T. Arima, *et al.*, Phys. Rev. B **51**, 14103 (1995).
12. H. Y. Hwang, S. W. Cheong, N. P. Ong, and B. Battlogg, Phys. Rev. Lett. **77**, 2041 (1996).
13. Y. Tokura, A. Urushibara, Y. Moritomo, *et al.*, J. Phys. Soc. Jpn. **63**, 3931 (1994).
14. G. M. Zhao, K. Conder, H. Keller, and K. A. Müller, Nature **381**, 676 (1996).

Translated by A. Bagatur'yants

Density of States in a Mesoscopic SNS Junction[1]

P. M. Ostrovsky*, M. A. Skvortsov, and M. V. Feigel'man

Landau Institute for Theoretical Physics, Russian Academy of Sciences, Moscow, 117940 Russia
*e-mail: ostrov@itp.ac.ru
Received February 28, 2002

The semiclassical theory of proximity effects predicts a gap $E_g \sim \hbar D/L^2$ in the excitation spectrum of a long diffusive superconductor/normal-metal/superconductor (SNS) junction. Mesoscopic fluctuations lead to anomalously localized states in the normal part of the junction. As a result, a nonzero, yet exponentially small, density of states (DOS) appears at energies below E_g. In the framework of the supermatrix nonlinear σ model, these prelocalized states are due to the instanton configurations with broken supersymmetry. The exact result for the DOS near the semiclassical threshold is found, provided the dimensionless conductance of the normal part G_N is large. The case of poorly transparent interfaces between the normal and superconductive regions is also considered. In this limit, the total number of subgap states may be large. © 2002 MAIK "Nauka/Interperiodica".

PACS numbers: 73.21.-b; 74.50.+r; 74.80.Fp

1. Introduction. It has recently been shown within several different although related contexts that the excitation energy spectrum of superconducting–normal (SN) chaotic hybrid structures [1, 2] and superconductors with magnetic impurities [3, 4] does not possess a *hard gap*, as predicted by a number of papers [5–8] using the semiclassical theory of superconductivity [9–11]. With mesoscopic fluctuations taken into account, the phenomenon of a *soft gap* appears: the density of states is nonzero at all energies, but it decreases exponentially rapidly below the semiclassical threshold $E_g \sim \hbar/\tau_c$, with τ_c being the characteristic dwell time in the N region. In particular, for diffusive systems perfectly connected to a superconductor, E_g has the order of the Thouless energy $E_{\rm Th}$ in the N region [5, 6].

The first result in this direction was obtained in [1], where the subgap density of states (DOS) in a quantum dot was studied by employing the universality hypothesis and predictions [12] of the random-matrix theory (RMT) [13]. Later on, the tail states in a superconductor with magnetic impurities were analyzed in [3, 4] on the basis of the supersymmetric nonlinear σ-model method [14] extended to include superconducting paring [15].

A fully microscopic approach to the problem of the subgap states in diffusive normal-metal/superconductor (NS) systems was developed in [2] in the framework of the supersymmetric σ model similar to that employed in [3, 4]. Physically, the low-lying excitations in SN structures are due to anomalously localized eigenstates [16] in the N region. From the mathematical side, nonzero DOS at $E < E_g$ comes about when nontrivial field configurations—instantons—are taken into account in the σ-model functional integral. As shown in [2], at $E \approx E_g$ there are two different types of instantons, their

actions being different by a factor of 2. The main contribution to the exponentially small subgap DOS is determined by the Gaussian integral near the least-action instanton.

For a planar (quasi-1D) superconductor/normal-metal/superconductor (SNS) junction with ideally transparent SN interfaces, the DOS is given by (provided $G_N^{-2/3} \ll \varepsilon \ll 1$)

$$\langle \rho \rangle = 0.97 \delta^{-1} G_N^{-1/2} \varepsilon^{-1/4} \exp[-1.93 G_N \varepsilon^{3/2}], \quad (1)$$

where $\varepsilon = (E_g - E)/E_g$, $G_N = 4\pi\nu D L_y L_z/L_x \gg 1$ is the dimensionless conductance (in units of $e^2/2\pi\hbar$) of the normal part connecting two superconductors, $E_g = 3.12 E_{\rm Th}$, $E_{\rm Th} = D/L_x^2$ is the Thouless energy, and $\delta = (\nu V)^{-1}$ is mean level spacing. Here, L_x is the thickness of the N region, which is assumed to be larger than the superconducting coherence length. It is also assumed that the lateral dimensions L_y, L_z are not much larger than L_x (otherwise, the instanton solution acquires additional dimension(s), and the exponent 3/2 changes; cf. [2] for detail). The corresponding mean-field (MF) expression above the gap is [6]

$$\langle \rho \rangle_{\rm MF} = 3.72 \delta^{-1} \sqrt{|\varepsilon|}. \quad (2)$$

Generally, the functional form of Eqs. (1), (2) is retained, whereas the coefficients are geometry-dependent and can be found from the solution of the standard Usadel equation [11] for a specific sample geometry. In any case, the total number of states with energies below E_g is on the order of unity.

In this letter, we extend our previous results [2] in two different directions. First, we derive *exact* expression for the DOS in the energy region $|\varepsilon| \ll 1$ without

---

[1] This article was submitted by the authors in English.

the further use of the inequality $\varepsilon \gg G_N^{-2/3}$. The obtained result interpolates smoothly between the semiclassical square-root edge (2) and the exponential tail (1). Second, we consider the same SNS system allowing for nonideal transparencies at the SN interfaces. The result depends upon the relation between the dimensionless interface conductance G_T and normal conductance G_N. As long as $G_T \geq G_N^{1/4}$, all qualitative features of the previous solution are retained but the value of the semiclassical threshold E_g and numerical coefficients in expressions like Eq. (1) become dependent upon the value of $t \equiv G_T/G_N$. However, on further decrease of interface transparency, $G_T \ll G_N^{1/4}$, the DOS behavior changes dramatically: in the semiclassical region $E > E_g$ it acquires the inverse-square-root singularity, $\langle \rho \rangle_{MF} \sim (-\varepsilon)^{-1/2}$. At smallest $|\varepsilon|$, this singularity smoothens out and crosses over to an exponentially decaying tail of low-energy states. A distinctive feature of this tail, as opposed to the situations discussed previously, is that the total number of subgap states becomes large and grows as $G_T^{-1/2} G_N^{1/8} \gg 1$. We coined this situation as "strong tail" and found exponential asymptotic behavior of the DOS in the strong-tail region.

2. Outline of the method. We treat the problem within the supersymmetric formalism. The derivation of the σ-model functional-integral representation can be found in [14, 15, 17]. The DOS is given by the integral over the supermatrix Q:

$$\langle \rho(E, \mathbf{r}) \rangle = \frac{\nu}{4} \mathrm{Re} \int \mathrm{str}(k\Lambda Q(\mathbf{r})) e^{-\mathscr{S}[Q]} \mathscr{D}Q, \qquad (3)$$

$$\mathscr{S}[Q] = \frac{\pi\nu}{8} \int d\mathbf{r}\, \mathrm{str}[D(\nabla Q)^2 + 4iQ(\Lambda E + i\tau_x \Delta)]. \quad (4)$$

Q is an 8×8 matrix operating in Nambu, time-reversal (TR), and Fermi–Bose (FB) spaces. The Pauli matrices operating in the Nambu and TR spaces are denoted by τ_i and σ_i. The matrix k is the third Pauli matrix in the FB space; $\Lambda = \tau_z\sigma_z$. Integration in Eq. (3) runs over the manifold $Q^2 = 1$ with the additional constraint

$$Q = CQ^T C^T, \quad C = -\tau_x \begin{pmatrix} i\sigma_y & 0 \\ 0 & \sigma_x \end{pmatrix}_{FB}. \qquad (5)$$

This manifold is parameterized by eight commuting and eight anticommuting variables. It turns out, however, that only four commuting and four anticommuting modes are relevant in the vicinity of the quasiclassical gap, while contributions from all other modes to the DOS cancel. The detailed discussion of this fact will be published elsewhere [17]. The reduced parameteriza-

tion for the commuting part of Q in terms of the four variables reads [2]

$$Q_c^{BB} = [\sigma_z \cos k_B + \tau_z \sin k_B(\sigma_x \cos\chi_B + \sigma_y \sin\chi_B)]$$
$$\times [\tau_z \cos\theta_B + \sigma_z\tau_x \sin\theta_B], \qquad (6)$$
$$Q_c^{FF} = \tau_z\sigma_z \cos\theta_F + \tau_x \sin\theta_F.$$

The commuting part of the action (with all Grassmann variables being zero) is simplified by introducing new variables $\alpha = (\theta_B + k_B)/2$, $\beta = (\theta_B - k_B)/2$. Then, the action (4) for the normal part ($\Delta = 0$) takes the form

$$S[\theta_F, \alpha, \beta] = 2S_0[\theta_F] - S_0[\alpha] - S_0[\beta], \qquad (7)$$

$$S_0[\theta] = \frac{\pi\nu}{4} \int d\mathbf{r}[D(\nabla\theta)^2 + 4iE\cos\theta]. \qquad (8)$$

Variation of this action yields identical Usadel equations for θ_F, α, and β:

$$D\nabla^2\theta + 2iE\sin\theta = 0, \qquad (9)$$

with the condition $\theta = \pi/2$ at the NS boundaries. Equation (9) generally possesses two different solutions $\theta_{1,2} = \pi/2 + i\psi_{1,2}$, which coincide ($\psi_{1,2}(\mathbf{r}) = \psi_0(\mathbf{r})$) exactly eight at the threshold energy E_g, and are close to each other in the range we are interested in ($|\varepsilon| \ll 1$). Thus, there are possible saddle points for the action (7) corresponding to two solutions of the Usadel equation for each variable θ_F, α, β. Rotation over the angle $\chi_B \in [0, 2\pi)$ connects some of them and produces the whole degenerate family of saddle points (see [2, 17] for detail). In the following, we will need the function $f_0(\mathbf{r})$, which is the normalized difference $\psi_2(\mathbf{r}) - \psi_1(\mathbf{r})$ at $E \longrightarrow E_g$; it obeys the linear equation

$$D\nabla^2 f_0 + 2E_g \sinh\psi_0 f_0 = 0. \qquad (10)$$

3. Exact result for the transparent interface. For energies close to E_g, we substitute $\theta = \pi/2 + i\psi_0 + igf_0$ into Eq. (8), expand it in powers of g and ε, and integrate it over space using Eq. (10):

$$S_0[\theta] = S_0[\pi/2 + i\psi_0] + \tilde{G}\left[-\tilde{\varepsilon}g + \frac{g^3}{3}\right],$$
$$\tilde{G} = \frac{\pi c_2 E_g}{2\delta}, \quad \tilde{\varepsilon} = \frac{2c_1}{c_2}\varepsilon. \qquad (11)$$

Here, we have introduced the constants $c_n = \int (d\mathbf{r}/V) f_0^{2n-1} \cosh\psi_0$. For the quasi-1D geometry, $c_1 = 1.15$ and $c_2 = 0.88$. To describe the deviation of the angles α, β, and θ_F from $\pi/2 + i\psi_0$, we introduce, analogously to g, the three parameters u, v, w, respectively. Grassmann variables are introduced as $Q =$
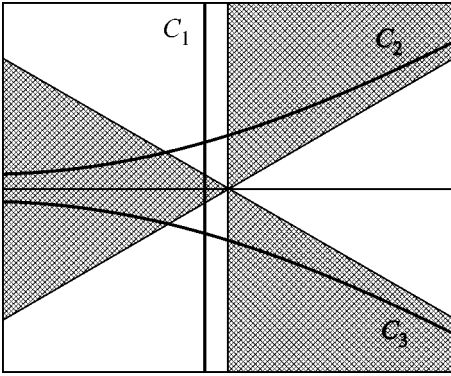
Fig. 1. Possible contours for integration over w and l. The proper choice is C_1 for w and C_3 for l.

$e^{-iW_c/2} e^{-iW_a/2} \Lambda e^{iW_a/2} e^{iW_c/2}$, where $Q_c = e^{-iW_c/2} \Lambda e^{iW_c/2}$ is specified in Eqs. (6) and

$$W_a = \begin{pmatrix} 0 & W_a^{FB} \\ i\tau_x \sigma_x (W_a^{FB})^T \sigma_y \tau_x & 0 \end{pmatrix},$$

as it must satisfy the anti-self-conjugate condition $W_a + C W_a^T C^T = 0$. Finally,

$$W_a^{FB} = \frac{f_0}{4} \begin{pmatrix} 0 & \zeta - \lambda & \zeta + \lambda & 0 \\ -\zeta + \lambda & 0 & 0 & -\zeta - \lambda \\ \xi + \eta & 0 & 0 & \xi - \eta \\ 0 & -\xi - \eta & -\xi + \eta & 0 \end{pmatrix}.$$

Expansion of the action in u, v, w and Grassmann variables leads to

$$\mathcal{S} = \tilde{G}\left[\tilde{\varepsilon}(u + v - 2w) - \frac{u^3 - v^3 - 2w^3}{3} \right.$$

$$\left. - \zeta\xi\frac{u + w}{4} - \lambda\eta\frac{v + w}{4} \right]. \tag{12}$$

For calculating the DOS, we also need an expansion of the preexponential factor in Eq. (3) as well as the Jacobian J for the parameterization of the Q matrix:

$$\frac{\nu}{4}\int d\mathbf{r}\,\mathrm{str}(k\Lambda Q) = -\frac{ic_1}{2\delta}(u + v + 2w),$$

$$J = \frac{8i\tilde{G}^2}{\pi}|u - v|.$$

By integrating over Grassmann variables and the cyclic angle χ_B, performing a rescaling $(u, v, w) \longrightarrow (2\tilde{G})^{-1/3}(u, v, w)$, which excludes $\tilde{G}$ from the integrand, and changing the variables to $l = (u + v)/2$, $m =$

$(u - v)^2/2$, we arrive at the following expression for the integral DOS:

$$\langle \rho \rangle = \frac{c_1(2\tilde{G})^{-1/3}}{4\pi\delta}\mathrm{Re}\int_0^\infty dm\int dl\,dw(w + l)$$

$$\times (w^2 + 2lw + l^2 - m)\exp\left[-\frac{w^3}{3} + \epsilon w + \frac{l^3}{3} + ml - \epsilon l\right], \tag{13}$$

where we introduced the notation $\epsilon = (2\tilde{G})^{2/3}\tilde{\varepsilon}$.

At this stage, we have to choose the contours of integration over w and l. The usual convergence requirements for the nonexpanded action (7) force the contour for w (l) to go along the imaginary (real) axis at large values of w (l). However, since the main contribution to the DOS comes from Eq. (13) determined by small w and l, these contours should be properly deformed to achieve convergence of Eq. (13). The integral (13) converges if the contour for l runs to infinity in the dark regions in Fig. 1, and otherwise for w. Therefore, we should choose the contour C_1 for w (see Fig. 1), whereas for l there are two possibilities: C_2 and C_3. The correct choice is dictated by the positivity of the DOS, which implies the contour C_3 for l. Integration in Eq. (13) is straightforward although rather cumbersome and leads to the final expression for the DOS:

$$\langle \rho \rangle = \frac{2\pi c_1}{(2\tilde{G})^{1/3}\delta}$$

$$\times \left[-\epsilon\mathrm{Ai}^2(\epsilon) + [\mathrm{Ai}'(\epsilon)]^2 + \frac{\mathrm{Ai}(\epsilon)}{2}\int_{-\infty}^{\epsilon} dy\,\mathrm{Ai}(y) \right], \tag{14}$$

where $\mathrm{Ai}(\epsilon)$ is the Airy function. Asymptotic behavior of the calculated DOS at $\epsilon \gg 1$ coincides with the result (1) of the single-instanton approximation [2]; see Fig. 2.

The functional dependence (14) coincides with the RMT prediction for the spectrum edge in the orthogonal ensemble [12]. It is not surprising, because the random-matrix theory is known to be equivalent to the 0D σ model [14]. In our case, the problem became effectively 0D after we had fixed the coordinate dependence $f_0(\mathbf{r})$ for the parameters of Q near E_g.

Breaking the time-reversal symmetry drives the system to the unitary universality class. The corresponding RMT result [12] can be obtained from Eq. (14) by dropping the last integral term. This result can easily be derived by the σ-model analysis in the following way. A strong magnetic field imposes an additional constraint on the Q matrix. As a result, the mode associated with the variable m acquires a mass; so, instead of integrating over it we set $m = 0$. One of the Grassman modes is also frozen out, giving the preexponent ($w +$

$l)^2$ in the integral (13). Finally, the expression for DOS coincides with Eq. (14) without the last term.

4. Finite transparency of the NS interface. We now turn to the analysis of the subgap structure of a quasi-1D SNS contact with finite conductance G_T of the NS boundary. The role of the interface is described by the dimensionless parameter $t = G_T/G_N$. For $t \gg 1$, the interface is transparent and the result (14) applies. In what follows, we will consider the case $t \ll 1$. The effect of finite transparency is described by the additional boundary term [14] in the action

$$\mathscr{S}_{\text{boundary}} = -\frac{G_T}{16}\text{str}(Q^L Q^R), \qquad (15)$$

where $Q^{L, R}$ are the Q matrices at both sides of the interface. Equation (15) is the first term in the expansion of the general boundary action [4, 14, 18] in the small transparency $\Gamma \ll 1$ of the conductive channel and leads to the Kupriyanov–Lukichev [19] boundary conditions. In the diffusive regime ($l \ll L_x$) at $t \ll 1$, we have $\Gamma \sim tl/L_x$, which justifies the use of Eq. (15). The commuting part of the action can still be written in the form (7) with the additional term in S_0:

$$S_0[\theta] = \frac{\pi \nu L_y L_z}{4} \int_{-L_x/2}^{L_x/2} dx[D(\theta')^2 + 4iE\cos\theta] \qquad (16)$$
$$- \frac{G_T}{4}\sin\left[\theta\left(\frac{L_x}{2}\right)\right].$$

In the limit $t \ll 1$, the Usadel equation has almost spatially homogeneous solutions, which allows the use of the expansion $\psi = A + B[1 - 4(x/L_x)^2]$ for them. Substituting this ansatz into the action (16) and minimizing over B, we obtain the action in terms of $P = e^A$:

$$S_0(P) = \frac{G_N}{8}\left[(s - t)P - \frac{2t}{P} + \frac{t^2}{24}P^2\right], \qquad (17)$$

where $s = E/E_{\text{Th}}$. Here, we keep only leading terms and substitute t for all s, except for the first one. After variation, we find the cubic saddle-point equation for P:

$$\frac{s}{t} = 1 - \frac{2}{P^2} - \frac{t}{12}P. \qquad (18)$$

The maximum of the RHS, achieved at $P_0 = (48/t)^{1/3}$, determines the position of the mean-field gap: $s_g = t + O(t^{5/3})$ and, hence, $E_g = G_T\delta/4\pi$. Depending on the deviation from the threshold, $\varepsilon = (E_g - E)/E_g = (s_g - s)/s_g$, there are two regimes for Eq. (18).

Weak tail. If $|\varepsilon| \ll t^{2/3}$, the two solutions to Eq. (18) are close to each other and can be sought in the form
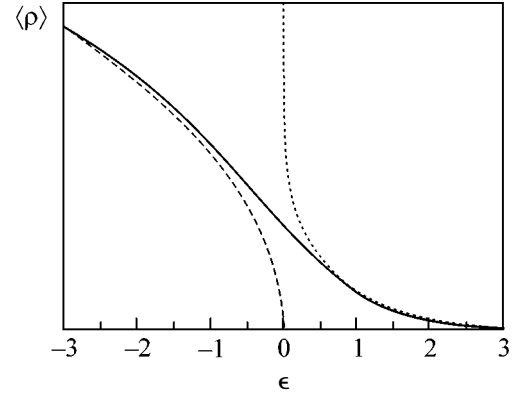
Fig. 2. (Solid line) Exact dependence (14) of the DOS on the dimensionless energy ϵ, (dotted line) single-instanton approximation (1), and (dashed line) semiclassical result (2) for the DOS.

$P = P_0 + \delta P$. Expanding the action in powers of δP, we get

$$S_0(P) = S_0(P_0) + \frac{G_T}{8}\left[-\varepsilon\delta P + \frac{2}{P_0^4}(\delta P)^3\right]. \qquad (19)$$

This equation closely resembles its counterpart (11) for the transparent interface. As mentioned in [4], this form of the expansion of the action in powers of small deviations near the threshold solution inevitably leads to the instanton action scaling as $\varepsilon^{3/2}$. In fact, there is full equivalence [17] between the DOS for the transparent NS interface given by Eq. (14) and the DOS in the limit $|\varepsilon| \ll t^{2/3} \ll 1$. The latter can be obtained from the former by redefinition of the constants $c_{1,2}$. For a 1D planar contact, they appear to be $c_1 = P_0/2$, $c_2 = 6/P_0$, $E_g/E_{\text{Th}} = t$.

In particular, above the threshold, at $\varepsilon < 0$, one encounters the mean-field square-root singularity

$$\langle\rho\rangle_{\text{MF}} = \frac{4}{\delta}\frac{6^{1/6}}{t^{2/3}}\sqrt{|\varepsilon|}. \qquad (20)$$

The instanton action becomes $\mathscr{S} = S_0(P_1) - S_0(P_2) = (2/3)6^{1/6}G_N t^{1/3}\varepsilon^{3/2}$, and the single-instanton asymptotic form of the DOS tail reads

$$\langle\rho\rangle = \frac{1}{\delta}\sqrt{\frac{\pi 6^{1/6}}{2G_N t^{5/3}\sqrt{\varepsilon}}}\exp\left(-\frac{2}{3}6^{1/6}G_N t^{1/3}\varepsilon^{3/2}\right). \qquad (21)$$

Strong tail. In the opposite limit, $t^{2/3} \ll |\varepsilon| \ll 1$, the difference between the two solutions to Eq. (18) is large but expansion (17) is still valid (gradients of $\psi_{1,2}$ are small, provided $\varepsilon \ll 1$). The roots $P_{1,2}$ can be found by neglecting either the second or the third term in Eq. (18): $P_1 = \sqrt{2/\varepsilon}$, $P_2 = 12\varepsilon/t$, with $P_2 \gg P_1$. Above

References to the asymptotic formulas for the DOS above ($\varepsilon < 0$) and below ($\varepsilon > 0$) the gap, and the width $|\varepsilon|_{\text{fluct}}$ of the fluctuation region for the regimes of the transparent interface ($t \gg 1$), weak ($|\varepsilon| \ll t^{2/3} \ll 1$) and strong ($t^{2/3} \ll |\varepsilon| \ll 1$) tails

	$\varepsilon < 0$	$\varepsilon > 0$	$|\varepsilon|_{\text{fluct}}$
$t \gg 1$	(2)	(1)	$G_N^{-2/3}$
$|\varepsilon| \ll t^{2/3} \ll 1$	(20)	(21)	$G_N^{-2/3} t^{-2/9}$
$t^{2/3} \ll |\varepsilon| \ll 1$	(22)	(23)	$G_N^{-1/2}$

the threshold, this gives the inverse-square-root singularity in the semiclassical DOS:

$$\langle \rho \rangle_{\text{MF}} = 2\nu \text{Re} \int d\mathbf{r} \cos\theta = \frac{1}{\delta} \text{Im}(P - P^{-1}) = \frac{1}{\delta}\sqrt{\frac{2}{|\varepsilon|}}. \quad (22)$$

Below E_g, one obtains for the instanton action $\mathcal{S} = -S_0(P_2) = (3/4)G_N\varepsilon^2$, which determines the one-instanton asymptotics of the subgap DOS. The preexponent can be calculated by generalizing the method of [2]. Introducing the deviation parameter q according to $\alpha = \pi/2 + i\log P_2 + iq/\sqrt{2}$ and expanding the action in powers of q and the corresponding Grassmann pair $\zeta\xi$, we obtain for the action and the preexponential factor in Eq. (3)

$$\mathcal{S} = \frac{3}{8}G_N\varepsilon^2\left[2 - q^2 + \frac{q\zeta\xi}{2\sqrt{2}}\right],$$

$$\frac{\nu}{4}\int d\mathbf{r}\,\text{str}(k\Lambda Q) = -\frac{3i\varepsilon}{t\delta}\left[1 - \frac{q}{\sqrt{2}}\right].$$

The measure of integration is $\mathcal{D}Q = 2\sqrt{3/t}\,(2\varepsilon)^{3/4}dq\,d\zeta\,d\xi$. Inserting these into Eq. (3), we finally obtain

$$\langle \rho \rangle = \frac{3}{\delta}\sqrt{\frac{\pi}{G_N t^3}}\sqrt{\frac{\varepsilon^3}{2}}\exp\left(-\frac{3}{4}G_N\varepsilon^2\right). \quad (23)$$

5. Discussion. We have considered the integral density of states in a coherent diffusive SNS junction with an arbitrary transparency of the SN interface. For the ideal interface ($G_T \gg G_N$), we managed to go beyond the single-instanton analysis [2] and derived the exact result (14), which is valid as long as $|E - E_g| \ll E_g$. This expression uniquely describes the semiclassical square-root DOS (2) above the Thouless gap E_g, the far subgap tail (1), and the crossover region $\varepsilon \sim G_N^{-2/3}$ between the two asymptotic expressions. The functional form of this result coincides with the prediction of the RMT.

As the SN interface becomes less transparent, $G_T \ll G_N$, the situation changes. At $G_T \gg G_N^{1/4}$, these changes

are only quantitative: the position of the quasiclassical gap is shifted to $E_g = (G_T/G_N)E_{\text{Th}}$, but the DOS both above [Eq. (20)] and below [Eq. (21)] the gap has the same dependence on the deviation ε from E_g, with the coefficients becoming dependent on G_T. In this limit, the very far part of the tail [at $\varepsilon \gg (G_T/G_N)^{2/3}$] exhibits a different ε dependence (23), but the corresponding DOS is exponentially small. Therefore, in the limit $G_T \gg G_N^{1/4}$, the total number of subgap states is on the order of 1 and independent of G_T. We refer to this case as weak tail.

As the interface becomes less transparent, the region of applicability of the weak tail shrinks and finally disappears at $G_T \sim G_N^{1/4}$. For even lower $G_T \ll G_N^{1/4}$, the difference between the case of the transparent interface becomes qualitative: the DOS above E_g acquires an inverse square-root dependence (22), while the subgap DOS follows Eq. (23). In this regime, the total number of subgap states is proportional to $G_T^{-1/2} G_N^{1/8} \gg 1$ and grows with decreasing G_T, in contrast to all previous cases where this number is on the order of 1. This indicates that at $G_T \sim G_N^{1/4}$ the universality class of the problem changes. At $G_T \ll G_N^{1/4}$, it is no longer equivalent to the spectral edge of the Wigner–Dyson random-matrix ensembles.

The asymptotic results for the DOS above and below the gap, as well as the width of the fluctuation region near E_g, are summarized in the table for the three regions considered.

REFERENCES

1. M. G. Vavilov, P. W. Brower, V. Ambegaokar, and C. W. J. Beenakker, Phys. Rev. Lett. **86**, 874 (2001).

2. P. M. Ostrovsky, M. A. Skvortsov, and M. V. Feigel'man, Phys. Rev. Lett. **87**, 027002 (2001).

3. A. Lamacraft and B. D. Simons, Phys. Rev. Lett. **85**, 4783 (2000).

4. A. Lamacraft and B. D. Simons, Phys. Rev. B **64**, 014514 (2001).

5. A. A. Golubov and M. Yu. Kupriyanov, Zh. Éksp. Teor. Fiz. **96**, 1420 (1989) [Sov. Phys. JETP **69**, 805 (1989)].

6. F. Zhou, P. Charlat, B. Spivak, and B. Pannetier, J. Low Temp. Phys. **110**, 841 (1998).

7. J. A. Melsen, P. W. Brower, K. M. Frahm, and C. W. J. Beenakker, Europhys. Lett. **35**, 7 (1996); Phys. Scr. **69**, 223 (1997).

8. S. Pilgram, W. Belzig, and C. Bruder, Phys. Rev. B **62**, 12462 (2000).

9. G. Eilenberger, Z. Phys. **214**, 195 (1968).

10. A. I. Larkin and Yu. N. Ovchinnikov, Zh. Éksp. Teor. Fiz. **55**, 2262 (1968) [Sov. Phys. JETP **28**, 1200 (1969)].

11. K. Usadel, Phys. Rev. Lett. **25**, 507 (1970).

12. C. A. Tracy and H. Widom, Commun. Math. Phys. **159**, 151 (1994); **177**, 727 (1996).

13. M. L. Mehta, *Random Matrices* (Academic, New York, 1991).

14. K. B. Efetov, *Supersymmetry in Disorder and Chaos* (Cambridge Univ. Press, New York, 1997).

15. A. Altland, B. D. Simons, and D. Taras-Semchuk, Pis'ma Zh. Éksp. Teor. Fiz. **67**, 21 (1997) [JETP Lett. **67**, 22 (1997)]; Adv. Phys. **49**, 321 (2000).

16. B. A. Muzykantskii and D. E. Khmelnitskii, Phys. Rev. B **51**, 5480 (1995).

17. P. M. Ostrovsky, M. A. Skvortsov, and M. V. Feigel'man, Zh. Éksp. Teor. Fiz. (in press) [JETP (in press)].

18. W. Belzig and Yu. V. Nazarov, Phys. Rev. Lett. **87**, 067006 (2001).

19. M. Yu. Kuprianov and V. F. Lukichev, Zh. Éksp. Teor. Fiz. **94** (6), 139 (1988) [Sov. Phys. JETP **67**, 1163 (1988)].

In situ Study of the Mechanism of Formation of Pressure-Densified SiO₂ Glasses

F. S. El'kin, V. V. Brazhkin*, L. G. Khvostantsev, O. B. Tsiok, and A. G. Lyapin

Institute of High-Pressure Physics, Russian Academy of Sciences, Troitsk, Moscow region, 142190 Russia
* e-mail: brazhkin@hppi.troitsk.ru
Received March 6, 2002

The volume of glassy a-SiO₂ upon compression to 9 GPa was measured *in situ* at high temperatures up to 730 K and at both pressure buildup and release. It was established that the residual densification of a-SiO₂ glass after high-pressure treatment was due to the irreversible transformation accompanied by a small change in volume directly under pressure. The bulk modulus of the new amorphous modification was appreciably higher (80% more than its original value), giving rise to residual densification as high as 18% under normal conditions. It was shown that the transformation pressure shifted to a lower pressure of about 4 GPa with a rise in temperature. A conclusion was drawn about the existence of at least two pressure-induced phase transitions accompanied by structure rearrangement in a-SiO₂. A nonequilibrium phase diagram is suggested for glassy SiO₂. It accounts for all the presently available experimental data and is confirmed by the existing modeling data. © *2002 MAIK "Nauka/Interperiodica".*

PACS numbers: 62.50.+p; 64.70.Pf

1. The pressure- and temperature-induced structural phase transitions in crystals have been well explored both experimentally and theoretically. At the same time, the nature and specific features of transformations in amorphous solids and glasses call for further investigation [1–3]. The studies of pressure-induced transformations in classical glasses such as a-SiO₂ are, perhaps, of special interest [4–12]. In spite of considerable experimental and theoretical efforts, the problem of describing pressure-induced a-SiO₂ transformations has not been adequately resolved so far [1–21]. The reasons for this are caused not only by the fundamental problems associated with the description of phase transitions in disordered media [2] but also by the rather complicated phase diagram of crystalline silica [4, 22, 23], for which the well-known low-pressure SiO₂ phases are stable: α- and β-quartz modifications, cristobalite, and tridymite; at higher pressures $P > 3$ GPa, the coesite phase becomes stable and, starting at 10 GPa and up to ~50 GPa, stishovite becomes a stable silica phase. In all low-pressure phases, silicon atoms have a tetrahedral environment ($Z = 4$) formed by divalent oxygen atoms, but coesite is a denser phase because the SiO₄ tetrahedra in it are packed more densely topologically [4]. In ever denser stishovite (rutile structure), the silicon atoms are positioned in an octahedral environment ($Z = 6$) and oxygen is trivalent [4].

There still remains much to be understood about the nature of the residual densification, which persists in the compressed glassy silica a-SiO₂ after pressure release and arises as a gradual process under pressures of 8–10 GPa at room temperature [4–7, 9, 15] and even

under pressures of 2–3 GPa at high temperatures of 700–1100 K [6]. At normal conditions, the maximal residual densification in glassy SiO₂ attains the value $\Delta\rho/\rho = (16–20)\%$ [4–7, 10, 24, 25] after treating with a pressure of 16–18 GPa at room temperature, 7–8 GPa in the temperature range 800–900 K, and, correspondingly, 4–5 GPa at $T \sim 1000$ K [4–7, 10, 24–26]. The elastic moduli and optical characteristics of densified SiO₂ glasses are markedly different from the moduli of the original glasses [4–7, 9, 27]. It is worth noting that, at normal conditions, the densified glasses are also characterized mainly by the tetrahedral environment composed of the oxygen atoms with virtually unchanged bond lengths and a slightly smaller average Si–O–Si angle [10, 24, 28]. At normal pressure and over a wide temperature range from 700 to 1200 K, the densified glass relaxes, with low activation energies, to its original density [6, 29].

In recent years, studies of the structure [11] and the Raman and Brillouin spectra [7–9, 12] of a-SiO₂, as well as the results of computer simulation [16–21], have shown that in the pressure range 12–40 GPa at room temperature a-SiO₂ undergoes transformation with a change of the short-range order and a gradual increase in the average silicon nearest neighbor coordination number from ≈4 to ≈6. This transformation is, to a large extent, reversible, so that the Si coordination number practically regains its original value of ≈4 after pressure release [10, 16–21, 24, 28].

To date, it has been unclear whether the transformation accompanied by the short-range rearrangement from the tetrahedral to octahedral coordination is rele-

vant to the residual glass densification after pressure release. It has also remained unknown to what extent the processes leading to glass densification at high pressures $P > 10$ GPa at room temperature and at pressures $P \approx 4$–6 GPa at high temperatures are common in nature. Note that *in situ* volume measurements have not been carried out so far for a-SiO$_2$ under pressure and under conditions providing for irreversible glass densification. It has only recently been established by *in situ* measurements that, at the beginning stage of irreversible a-SiO$_2$ densification at room temperature ($P \approx$ 9 GPa), the volume relaxation obeys the logarithmic law [15]. While this paper was being prepared for publication, paper [26] was issued, in which the *in situ* volume measurements with heating at $P = 3.6$ GPa were reported for a-SiO$_2$ and in which a considerable volume anomaly was observed in a rather narrow temperature interval $T \approx 880$–960 K.

In this work, the density of glassy silica a-SiO$_2$ was *in situ* measured at high pressures up to 9 GPa and temperatures up to 730 K for both an increase and decrease of pressure. The obtained experimental results and an analysis of literature data made it possible to formulate a conceptually new nonequilibrium phase diagram for glassy SiO$_2$.

2. The starting glassy silica samples were parallelepipeds ($3 \times 2 \times 2$ mm) made from a nonporous glass with density $\rho = 2.21$ g/cm^3. The sample volumes at high pressure were measured by the strain gauge technique, which was originally developed in [30] for measurements at room temperature. By the absolute accuracy of volume measurements, this method is comparable to the X-ray technique (for crystals), while its sensitivity is several orders higher. To perform high-temperature measurements, the method [30] was substantially modified. The details will be published elsewhere.

High pressure was produced using apparatus of the toroid type [31] with an operating volume of ~1 cm^3. These apparatus provided hydrostatic conditions for pressure measurements up to 10 GPa with fine pressure control at high temperatures. A mixture of pentane with petroleum ether ($3 : 2$) was used as a transmitting medium, because it retained hydrostatic properties up to approximately 6 GPa at room temperature. At higher pressures, this mixture was used only at high temperatures, correspondingly, in the region where it provided hydrostatic conditions. The rates of varying pressure and temperature were, respectively, 0.05 GPa/min and 0.3 K/s.

3. The curves for the relative change in volume of the a-SiO$_2$ samples under pressure are shown in Fig. 1a. The discontinuities in the curves at pressures 1.8–3.7 GPa correspond to the sample heating and cooling steps. The room-temperature curves [15] are also presented for comparison. Starting at a certain moment upon pressure buildup, the curves deviate from their standard regular behavior corresponding to a linear
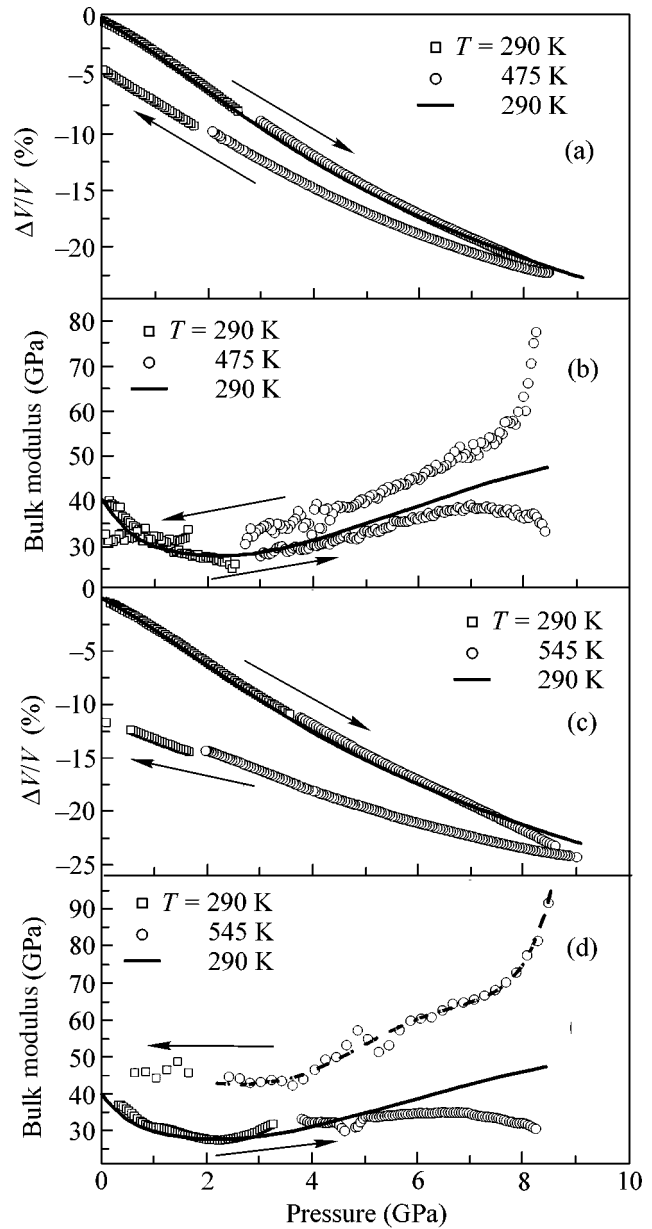
Fig. 1. (a, c) Relative changes of a-SiO$_2$ volume in the compression and unloading cycles (the initial and final portions were measured at room temperature) and (b, d) the corresponding bulk moduli obtained by the numerical differentiation of volume curves (for $T = 475$ K, the curves were differentiated directly, and, for $T = 545$ K, the curves were smoothed out before the differentiation because of the enhanced noise level). The data corresponding to the a-SiO$_2$ compression at room temperature are given for comparison.

change in the bulk modulus. This is most clearly seen from the softening of the bulk modulus (Figs. 1b, 1d), whose pressure dependence is obtained by the numerical differentiation of the volume curves. The higher the temperature, the earlier the compressibility anomaly is observed, starting at pressures of ≈ 5.7 and 6.7 GPa at temperatures of 475 and 545 K, respectively. The
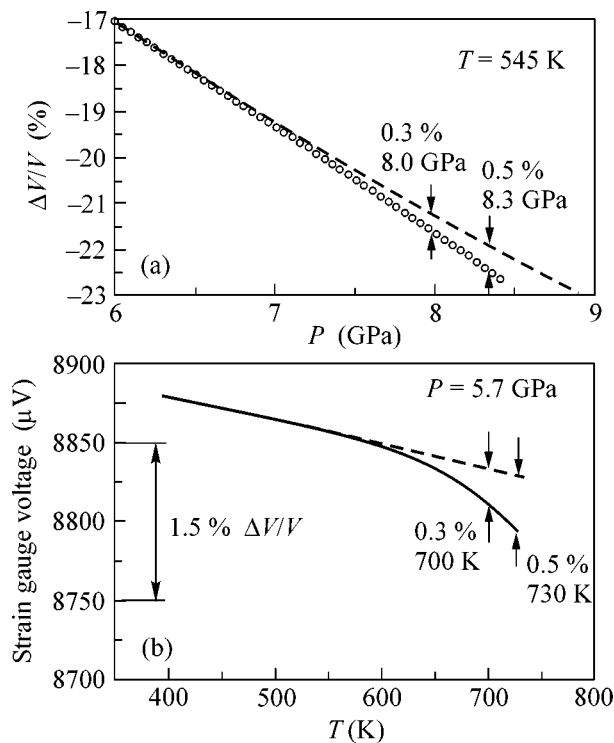
Fig. 2. Enlarged fragments of the (a) pressure and (b) temperature dependence of relative volume change in the region of the anomaly associated with the irreversible densification of *a*-SiO$_2$. In the second case, the data were not recalculated to the relative change, because the calibration experiments were not carried out in the temperature range below 730 K, but the magnitude of the anomaly and its onset at ~600 K were determined rather reliably from our data.

region of the volume anomaly for the amorphous SiO$_2$ is shown in Fig. 2a on the enlarged scale. It is worth noting that the magnitude of the volume anomaly at high pressure is as low as ≈0.7 and 1.5% at 475 and 545 K, respectively.

As the pressure is reduced, the behavior of the *a*-SiO$_2$ volume becomes essentially irreversible, because the glass compressibility in the new state diminishes. As a result, a large residual densification (~5 and ~12% in the experiments presented in Figs. 1a and 1c, respectively) is observed under normal conditions. Indeed, it follows from the data obtained in this work that the bulk modulus of the glass in the new state (Figs. 1b, 1d) exceeds, at the same pressure, the corresponding value in its initial state by a factor of almost 1.5 even if the transformation is incomplete, which is in compliance with the literature data [4, 7, 9, 12].

The thermobaric treatment of the *a*-SiO$_2$ sample at a high pressure of 8.6 GPa and a temperature of 870 K (the highest possible temperature for the liquid used) gave a sample with maximal (18%) residual densification. This is the highest residual densification ever observed in experiment [5, 6, 10, 24, 25], and, hence, it

can be used for estimating the width of the transition to the new densified glass state. The values $B = 68.1$ GPa and $G = 45.1$ GPa obtained under normal conditions for, respectively, the bulk and shear moduli in our precise ultrasonic measurements of the elastic properties of glasses with the highest residual densification are considerably larger than the respective values $B = 38.6$ GPa and $G = 29.7$ GPa in the initial glass.

The anomalous glass densification was also observed on heating *a*-SiO$_2$ at high pressures. Figure 2b presents the envelope of four heating–cooling cycles at a pressure of 5.7 GPa. By summing the results of all our *in situ* measurements of the *a*-SiO$_2$ volume, we succeeded in determining rather accurately the region corresponding to the structural transition to a denser *a*-SiO$_2$ modification in the phase diagram, including the onset of this process and its more intense stage (Fig. 3). The extrapolation of the data obtained in this work to the high-temperature region (Fig. 3) suggests that, at high temperatures near the crystallization temperature, the structural densification of *a*-SiO$_2$ occurs near 3–4 GPa, in accordance with the data reported in recent work [26]. The temperature interval of reverse transformation to a less dense glass was estimated using the isochronous annealing of the prepared densified glasses at normal pressure and found to be equal to 1000–1100 K (for an annealing rate of 20 K/min).

4. The following fundamental conclusions can be drawn from the obtained results.

First, the *a*-SiO$_2$ transformation resulting in the residual glass densification is accompanied, directly under pressure, by a small (few percent) change in volume and is fully irreversible. Formally, much of the residual glass densification at normal conditions is due to a markedly lower compressibility of *a*-SiO$_2$ after transformation (Fig. 1). At atmospheric pressure, the bulk modulus of the glass with maximal (18%) residual densification is higher by 80% than in the initial glass.

Second, it has become clear that the processes of irreversible *a*-SiO$_2$ densification at pressures higher than 9 GPa at room temperature, and at high temperatures and lower pressures of 5–7 GPa, are due to the same structural transformation.

Consequently, the transition observed in *a*-SiO$_2$ at room temperature in the pressure range 10–40 GPa upon changing the silicon coordination number from four to six is unrelated to irreversible residual glass densification. *Therefore, at least two pressure- and temperature-smeared transformations accompanied by a marked change in the structure and properties of a-SiO$_2$ should exist at pressures below 40 GPa (Fig. 4).* By analogy with the quartz–coesite phase transition, the first transformation does not noticeably distort the tetrahedral (for the Si atoms) short-range structure. It is irreversible at room temperature and brings about the residual densification. The second transformation occurs at higher pressures. It is accompanied by a
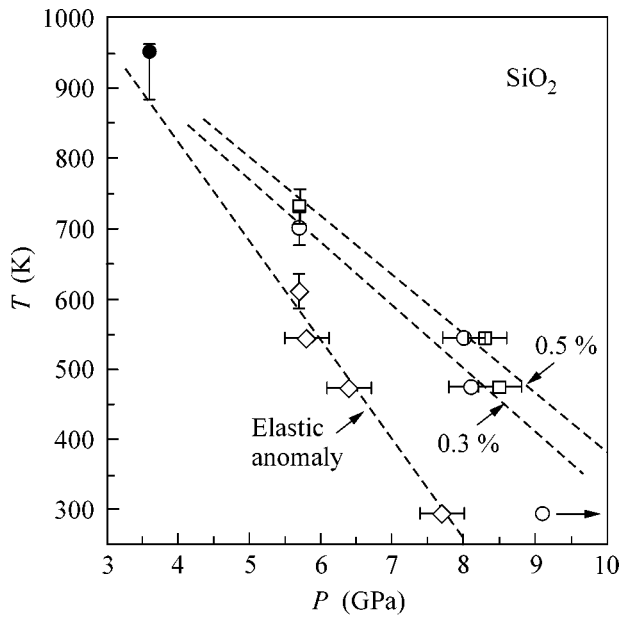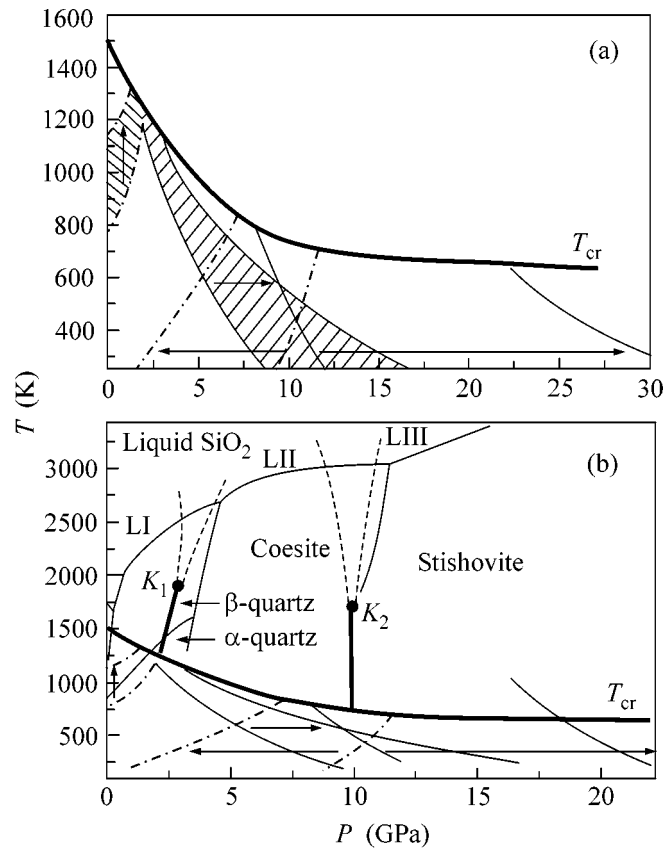
Fig. 3. The experimental points corresponding to the ($\diamond$) onset of elastic anomaly and the compression ratios of ($\circ$) 0.3 and ($\square$) 0.5% allow the region (dashed lines) of irreversible *a*-SiO$_2$ transformation into a denser glass to be determined in the pressure–temperature diagram. The point at $P = 3.6$ GPa corresponds to the transition according to [26].

Fig. 4. (a) Phase diagram for the transformations of glassy SiO$_2$ below the crystallization temperature T_{cr} (the curve is constructed using the data from [6, 10, 25, 26, 32]). These data are evidence for the two transitions: between the ordinary and densified tetrahedral phases (the hatched regions correspond to the direct and reverse transitions) and between the densified tetrahedral and octahedral phases (nonhatched regions). The regions of direct transitions are bounded by the solid lines, and the regions of reverse transitions are bounded by the dot-and-dash lines. The boundaries of transition regions are drawn rather arbitrarily. The arrows show the directions of the corresponding transitions. (b) The thermodynamic phase diagram of SiO$_2$ [22, 23] and the hypothetical diagram of liquid SiO$_2$ with two possible first-order phase transitions in a supercooled liquid state and two corresponding critical points (K_1 and K_2). The liquid–liquid phase transitions correspond to the broadened regions of structural rearrangement (between the states LI, LII, and LIII) in the ordinary liquid and, below the temperature T_{cr}, to the transitions between the amorphous states labeled according to the diagram (a).

change in the silicon coordination from tetrahedral to octahedral, by analogy with the coesite–stishovite phase transition, and is reversible at room temperature. The diagram for both *a*-SiO$_2$ transformations, constructed using the experimental results of this work and the literature data, is presented in Fig. 4a.

At room temperature, the pressures of both transformations overlap, whereas the reverse transitions are well separated in pressure (Fig. 4). Previous conclusions drawn about the possible interconnection between the residual densification in *a*-SiO$_2$ and its high-pressure transformation with changing short-range structure were based precisely on this fact.

The first transition from the "quartz" tetrahedral glass to the densified tetrahedral glass is, evidently, accompanied not only by a change in the packing of SiO$_4$ tetrahedra but also by a change in the topology of tetrahedron connectivity. This scenario is confirmed by modeling the compression of a purely tetrahedral glass [16]. In accordance with our experimental data, the pressure-induced topological changes in the medium-range structure are not accompanied by a sizable change in the degree of tetrahedron packing, but the change of bonding between the tetrahedra leads to a substantial change in compressibility. It is natural to expect that, similar to coesite, a great number of four-membered rings of mutually bonded SiO$_4$ tetrahedra appear in the densified tetrahedral glass, and the aver-age Si–O–Si angle between the tetrahedra may serve as the transition order parameter.

The second transformation to the octahedral "stishovite" glass is accompanied by the rearrangement of atomic packing in glass and, evidently, is due to short-range tetrahedral instability. It is conceivable that the angle of twisting SiO$_4$ tetrahedra may serve as the order parameter for this transformation [33].

The presence of two different transformations in a-SiO_2 allows for the explanation of practically all presently available experimental data concerning the behavior of a compressed glassy silica [2–12] and, at the same time, agrees well with the existing model calculations [16–21]. If such is the case, all the existing contradictions in the interpretation of the results of different works are removed. In particular, molecular dynamic studies of compressed a-SiO_2 have recently been carried out in [19, 20]. In [19], the second reversible transition to the octahedral glass was, in fact, analyzed, while a thermodynamic analysis of the transformation between the low- and high-density phases of the tetrahedral glass at relatively low pressures was given in [20].

The conclusion about two transformations in a-SiO_2 (Fig. 4a) allows some other assumptions to be made about the phase diagram of SiO_2 (Fig. 4b). It is natural to assume that two analogous transformations occur in a SiO_2 melt. This is indirectly confirmed by the data reported in [34–37], where the first transition showed up as a change in the degree of densification for glasses prepared by quenching from a melt under pressure [34], and the second transition was associated with a substantial rearrangement of the atomic short-range order and caused the anomalous properties of the SiO_2 melt [35–37]. In turn, the assumption can be made that two first-order phase transitions and the corresponding critical points may exist in a supercooled SiO_2 liquid (Fig. 4b).

Thus, at least two sequential pressure-induced transformations with material volume and structural changes occur in glassy silica. The first transformation is accompanied by a change in the type of packing of the SiO_4 tetrahedra and is irreversible at room temperature, whereas the second transformation is accompanied by a change of the silicon coordination from tetrahedral to octahedral and is reversible at room temperature. At low temperatures, the pressures of these transformations overlap, whereas at high temperatures they are, likely, separated. The presence of two transitions in the amorphous and, correspondingly, liquid state is a phenomenon which is, presumably, typical of other substances in which a hierarchy of phase transitions in the crystal state is accompanied by a change in the topology of submolecular ordering followed by a change in the short-range order and in the type of atomic packing. For instance, the occurrence of the second transition between the amorphous phases may be expected for H_2O at higher pressures and low temperatures.

REFERENCES

1. A. G. Lyapin, V. V. Brazhkin, E. L. Gromnitskaya, *et al.*, Usp. Fiz. Nauk **169**, 1157 (1999).

2. V. V. Brazhkin, A. G. Lyapin, S. V. Popova, and R. N. Voloshin, *New Kinds of Phase Transitions: Transformations in Disordered Substances*, Ed. by V. V. Brazhkin *et al.* (Kluwer, Dordrecht, 2002).

3. A. G. Lyapin, V. V. Brazhkin, E. L. Gromnitskaya, *et al.*, in *New Kinds of Phase Transitions: Transformations in Disordered Substances*, Ed. by V. V. Brazhkin *et al.* (Kluwer, Dordrecht, 2002).

4. R. J. Hemley, C. T. Prewitt, and K. J. Kingma, in *Silica: Physical Behavior, Geochemistry and Materials Applications*, Ed. by R. J. Hemley, C. T. Prewitt, and G. V. Gibbs (Mineralogical Society of America, Washington, 1994), Reviews in Mineralogy, Vol. 29, p. 41.

5. P. W. Bridgman and I. Simon, J. Appl. Phys. **24**, 405 (1953).

6. H. M. Cohen and R. Roy, Phys. Chem. Glasses **6**, 149 (1965).

7. M. Grimsditch, Phys. Rev. Lett. **52**, 2379 (1984).

8. R. J. Hemley, H. K. Mao, P. M. Bell, and B. O. Mysen, Phys. Rev. Lett. **57**, 747 (1986).

9. M. Grimsditch, Phys. Rev. B **34**, 4372 (1986).

10. Th. Gerber, B. Himmel, H. Lorenz, and D. Stachel, Cryst. Res. Technol. **23**, 1293 (1988).

11. C. Meade, R. J. Hemley, and H. K. Mao, Phys. Rev. Lett. **69**, 1387 (1992).

12. C. S. Zha, R. J. Hemley, H. K. Mao, *et al.*, Phys. Rev. B **50**, 13105 (1994).

13. E. M. Stolper and T. J. Ahrens, Geophys. Res. Lett. **14**, 1231 (1987).

14. V. G. Karpov and M. Grimsditch, Phys. Rev. B **48**, 6941 (1993).

15. O. B. Tsiok, V. V. Brazhkin, A. G. Lyapin, and L. G. Khvostantsev, Phys. Rev. Lett. **80**, 999 (1998).

16. L. Stixrude and M. S. T. Bukowinski, Phys. Rev. B **44**, 2523 (1991).

17. J. S. Tse, D. D. Klug, and Y. Le Page, Phys. Rev. B **46**, 5933 (1992).

18. R. J. Della Valle and E. Venuti, Phys. Rev. B **54**, 3809 (1996).

19. D. J. Lacks, Phys. Rev. Lett. **80**, 5385 (1998).

20. D. J. Lacks, Phys. Rev. Lett. **84**, 4629 (2000).

21. E. Demiralp, T. Cagin, and W. A. Goddard, III, Phys. Rev. Lett. **82**, 1708 (1999).

22. E. Yu. Tonkov, *High Pressure Phase Transformations: A Handbook* (Gorgon and Breach, Philadelphia, 1992; Metallurgiya, Moscow, 1988), Vol. 1, p. 601.

23. V. Swamy, S. K. Saxena, B. Sundman, and J. Zhang, J. Geophys. Res. **99**, 11787 (1994).

24. S. Susman, K. J. Volin, D. L. Price, *et al.*, Phys. Rev. B **43**, 1194 (1991).

25. Y. Inamura, M. Arai, N. Kitamura, *et al.*, Physica B (Amsterdam) **241**, 903 (1997).

26. G. D. Mukherjee, S. N. Vaidya, and V. Sugandhi, Phys. Rev. Lett. **87**, 195501 (2001).

27. P. McMillan, B. Piriou, and R. Couty, J. Chem. Phys. **81**, 4234 (1984).

28. R. A. B. Devine, R. Dupree, I. Farnan, and J. J. Capponi, Phys. Rev. B **35**, 2560 (1987).

29. J. D. Mackenzie, J. Am. Ceram. Soc. **46**, 470 (1963).

30. O. B. Tsiok, V. V. Bredikhin, V. A. Sidorov, and L. G. Khvostantsev, High Press. Res. **10**, 523 (1992).

31. L. G. Khvostantsev, L. F. Vereshchagin, and A. P. Novikov, High Temp. – High Press. **9**, 637 (1977).

32. K. Suito, M. Miyoshi, and A. Onodera, High Press. Res. **16**, 217 (1999).

33. S. V. Goryaĭnov and N. N. Ovsyuk, Pis'ma Zh. Éksp. Teor. Fiz. **69**, 431 (1999) [JETP Lett. **69**, 467 (1999)].

34. M. Kanzaki, J. Am. Ceram. Soc. **73**, 3706 (1990).

35. E. Ohtani, F. Taulelle, and C. A. Angell, Nature **314**, 78 (1985).

36. J. Zhang, R. C. Liebermann, T. Gasparik, *et al.*, J. Geophys. Res. **98**, 19785 (1993).

37. I. Saika-Voivod, F. Sciortino, and P. H. Poole, Phys. Rev. E **63**, 11202 (2000).

Translated by V. Sakun

Excitations in a Quantum Hall Ferromagnet with Strong Coulomb Interaction[1]

S. V. Iordanski and A. Kasbuba

Landau Institute for Theoretical Physics, Russian Academy of Sciences, Moscow, 117334 Russia
Received March 7, 2002

A quantum Hall ferromagnet is considered at integer fillings ν, provided typical Coulomb interaction energy E_c is large compared to the cyclotron energy ω_H. Low-energy collective modes consist of a magnetoplasmon exciton and a gapless spin exciton. All charged excitations have a gap. The activation energy gap for a pair of charged topological excitations—skyrmion and antiskyrmion—is small, i.e., $\Delta < \nu\omega_H$. The electric charge of a skyrmion is the multiple $q = evQ$, where Q is the integer topological charge. © 2002 MAIK "Nauka/Interperiodica".

PACS numbers: 71.27.+a; 73.43.Cd.; 71.35.Lk

A commonly used theoretical approach for the 2D electron quantum Hall state is to consider the limit of extremely large cyclotron energy ω_H compared to typical Coulomb interaction energy E_c, when electron wave functions can be projected onto the states of several of the lowest Landau levels [1–3]. The simplest case corresponds to a nondegenerate Fermi gas, with all states within the lowest Landau levels being filled. In particular, one finds a ferromagnetic ordering due to the exchange Coulomb interaction. In the limit $r_s = E_c/\omega_H \longrightarrow 0$, it is possible to find the exact energies and wave functions of electron and hole excitations, as well as various collective excitations with charge and spin distortions of the ground state [1–3]. This model also features topological charged excitations—skyrmions—that render the activation energy twofold lower then that for an electron–hole pair excitation [4]. However, in real experiments the condition of small r_s is violated, and for Si heterostructures and organic MOSFETs based on molecular crystals this violation is quite severe with $r_s \sim 10$ [5, 6]. Newly developed AlAs heterostructures also fall in the class of strongly interacting 2DEG. Some predictions of the standard theoretical model are not consistent with experiments even in the simplest case of integer filling ν. The most apparent discrepancy concerns the activation gap for charged excitations, which is found to be substantially smaller than the predicted exchange Coulomb energy [6] and linearly depends on the strength of the magnetic field. In this letter, we consider the opposite case of the theoretical model, with the Coulomb interaction being large compared to the cyclotron energy: $r_s = E_c/\omega_H \gg 1$. In spite of computational difficulties, it is possible to make some predictions concerning the lowest energy of various collective excitations and charged topological excitations (skyrmions) in this limit.

Obviously, with a strong Coulomb interaction, the ground state does not coincide with the Hartree–Fock ground state, where electrons completely occupy several of the lowest Landau levels (Ll). Actually, one has to take into account virtual transitions to a number of higher Ll's and, therefore, the projection of the electron wave function onto several of the lowest Ll states is invalid. It is difficult to construct analytically the ground-state wave function or to find corresponding correlation functions. The ground state of an ideal electron gas with integer Ll fillings is nondegenerate and, therefore, it is possible to use the perturbation theory in powers of interaction and to assume, in the spirit of the Landau Fermi liquid theory, that the exact summation of perturbation series will preserve the ideal Fermi-gas classification of one-particle excitations. There are quasielectron and quasihole excitations with different energies $\varepsilon_e(s)$ and $\varepsilon_h(s)$, where the index s counts the discrete energy levels of charged quasi-particles in a magnetic field. In [7], an excitation gap $\Delta_{eh} = \min_{ss'}(\varepsilon_e(s) - \varepsilon_h(s')) = 0.1\,E_c$ was established numerically. These levels must be degenerate in the continuous index p, which specifically depends on the gauge because of the existence of magnetic translations commuting with the Hamiltonian but not commuting between themselves. The one-particle Green's function matrix $G_{nn'}(p, \omega)$ is not diagonal in inter-Ll indices n and n' but it is diagonal in the intra-Ll index p; ω is the time Fourier frequency. We assume that the one-particle Green's function has simple poles at these energies:

$$G(p, s, \omega) \approx \frac{A_s}{\omega - \varepsilon_e(s) - i\delta},$$

$$G(p, s, \omega) \approx \frac{B_s}{\omega - \varepsilon_h(s) + i\delta}. \tag{1}$$


Here, the index s denotes quasiparticle eigenstates diagonalizing the Green's function $G_{nn'}(p, \omega) = \sum_s \phi_n(s) G(p, s, \omega)\phi_n^*(s)$, where $\phi_n(s)$ are the one-particle quasiexcitation wave functions.

It is possible to relate the position of chemical potential μ, assumed to be inside the excitation gap Δ_{eh}, with the total density of electrons, in the same way as it is done in the case of usual Fermi liquid theory taking into account the phase and analytical properties of the Green's function [8, 9]. We consider a special topological invariant constructed from the Matsubara Green's functions [10]:

$$\nu' = \frac{1}{2\pi i}\int_C \mathrm{Tr}(G(p, \omega)\boldsymbol{\nabla} G^{-1}(p, \omega))d\mathbf{l}. \qquad (2)$$

The integrand is a logarithmic derivative of the one-particle Green's function on the plane, with the two axis being the Matsubara frequency $\omega = i\omega$ and the continuous gauge index p. $G_{nn'}(\omega, p)$ is a matrix with inter-Ll indices n and n', and the gradient is a vector in the p, ω plane. If the contour C is drawn in a region p, ω free of singularities in $\log(\det G)$, then the integrand (2) is a closed form and, therefore, gives a topological invariant quantity not depending on the form of closed contour C in this region. If there is no singularity inside the contour C, then $\nu' = 0$, otherwise it gives some integer number, because the complex matrix G is single-valued. Assuming a Landau gauge, the variable p coincides with the Y coordinate of the center of an electron orbit, which is restricted to the area of the sample occupied by 2D electrons. The fermi liquid electron Green's function (1) has no singularities or zeroes inside the sample, and the only singularity of the integrand can be found on a boundary at small ω due to the existence of edge states. Therefore, integration over a macroscopically large rectangular contour C with its sides parallel to the p and ω axes (see figure with dashed region representing the 2DEG) gives some integer number that depending on the position of chemical potential and related to the edge plasmon modes. In this case one can neglect the contributions to (2) from the horizontal sides since G is essentially $1/\omega$ not depending on p deep inside the 2DEG due to the gauge invariance. The only nonzero contribution comes from the vertical side of C inside the 2DEG, because the integration over the other vertical side outside the sample gives zero (no electrons in any state). Thus, we get the integer

$$\nu = \int_{-\infty}^{\infty} \mathrm{Tr}\left(G(p, \omega)\frac{\partial}{\partial\omega}G^{-1}(p, \omega)\right)\frac{d\omega}{2\pi i}, \qquad (3)$$
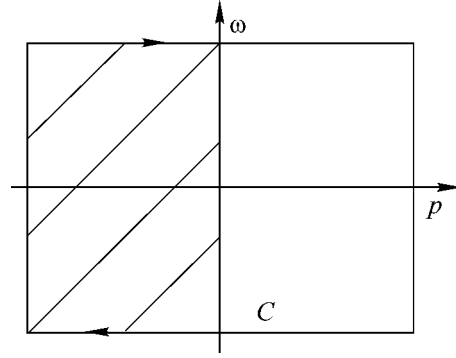
Contour C of integration for the topological Green's function invariant. The dashed area coincides with the 2DEG sample.

for any p inside the sample. Using the definition of the density in terms of the Green's function [8]

$$N = \sum_p \int_{-\infty}^{\infty} \mathrm{Tr}G(p, \omega)e^{i\omega\delta}\frac{d\omega}{2\pi i}, \qquad (4)$$

where $\delta \longrightarrow +0$, and the definition of the self-energy

$$G_{nn'}^{-1}(p, \omega) = (\omega - n\omega_H)\delta_{nn'} - \Sigma_{nn'}(s, p, \omega), \qquad (5)$$

we rewrite the density in a convenient form:

$$N = \sum_p \int_{-\infty}^{\infty} \mathrm{Tr}\left[G(p, \omega)\frac{\partial}{\partial\omega}G^{-1}(p, \omega)\right.$$
$$\left. + G(p, \omega)\frac{\partial\Sigma(p, \omega)}{\partial\omega}\right]e^{i\omega\delta}\frac{d\omega}{2\pi i}. \qquad (6)$$

Due to the existence of the Luttinger and Ward functional [9], the variation of which reads

$$\delta X = \sum_p \int_{-\infty}^{\infty} \mathrm{Tr}\Sigma(p, s, \omega)\delta G(p, s, \omega)\frac{d\omega}{2\pi}, \qquad (7)$$

we can eliminate the second term in the brackets as being exactly zero. Summing Eq. (3) over all p, we get, in accordance with Eq. (6), the total number of electrons

$$N = \nu\sum_p = \nu\frac{S}{2\pi l_H^2}, \qquad (8)$$

assuming the periodic conditions along the y direction $p = n/2\pi L_y$, $L_x > l_H^2 p > 0$ and $l_H^2 = c\hbar/eH$. This gives a standard expression for the electron density, $n_e = \nu/2\pi l_H^2$. Thus, we have shown that our Fermi liquid assumptions for the electron Green's function are valid only for an electron density corresponding to the integer fillings.

It is possible to establish the properties of low-energy collective excitations in the large r_s limit. One of these excitations is the magnetoplasmon mode, or Kohn exciton, associated with the following operators in the Landau gauge:

$$\Pi^{\pm}(\mathbf{q}) = \frac{1}{\sqrt{2}}\int e^{\pm i\mathbf{q}\mathbf{r}}(j_y \pm i j_x)d^2\mathbf{r}. \qquad (9)$$

Here, $\mathbf{j}(\mathbf{r})$ is the current density operator in the second quantized representation and Landau gauge

$$j_x = \frac{1}{2}\left\{\psi^{+}\left(-i\frac{\partial}{\partial x}\right)\psi + i\frac{\partial\psi^{+}}{\partial x}\psi\right\},$$

and

$$j_y = \frac{1}{2}\left\{\psi^{+}\left(-i\frac{\partial}{\partial y} + x\right)\psi - \left[\left(-i\frac{\partial}{\partial y} - x\right)\psi^{+}\right]\psi\right\}.$$

Operators $\Pi^{\pm}(\mathbf{q})$ raises/lowers the Ll index by unity, whereas operators $\Pi^{\pm}(\mathbf{0})$ commute with the Coulomb part of the Hamiltonian

$$H_c = \frac{1}{2}\int V(\mathbf{q})\rho(\mathbf{q})\rho(-\mathbf{q})\frac{d^2\mathbf{q}}{(2\pi)^2}, \qquad (10)$$

where $\rho(\mathbf{q})$ is the Fourier component of the density operator $\psi^{+}(\mathbf{r})\psi(\mathbf{r})$. The commutator of $\Pi^{+}(0)$ with the kinetic energy can easily be calculated and we get $H\Pi^{+}(0)|0\rangle = (\omega_H + E_0)\Pi^{+}(0)|0\rangle$, where $|0\rangle$ is the ground-state wave function, and E_0 is the ground-state energy. Thus, $\Pi^{+}|0\rangle$ is also an eigenstate of the Hamiltonian—a statement known as the celebrated Kohn theorem [11]. It gives the lowest energy of the magnetoplasmon. Similarly, we find $\Pi^{-}(0)|0\rangle = (E_0 - \omega_H)\Pi^{-}(0)|0\rangle$. This is compatible with the assumption that $|0\rangle$ is the ground state only if $\Pi^{-}(0)|0\rangle = 0$. This property originates from the ideal Fermi gas and survives switching on interaction.

As the Kohn exciton is neutral it can be classified by the momentum vector $\mathbf{q}$, and the operator $\Pi^{+}(\mathbf{q})$ is essentially the first term in the expansion of the true exciton creation operator in powers of $\mathbf{q}$. Finite momentum gives rise to a dispersion of the Kohn exciton $\omega_{ex}(\mathbf{q}) = \omega_H + \delta\omega_{ex}(\mathbf{q})$. It is possible to find exactly the main part of this dispersion for small $\mathbf{q}$.

The derivation can be done in terms of density operator $\rho(\mathbf{q}, t)$ and current density operator $\mathbf{j}(\mathbf{q}, t)$ in the Heisenberg representation. There are two equations of motion: the continuity equation for density

$$\frac{\partial\rho}{\partial t} + i\mathbf{q}\cdot\mathbf{j}(\mathbf{q}) = 0 \qquad (11)$$

and the equation of motion for current

$$\frac{\partial\mathbf{j}}{\partial t} = \frac{e}{mc}\mathbf{H}\times\mathbf{j}(\mathbf{q}) + n_e\mathbf{q}V(q)\rho(\mathbf{q}). \qquad (12)$$

Finding a "hydrodynamic" expression for the frequency of magnetoplasmon at small $\mathbf{q}$ ($ql_H \ll 1$) is straightforward:

$$\omega_{ex}(\mathbf{q}) = \sqrt{\omega_H^2 + \frac{n_e}{m}V(q)\mathbf{q}^2}. \qquad (13)$$

One can check that the corresponding two-particle Green's function has a pole at frequency (13). At very small $\mathbf{q}$, we get $\delta\omega_{ex}(\mathbf{q}) = e^2\nu|\mathbf{q}|/2$. The hydrodynamic Eqs. (11) and (12) are valid only at $q \ll \sqrt{n_e}$, which gives the Kohn exciton limiting energy bound: $\omega_{ex}(\mathbf{q}) < \Delta_{ex} \approx \sqrt{e^2 n_e\sqrt{n_e}/m}$.

The other collective mode is the Goldstone spin wave created by an operator

$$S^{\pm}(\mathbf{q}) = \int e^{\mp i\mathbf{q}\mathbf{r}}\psi_{\alpha}^{+}(r)\sigma_{\alpha\beta}^{\pm}\psi_{\beta}(r)d^2\mathbf{r},$$
$$\sigma^{\pm} = (\sigma_x \pm i\sigma_y)/2, \qquad (14)$$

where σ_i are the Pauli matrices. These operators commute with the total Hamiltonian at $\mathbf{q} = 0$ in the exchange approximation (neglecting spin–orbit and Zeeman interaction terms). This fact is a consequence of the global symmetry of the Hamiltonian with respect to rotations in a spin space. Spin-wave excitations are also neutral and, therefore, are classified by momentum $\mathbf{q}$. The dispersion curve is quadratic at small $\mathbf{q}$, and for small r_s it was calculated in [2, 3] to be $\varepsilon_{sw}(q) \approx E_c(ql_H)^2$. However, in the opposite limit of large r_s, the spin-wave dispersion is $\varepsilon_{sw} < \omega_H(ql_H)^2/2$ at small $\mathbf{q}$, as we show below.

In a 2D ferromagnet, special topological textures of the spin order parameter field, known as skyrmions, with nontrivial mapping of the entire 2D plane onto the unit sphere of spin directions are allowed [4]. In order to find the energy of such topological excitations, it is necessary to start from the microscopical quantum Hamiltonian for electron spinors, because the phenomenological nonlinear sigma model and its parameters must be derived. Our approach is the same as in [12], where the case of small r_s was considered. However, that publication contains several faults and we repeat briefly the main points here. To establish a procedure for the construction of the electron wave function describing a skyrmion and to calculate its energy, it is useful to introduce a unitary matrix $U(r)$, which rotates the initially uniform spinor field $\chi_{\uparrow}(r)$ at every point of the 2D plane. The Coulomb energy is invariant under any nonuniform rotation $\psi(\mathbf{r}) = U(\mathbf{r})\chi(\mathbf{r})$, because the local density $\rho(\mathbf{r}) = \psi^{+}(\mathbf{r})\psi(\mathbf{r})$ is obviously invariant.

Therefore, the total transformed Hamiltonian takes the form

$$H = \frac{1}{2m}\int \chi^+(\mathbf{r})(-i\boldsymbol{\nabla} + \mathbf{A}(\mathbf{r}) + \boldsymbol{\Omega}(\mathbf{r}))^2\chi(\mathbf{r})d^2\mathbf{r}$$

$$+ \frac{1}{2}\int V(\mathbf{r}-\mathbf{r}')\chi_\alpha^+(\mathbf{r})\chi_\beta^+(\mathbf{r}')\chi_\beta(\mathbf{r})\chi_\alpha(\mathbf{r})d^2\mathbf{r}d^2\mathbf{r}', \quad (15)$$

where the matrix field $\boldsymbol{\Omega}(\mathbf{r}) = -iU^+\boldsymbol{\nabla}U = \boldsymbol{\Omega}^l\sigma^l$ can be expanded in terms of the Pauli matrices σ^l. We consider only the case of a large skyrmion core compared to the magnetic length l_H, i.e., only small gradients of $U(\mathbf{r})$ and small vector functions $\boldsymbol{\Omega}^l$. The main assumption is that it is possible to use, as a leading assumption, perturbation theory in powers of $\boldsymbol{\Omega}(\mathbf{r})$ starting from the ferromagnetic state. Matrix U depends on three Euler angles, and it is topologically nontrivial only if there exists some nonzero winding number for two of its Euler angles. Using the frame with a spin direction at large distances as the z axis, we can parametrize U as three consecutive rotations:

$$U(\alpha, \beta, \gamma) = U_z(\alpha)U_y(\beta)U_z(\gamma),$$

where angles α and γ describe a rotation about the z direction that has the same winding number in the 2D plane, whereas the angle $0 \le \beta \le \pi$ describes a rotation about some perpendicular direction taken to be y. The condition of an identical winding number for α and γ is related to the requirement for matrix U to be nonsingular over the whole 2D plane, which is essential to allow for a perturbation theory in $\boldsymbol{\Omega}$. In this case,

$$\boldsymbol{\Omega}^z = \frac{1}{2}(1 + \cos\beta)\boldsymbol{\nabla}\alpha,$$

$$\boldsymbol{\Omega}^x = \frac{1}{2}(\sin\beta\cos\alpha\boldsymbol{\nabla}\alpha - \sin\alpha\boldsymbol{\nabla}\beta),$$

$$\boldsymbol{\Omega}^y = \frac{1}{2}(\sin\beta\cos\alpha\boldsymbol{\nabla}\alpha + \sin\alpha\boldsymbol{\nabla}\beta).$$

We see that vectors $\boldsymbol{\Omega}^l$ are well defined and smooth, provided point singularities coincide with the points where $\beta(r) = \pi$. At $\mathbf{r} \longrightarrow \infty$, $\beta(r) \longrightarrow 0$; therefore, $U(r)$ is uniquely defined over the entire 2D plane. The nonsingular part of angle $\alpha - \gamma$ is irrelevant, and we set it to be zero. The topological integer invariant is given by

$$Q = \frac{1}{2\pi}\int \boldsymbol{\nabla} \times \boldsymbol{\Omega}^z d^2\mathbf{r}. \quad (16)$$

In this construction, $U(\mathbf{r})$ is defined as an external classical matrix field in the electron Hamiltonian. A complete quantum description of the matrix field $U(\mathbf{r}, t)$ or, equivalently, the skyrmion wave function, is a difficult problem. In quantum field theory, different topological sectors are considered separately without transitions between them [13]. We use this approach assuming that a large skyrmion core makes these transitions improbable. In Hamiltonian (15), $\boldsymbol{\Omega}^z$ and $\boldsymbol{\Omega}^l$ with $l \ne z$ describe

different effects and can be treated separately up to the second order of perturbation theory. This allows us to cast the kinetic part of the Hamiltonian in terms of Ω^l:

$$H = \frac{1}{2m}\int \chi^+(r)[-i\boldsymbol{\nabla} + \mathbf{A}(r) + \boldsymbol{\Omega}^z\sigma_z]^2\chi(r)d^2\mathbf{r}$$

$$+ \frac{1}{m}\sum_{l \ne z}\int \chi^+(\mathbf{r})\boldsymbol{\Omega}^l\sigma_l(-i\boldsymbol{\nabla} + \mathbf{A})\chi(\mathbf{r})d^2\mathbf{r} \quad (17)$$

$$+ \frac{1}{2m}\sum_{l \ne z}\chi^+(\mathbf{r})\chi(\mathbf{r})(\boldsymbol{\Omega}^l)^2d^2\mathbf{r}.$$

We see that $\boldsymbol{\Omega}^z$ defines additional effective vector potential and the corresponding effective magnetic field, which has an opposite sign for the two spin states. Up to the second order in $\boldsymbol{\Omega}^z$, we can consider only the reference ferromagnetic spin-up configuration. Any term in skyrmion the energy can be expanded in gauge invariant terms; therefore, it depends only on $\boldsymbol{\nabla} \times \boldsymbol{\Omega}^z$ and its derivatives. The second term in the kinetic energy can be rewritten in terms of exciton-like creation operators

$$T = \frac{1}{2m}$$

$$\times \sum_{l \ne z}\int \{\Omega_+^l\chi^+(\mathbf{r})\sigma_l\pi^-\chi(\mathbf{r}) + \Omega_-^l(\mathbf{r})\chi^+\sigma_l\pi^+\}\chi(\mathbf{r})d^2\mathbf{r}, \quad (18)$$

where $\Omega_\mp = \Omega_y \pm i\Omega_x$ and

$$\pi^- = \partial/\partial x - i\partial/\partial y + x,$$
$$\pi^+ = -\partial/\partial x - i\partial/\partial y + x. \quad (19)$$

Kinetic term (18) can be expressed in terms of a complicated spin-flip magnetoplasmon exciton—excitation that combines both charge and spin and is created by an operator

$$\Lambda^\pm(0) = \int \psi_\alpha^+(\mathbf{r})\sigma_{\alpha\beta}^\pm\pi_\pm\psi_\beta(\mathbf{r})d^2\mathbf{r}. \quad (20)$$

Operators $\Lambda^\pm(0)$ do not commute with the Coulomb part of the Hamiltonian. Therefore, their dispersion is determined by diagrams with large internal momenta and cannot be found analytically even for small $\mathbf{q}$. Even in the limit $r_s \longrightarrow 0$, any excitation frequency must depend on the kinetic part of the Hamiltonian, because pure potential interaction leads to extreme degeneracy of electron states with zero velocity. Therefore, the energy of these spin-flip magnetoplasmon must include the kinetic part of the Hamiltonian. The proper scale is given by the energy of the Kohn exciton at large $q \sim 1/l_H$: $\Delta_{ex} \sim \sqrt{e^2n_e\sqrt{n_e}/m}$.

In the first order of perturbation theory, there are three terms in QHP energy. The first is

$$\delta E_1 = \frac{1}{2m}\sum_{l \neq z}\int \langle \rho(\mathbf{r})\rangle (\mathbf{\Omega}^l)^2 d^2\mathbf{r}, \tag{21}$$

where $\langle \rho(r)\rangle$ is the ground-state average density, and the other two terms are due to the change of the effective magnetic field; i.e., the local change of cyclotron energy

$$\delta E_H = \frac{1}{m}\sum_{n,p}\left(n + \frac{1}{2}\right)$$
$$\times \int \mathbf{\nabla} \times \mathbf{\Omega}^z \langle 0|\chi_{np}^+(r)\chi_{np}(r)|0\rangle \varphi_{np}^*(r)\varphi_{np}(r) d^2\mathbf{r}, \tag{22}$$

where χ_{np}, χ_{np}^+ are creation operators for the n Ll state, and the correction to the local exchange energy

$$\delta E_{ex} = -\frac{1}{2}\int \frac{\partial E_{ex}}{\partial H}\nabla \times \mathbf{\Omega}^z(r) d^2\mathbf{r}, \tag{23}$$

where $E_{ex}(H)$ is the exchange energy density in a uniform ferromagnetic ground state.

The calculation of the skyrmion energy in the limit of small r_s was done in [12] up to the second order, except for missing correction (23) to the exchange energy. Adding this to the results of [12] in the ease of $\nu = 1$ for the 2D Coulomb interaction gives the skyrmion energy for small r_s:

$$E_{sk} = \sqrt{\frac{\pi}{8}}\frac{e^2}{l_H}(|Q| - 2Q), \tag{24}$$

which coincides with the earlier results of [14, 15].

The main new feature for the case of large r_s appears in the second-order perturbation term in T:

$$\delta E_2 = \langle 0|T\frac{1}{E_0 - H}T|0\rangle; \tag{25}$$

T is connected to spin-flip magnetoplasmon operators (20) with small $\mathbf{q}$ (18), because the Fourier transform of $\Omega^l(\mathbf{r})$ contains only small $\mathbf{q}$. Operator T acts on the ground ferromagnetic state and, therefore, only the term with σ^+ that reverses the spin is essential. For the second-order term, we get the estimate

$$\delta E_2 \approx -\frac{\omega_H^2}{\sqrt{\Delta_{ex}}} \ll \omega_H. \tag{26}$$

Though this contribution is negative and, thus, decreases the skyrmion energy, we can neglect it in the limit of strong Coulomb interaction. We want to emphasize here that in the opposite limit of small r_s this term gives an essential contribution to the total skyrmion energy.

The spin structures of the skyrmion and antiskyrmion are identical except for the sign of the winding number. Therefore, their additional Zeeman and direct Coulomb energies are the same. In the activation energy for the creation of a skyrmion–antiskyrmion pair with opposite topological charges Q and $-Q$, all terms proportional to $\mathbf{\nabla} \times \mathbf{\Omega}^z$ cancel:

$$\Delta_{sk} = E_{sk}(Q) + E_{sk}(-Q)$$
$$= \frac{\nu}{4\pi m}\int(\Omega_x^2 + \Omega_y^2)d^2\mathbf{r} = \nu\omega_H|Q|. \tag{27}$$

The last equality in Eq. (27) holds for a special Belavin–Polyakov ansatz for skyrmion matrix $U(\mathbf{r})$ that minimizes the energy of the QHF. Result (27) coincides with the large r_s extrapolation of the skyrmion energy to the case of small r_s at $\nu = 1$ obtained in [16].

If we consider the nonuniform rotation $U(r)$ with vanishing winding number, we obtain a gradient energy in the nonuniform ferromagnet:

$$\delta E_1 = \frac{\rho}{8m}\iint\left(\frac{\partial \mathbf{n}}{\partial x_k}\right)^2 d^2\mathbf{r} = \frac{1}{16\pi}\nu\omega_H\int\left(\frac{\partial \mathbf{n}}{\partial x_k}\right)^2 d^2\mathbf{r}, \tag{28}$$

where $\mathbf{n} = (\sin\beta\cos\alpha, \sin\beta\sin\alpha, \cos\beta)$ is the unit vector in the direction of local spin. This gradient energy gives the spin-wave dispersion $\omega_{sp} = \omega_H\mathbf{q}^2/2$.

The local electron density is determined by the local magnetic field:

$$\rho(r) = \frac{\nu}{2\pi l_H^2}\left(1 + \mathbf{\nabla} + \mathbf{\Omega}^z \cdot \frac{\mathbf{H}}{H}\right), \tag{29}$$

in accordance with our classification assumption that the density coincides with that for an ideal Fermi gas. Therefore, the electric charge of the skyrmion is

$$q = \frac{e\nu}{2\pi}\int\mathbf{\nabla} \times \mathbf{\Omega}^z d^2\mathbf{r} = e\nu Q, \tag{30}$$

and the activation energy per electron or hole charge is given by $\Delta_{activ} = \omega_H/2$. This quantity is proportional to the magnetic field and is small compared to the Coulomb exchange energy E_c. This is qualitatively in accordance with experimental data for the activation energy. We do not discuss here the mobility of skyrmions, which may qualitatively alter the mechanism behind the experimentally observed activation energy.

REFERENCES

1. *The Quantum Hall Effect*, Ed. by E. R. Prange and S. M. Girvin (Springer-Verlag, New York, 1987; Mir, Moscow, 1989).

2. Yu. A. Bychkov, S. V. Iordanski, and G. M. Eliashberg, Pis'ma Zh. Éksp. Teor. Fiz. **33**, 152 (1981) [JETP Lett. **33**, 143 (1981)].

3. C. Kallin and B. I. Halperin, Phys. Rev. B **30**, 5655 (1984).

4. S. L. Sondhi, A. Kahlrede, S. A. Kivelson, and E. H. Rezai, Phys. Rev. B **47**, 16419 (1993).

5. J. H. Schön, Ch. Kloc, and B. Batllog, Science **288**, 2338 (2000).

6. V. M. Pudalov, S. T. Semenchinski, and V. S. Edelman, Zh. Éksp. Teor. Fiz. **89**, 1870 (1985) [Sov. Phys. JETP **62**, 1079 (1985)].

7. R. Price and S. Das Sarma, Phys. Rev. B **54**, 8033 (1996).

8. A. A. Abrikosov, L. P. Gor'kov, and I. E. Dzyaloshinskii, *Methods of Quantum Field Theory in Statistical Physics* (Fizmatgiz, Moscow, 1962; Dover, New York, 1963).

9. J. M. Luttinger and J. C. Ward, Phys. Rev. **118**, 1417 (1960); J. M. Luttinger, Phys. Rev. **119**, 1153 (1960).

10. G. Volovik, Phys. Rep. **351** (4), 195 (2001).

11. W. Kohn, Phys. Rev. **123**, 1242 (1961).

12. S. V. Iordanski, S. G. Plyasunov, and V. I. Fal'ko, Zh. Éksp. Teor. Fiz. **115**, 716 (1999) [JETP **88**, 392 (1999)].

13. R R. Rajaraman, *Solitons and Instantons: an Introduction to Solitons and Instantons in Quantum Field Theory* (North-Holland, Amsterdam, 1982; Mir, Moscow, 1985).

14. H. A. Fertig, L. Brey, R. Cote, and A. H. MacDonald, Phys. Rev. B **50**, 11018 (1994).

15. Yu. A. Bychkov, T. Maniv, and I. D. Vagner, Phys. Rev. B **53**, 10148 (1995).

16. S. Dickmann, Phys. Rev. B (2002) (in press); cond-mat/0107272.

Zero Modes in a Periodic System of Aharonov–Bohm Solenoids

V. A. Geyler* and E. N. Grishanov**

Mordovian State University, ul. Bol'shevistkaya 68, Saransk, 430000 Russia
* e-mail: geyler@mrsu.ru
** e-mail: grishanovev@mrsu.ru
Received February 21, 2002

The existence of infinitely degenerate zero modes is proved for a quantum-mechanical two-dimensional charged particle with spin 1/2 moving in the field of an infinite system of Aharonov–Bohm solenoids. The condition for appearance of these modes is found and their explicit form is obtained. © *2002 MAIK "Nauka/Interperiodica".*

PACS numbers: 03.65.Ta; 73.40.-c

The nontrivial topological structure of the configuration space is often responsible for the appearance of zero modes (zero-energy bound states) in the energy spectrum of a quantum-mechanical system. Quantum fluctuations caused by the zero modes underlie interesting effects in the quantum field theory [1], cosmic string theory [2], and condensed matter physics (an extensive bibliography can be found in [3]). For a charged particle with spin 1/2 in a localized magnetic field, zero modes were determined by Aharonov and Casher in their familiar work [4]. The methods of that work were extended by Dubrovin and Novikov to the periodic magnetic fields with a regular vector potential, and the explicit form was found for the zero-energy Bloch magnetic states [5]. It is significant that the Aharonov–Casher ansatz also applies to a finite system of infinitely thin Aharonov–Bohm solenoids [6]. One can easily show that no zero modes appear for a single solenoid, but they can appear, at certain fluxes, in a finite system of such solenoids (this situation is analyzed in detail in [7] for a finite number of finite-order pole singularities of the magnetic vector potential). It will be shown below that an infinite system of Aharonov–Bohm solenoids has (even if they are arranged periodically) the infinitely degenerate ground state $E_0 = 0$ at certain values of magnetic fluxes; the corresponding magnetic field may have a uniform component. Clearly, the system with a finite Aharonov–Bohm flux density is the thermodynamic limit of the systems in bounded regions with a given flux density. An example of the system of this type is provided by a quasi-two-dimensional system with columnar defects in a uniform magnetic field directed along the defect axis [8, 9].

The motion of a nonrelativistic charged particle (charge e) with spin 1/2 in the (xy) plane in a magnetic field B directed along the z axis is described by the Pauli Hamiltonian

$$H = \Pi^2 - 2eB\mathbf{s}_z, \qquad (1)$$

where $\Pi = \mathbf{p} - e\mathbf{A}$ and $\mathbf{A}$ is the field vector potential; i.e., $B = \partial_x A_y - \partial_y A_x$. In the two-dimensional case, Hamiltonian (1) is separated into two scalar operators $H^{\pm}$ corresponding to the replacement of the matrix $\mathbf{s}_z$ in Eq. (1) by its eigenvalues $s = \pm 1/2$. The magnetic field B consists of the two components: $B = B^0 + B^{AB}$, where the field B^0 is uniform and B^{AB} is the field of infinitely thin Aharonov–Bohm solenoids passing through the points of some discrete subset Λ in the plane $\mathbf{R}^2$. In this case, the multiply connected region $\mathbf{R}^2/\Lambda$, in which the Aharonov–Bohm field strength is zero, represents the configuration space of the system. We will assume for simplicity that each solenoid creates the same flux Φ^{AB} and denote the number of flux quanta in this flux by θ^{AB}: $\theta^{AB} = \Phi^{AB}/\Phi_0$, where $\Phi_0 = hc/e$. We also restrict ourselves to the case where Λ is a lattice; experimentally, such a situation occurs in the GaAs/AlGaAs heterostructures coated with a film of type-II superconductors [10]. Nevertheless, we note that, after the appropriately corrected formulations, some of the conclusions drawn in this work are valid for a more general case. Below, θ^0 denotes the number of flux quanta per a unit cell of the lattice Λ in the field B^0.

It is convenient to denote the points in the plane as complex coordinates $z = x + iy$. The vector potential $\mathbf{A}^{AB}$ for B^{AB} will be taken in the form $\mathbf{A}^{AB}(z, z^*) = (\mathrm{Im}\,M(z), \mathrm{Re}\,M(z))$, where $M(z)$ is a meromorphic function having only simple poles coinciding with Λ, with all residues of $M(z)$ being equal to $\Phi^{AB}/2\pi$. Indeed, one can easily verify that the equality

$$\partial_x A_y^{AB} - \partial_y A_x^{AB} = \Phi^{AB} \sum_{\lambda \in \Lambda} \delta(z - \lambda)$$

is valid in this case. For B^0, we use the vector potential $\mathbf{A}^0(z, z^*) = (B/2)(\mathrm{Im}\,z^*, \mathrm{Re}\,z^*)$.

Since the potential $\mathbf{A}^{AB}$ is singular if $\Phi^{AB} \neq 0$, Eq. (1) does not uniquely define the self-conjugate operator; to correctly define the operator H, one should specify the boundary conditions at the points of Λ [11]. We avoid the cumbersome mathematics of the operator theory of self-conjugate extensions and introduce, following [4], the operators

$$P_{\pm} = \Pi_x \pm i\Pi_y. \quad (2)$$

The largest domain allowable by formal Eq. (2) will be chosen as the domain $\mathscr{D}_{\pm}$ of operator $P_{\pm}$; namely, we assume that $\mathscr{D}_{\pm}$ consists of all functions f belonging to the Hilbert space $L^2(\mathbf{R}^2)$, for which the generalized function $P_{\pm}f$ defined in the domain $\mathbf{R}^2\backslash\Lambda$ also belongs to $L^2(\mathbf{R}^2)$. Then, the self-conjugate operator

$$H^{\pm} = P_{\pm}^* P_{\pm} \quad (3)$$

becomes correctly defined. Evidently, for smooth functions, whose carrier does not contain any points from Λ, the operator $H^{\pm}$ is defined by the right-hand side of Eq. (1). Note that, for the vector potential without singular points, definition (3) coincides with the conventional mathematical definition of the Schrödinger operator in the presence of a magnetic field [12].

Let us first consider the case $B^0 = 0$. Let $W(z)$ be an entire function having only simple zeros whose set coincides with Λ. Then, one can take $M(z) = \Phi^{AB}W'(z)(2\pi W(z))^{-1}$, where the function W satisfies the equation $\Delta\ln|W(z)| = 2\pi(\Phi^{AB})^{-1}B^{AB}(z, z^*)$. The following conclusion can thus be drawn.

The ground state ψ of the Hamiltonian $H^{\pm}$ has the form

$$\psi(x, y) = |W(x + iy)|^{\mp\theta^{AB}}\phi(x \pm iy), \quad (4)$$

where $\phi(z)$ is an arbitrary function holomorphic in the domain $\mathbf{C}\backslash\Lambda$. Let us take for $W(z)$ the modified Weierstrass σ function $\tilde{\sigma}(z)$ that was introduced by Perelomov in [13]: $\tilde{\sigma}(z) = \exp(-\nu z^2)\sigma(z)$. Here, $\sigma(z)$ is the Weierstrass σ function on the Λ lattice; $\nu = i(4S)^{-1}(\eta_1\omega_2^* - \eta_2\omega_1^*)$, where ω_1 and ω_2 form the basis of the Λ lattice; $S = \mathrm{Im}(\omega_1^*\omega_2)$ is the unit-cell area; $\eta_j = (1/2)\zeta(\omega_j/2)$; and $\zeta(z) = \sigma'(z)/\sigma(z)$ is the Weierstrass ζ function. Note that $\nu = 0$ for the quadratic or hexagonal lattice Λ. Denote $\mu = \pi/2S$; it was proved in [13] that the function $\rho(z, z^*) = \exp(-2\mathrm{Re}(\nu z^2) - \mu zz^*)|\sigma(z)|^2$ is Λ-periodic and, in addition, $|\tilde{\sigma}(z)| \leq C\exp(\mu|z|^2)$ with a certain constant C. One can easily find that, at $0 < \alpha < 1$, the function of the form $|\tilde{\sigma}(z)|^{-2\alpha}p(z)$, where $p(z)$ is an arbitrary polynomial, is integrable in the whole plane C. Let the flux θ^{AB} be noninteger. Denote by N the integral part of θ^{AB}. Substituting $\phi(z) = [\tilde{\sigma}(z)]^N p(z)$ in Eq. (4), one obtains the square integrable function ψ.

Therefore, the Hamiltonian H^+ has the zero mode for any noninteger flux θ^{AB}, and this mode is infinitely degenerate. This conclusion is valid for H^- as well. One can show that, for an integer θ^{AB}, the operator $H^{\pm}$ is unitarily equivalent (as in the case of a single Aharonov–Bohm solenoid) to the free Hamiltonian $H_0 = -(\hbar^2/2m)\Delta$ and, hence, has no zero modes. Indeed, $H_0 = U^*H^{\pm}U$, where U is a unitary operator of multiplication by the function $\exp[\pm i\theta\,\mathrm{Arg}(W(z)|W(z)|^{-1})]$, which is single-valued for an integer θ.

Let us now pass over to the general situation $B^0 \neq 0$. First, we point out the following evident, though important, fact. At $B^0 = 0$, the operators $H^{\pm}$ transform into each other upon changing the direction of the B^{AB} field; in the new situation, the signs of both B components should be changed. Hence, the mutual symmetry of the $H^{\pm}$ operators is absent at a fixed B^0, surely, because the spin direction is locked to the field B^0. Next, without loss of generality, we will take $\theta^0 > 0$. In this case, the zero mode should take the form

$$\psi(x, y) = \exp\left(\mp\frac{\pi\theta^0}{2S}\right)|W(x + iy)|^{\mp\theta^{AB}}\phi(x \pm iy), \quad (5)$$

where $\phi(z)$ is again a holomorphic function in the domain $\mathbf{C}\backslash\Lambda$. As above, we take $W(z) = \tilde{\sigma}(z)$. The operator H^+ has the zero mode for any θ^{AB}. Indeed, all previous considerations hold true for a noninteger θ^{AB}. For an integer θ^{AB} ($\theta^{AB} = N$), we take $\phi(z) = [\tilde{\sigma}(z)]^N p(z)$ to obtain the square integrable ψ function. Clearly, in this case, the $E_0 = 0$ level is infinitely degenerate. Interestingly, the operator H^+ has a bound eigenstate even if the total flux equals zero, i.e., if $\theta^0 + \theta^{AB} = 0$. For the operator H^-, the function $\phi(z^*)$ in Eq. (5) should be taken in the form of the product of a modified Weierstrass function on the Λ^* lattice with the basis ω_2^*, ω_1^* by an arbitrary polynomial of z^*. One thus obtains the following condition for the appearance of the zero mode for a noninteger θ^{AB}: $\theta^0 < 1 - \{\theta^{AB}\}$, where, as usual, the symbol $\{x\}$ denotes the fractional part of x.

Conclusions. In the absence of a uniform magnetic-field component, the periodic system of Aharonov–Bohm solenoids with a noninteger flux θ^{AB} localizes (with an infinite degeneracy) the ground state $E_0 = 0$, irrespective of the direction of electron spin. Such behavior of the spectrum is quite natural for a chaotic or quasi-periodic arrangement of solenoids (Anderson localization). As for the periodic flux system, this phenomenon is analogous to the electron localization at the Landau level in a periodic system of pointlike potentials, which was considered numerically by Ando in [14] and studied analytically in [15–17] (see also review [18]). The ground state remains delocalized in the case of integer flux.

In the presence of a uniform magnetic field B^0 (with θ^0 flux quanta per unit cell), an electron whose spin is opposite to the B^0 direction remains localized (also with an infinite multiplicity) at the $E_0 = 0$ level for any fluxes created by the Aharonov–Bohm solenoids. If the electron spin is parallel to B^0, the periodic system of Aharonov–Bohm solenoids gives rise to an infinitely degenerate zero mode at a rather low B^0. Evidently, the condition $\theta^0 < 1 - \{\theta^{AB}\}$ (the flux θ^{AB} is noninteger) for the appearance of zero modes is periodic in the flux θ^{AB}.

The explicit form of the corresponding modes is given by Eq. (4) or (5).

REFERENCES

1. K. Janssen, Phys. Rep. **273**, 1 (1996).

2. E. Witten, Nucl. Phys. B **249**, 557 (1985).

3. P. W. Brower, E. Racine, A. Furusaki, *et al.*, cond-mat/0201580.

4. Y. Aharonov and A. Casher, Phys. Rev. A **19**, 2461 (1979).

5. B. A. Dubrovin and S. P. Novikov, Zh. Éksp. Teor. Fiz. **79**, 1006 (1980) [Sov. Phys. JETP **52**, 511 (1980)].

6. Y. Aharonov and A. Bohm, Phys. Rev. **115**, 485 (1959).

7. M. Hirokawa and O. Ogurisu, J. Math. Phys. **42**, 3334 (2001).

8. Yu. I. Latyshev, O. Laborde, P. Monceau, *et al.*, Phys. Rev. Lett. **78**, 919 (1997).

9. Yu. I. Latyshev, Usp. Fiz. Nauk **169**, 924 (1999).

10. S. J. Bending, K. von Klitzing, and K. Ploog, Phys. Rev. Lett. **65**, 1060 (1990).

11. S. A. Voropaev and M. Bordag, Zh. Éksp. Teor. Fiz. **105**, 241 (1994) [JETP **78**, 127 (1994)].

12. H. L. Cycon, R. G. Froese, W. Kirsch, and B. Simon, *Schrödinger Operators, with Application to Quantum Mechanics and Global Geometry* (Springer-Verlag, Berlin, 1987; Mir, Moscow, 1990), p. 31.

13. A. M. Perelomov, Teor. Mat. Fiz. **6**, 213 (1971).

14. T. Ando, J. Phys. Soc. Jpn. **52**, 1740 (1983).

15. V. A. Geĭler and V. A. Margulis, Zh. Éksp. Teor. Fiz. **95**, 1134 (1989) [Sov. Phys. JETP **68**, 654 (1989)].

16. M. Ya. Azbel' and B. I. Halperin, Phys. Rev. B **52**, 14098 (1995).

17. Y. Avishai, M. Ya. Azbel', and S. A. Gredesckul, Phys. Rev. B **48**, 17280 (1993).

18. S. A. Gredeskul, M. Zusman, Y. Avishai, *et al.*, Phys. Rep. **288**, 223 (1997).

Translated by V. Sakun

Collapse in the Nonlinear Schrödinger Equation of Critical Dimension {σ = 1, D = 2}

Yu. N. Ovchinnikov[1, 2] and I. M. Sigal[3]

[1] *Max-Planck Institute for Physics of Complex Systems, D-01187 Dresden, Germany*
[2] *Landau Institute for Theoretical Physics, Russian Academy of Sciences, ul. Kosygina 2, Moscow, 117940 Russia*
[3] *Department of Mathematics, University of Toronto, Toronto, Ontario, Canada M5S 3G3*
Received February 27, 2002

Collapsing solutions to the nonlinear Schrödinger equation of critical dimension {σ = 1, D = 2} are analyzed in the adiabatic approximation. A three-parameter set of solutions is obtained for the scale factor $\lambda(t)$. It is shown that the Talanov solution lies on the separatrix between the regions of collapse and convenient expansion. A comparison with numerical solutions indicates that weakly collapsing solutions provide a good initial approximation to the collapse problem. © *2002 MAIK "Nauka/Interperiodica".*

PACS numbers: 02.30.Jr; 03.65.Ge

The nonlinear Schrödinger equation

$$i\frac{\partial \psi}{\partial t} + \Delta \psi + |\psi|^{2\sigma}\psi = 0 \tag{1}$$

in the critical case (σ = 1, D = 2) has various solutions collapsing within a finite time. One of them [exact solution to Eq. (1)] was found by Talanov [1]. The second type of collapsing solutions was obtained by Zakharov [2]. The universal behavior of the solutions of this type is violated only near the collapse point for the appropriately chosen initial data [3, 4] (see also [5, 6]). The region of this violation is very narrow [7, 8]. In the critical case {σ = 1, D = 2}, the third type of solutions (weak collapse) transforms to the second-type solution.

Below, we investigate the behavior of a collapsing solution under the assumption that an adiabatic parameter exists. It will be shown that the measure of realization of the Talanov-type solution is zero. Therefore, the solutions of this type are not realized in a numerical experiment with the initial general-position data.

The tail of a collapsing solution can never be universal. Only a function in the region where it is not too small can be universal. We will demonstrate that the numerical calculation in this region [9] is described with high accuracy by a weakly collapsing solution with a certain choice of free parameters.

1. Adiabatic approach to the collapse. Equation (1) has the stationary solution $\tilde{\psi}$ decreasing exponentially at infinity:

$$\Delta \tilde{\psi} + |\tilde{\psi}|^2 \tilde{\psi} = |E_0|\tilde{\psi}; \quad E_0 < 0, \quad \tilde{\psi} = \tilde{\psi}(|r|). \tag{2}$$

If $\hat{\psi}$ is a solution to Eq. (2), the function

$$\hat{\psi} = \frac{1}{\lambda}\exp\left(\frac{i|E_0|}{\lambda^2}(t - t_0)\right)\tilde{\psi}(\rho/\lambda), \quad \rho = |r|, \tag{3}$$

is also a solution to Eq. (1) for an arbitrary time-independent λ value. This property of Eq. (1) enables us to analyze Eq. (1) using the adiabatic theory (adiabaticity parameter $\lambda\dot{\lambda}$) (see [3–5]). Our aim is to obtain an equation for the parameter λ. In the leading approximation in the adiabaticity parameter, a third-order nonlinear equation for the scale parameter λ will be derived. Equation (1) is first-order in time *t*. Therefore, a solution is completely determined by specifying the function ψ at a fixed instant of time. This statement means that a change in the initial state results in changing the form of the collapsing solution. From this viewpoint, the time dependence of the form $(t_0 - t)^\alpha$ is not universal and depends on the parameters related to the initial form of the function ψ. We will demonstrate that the Talanov solution is a separatrix between the collapse process and the regular development. As a result, the effective measure for this solution is zero, and this solution cannot be obtained by numerical calculation. However, there is a region of initial data that give rise to the compression of the state to a small nonzero size with further expansion.

2. Equation for the scale parameter λ. A solution to Eq. (1) is sought in the form

$$\psi = (\lambda^{-1}\tilde{\psi}(\rho/\lambda) + \psi_1(\rho/\lambda, t))\exp\left(i|E_0|\int^t \frac{dt_1}{\lambda^2(t_1)}\right), \tag{4}$$

where $\lambda \equiv \lambda(t)$ and the function $\tilde{\psi}$ satisfies Eq. (2). Below, we set

$$x = \rho/\lambda. \qquad (5)$$

Substituting Eq. (4) for the function ψ into Eq. (1), we obtain the exact equation

$$\left\{ \frac{1}{x}\frac{\partial}{\partial x}\left(x\frac{\partial}{\partial x}\right)\psi_1 + \psi_1^2(2\psi_1 + \psi_1^*) - |E_0|\psi_1 \right\}$$

$$+ i\lambda^2\frac{\partial\psi_1}{\partial t} - i\lambda\dot{\lambda}x\frac{\partial\psi_1}{\partial x} + \lambda\tilde{\psi}(\psi_1^2 + 2\psi_1\psi_1^*) \qquad (6)$$

$$- \lambda^2\psi_1^2\psi_1^* - i\lambda\dot{\tilde{\psi}} - i\lambda\dot{\lambda}x\frac{\partial\tilde{\psi}}{\partial x} = 0,$$

where

$$\dot{\lambda} = \partial\lambda/\partial t. \qquad (7)$$

We use the adiabatic approximation and consider the parameter $\lambda\dot{\lambda}$ as a small quantity,

$$\lambda\dot{\lambda} \ll 1. \qquad (8)$$

The first-order correction can easily be found. As a result, we obtain the function ψ_1 in the form

$$\psi_1 = i\tilde{\psi}\left(\frac{\dot{\lambda}}{4}x^2 + \beta\right) + \phi + i\psi_3, \qquad (9)$$

where $\beta \equiv \beta(t)$ is an arbitrary function of time t of order $\dot{\lambda}$, ϕ is the real second-order correction, and ψ_3 is the third-order correction. The function ϕ can be found from Eqs. (6) and (9):

$$\phi = \hat{L}^{-1}\left\{ \lambda^2\tilde{\psi}\left(\frac{\ddot{\lambda}}{4}x^2 + \frac{\partial\beta}{\partial t}\right) \right.$$

$$\left. - \lambda\dot{\lambda}x\left(\beta\frac{\partial\tilde{\psi}}{\partial x} + \frac{x\dot{\lambda}}{2}\tilde{\psi} + \frac{\dot{\lambda}x^2}{4}\frac{\partial\tilde{\psi}}{\partial x}\right) - \lambda\left(\frac{\dot{\lambda}}{4}x^2 + \beta\right)^2\tilde{\psi}^3 \right\}, \qquad (10)$$

where the operator $\hat{L}$ is determined by the expression

$$\hat{L} = \frac{1}{x}\frac{\partial}{\partial x}\left(x\frac{\partial}{\partial x}\right) + 3\tilde{\psi}^2 - |E_0|. \qquad (11)$$

The operator

$$\hat{L}_1 = \frac{1}{x}\frac{\partial}{\partial x}\left(x\frac{\partial}{\partial x}\right) + \tilde{\psi}^2 - |E_0| \qquad (12)$$

has zero mode $i\tilde{\psi}$:

$$\hat{L}_1(u\tilde{\psi}) = 0.$$

Therefore, the right-hand side of the equation for ψ_3 must be orthogonal to the function $\tilde{\psi}$. This condition

provides the following equation for the function $\lambda(t)$:

$$\int_0^\infty dx\, x\tilde{\psi}\left\{ \lambda^2\frac{\partial\phi}{\partial t} - \lambda\dot{\lambda}x\frac{\partial\phi}{\partial x} \right.$$

$$\left. + 2\lambda\tilde{\psi}^2\left(\frac{\dot{\lambda}}{4}x^2 + \beta\right)\phi + \lambda^2\tilde{\psi}^3\left(\frac{\dot{\lambda}}{4}x^2 + \beta\right)^3 \right\} = 0. \qquad (13)$$

To simplify this equation, we use the exact equations

$$\hat{L}\left(\frac{\partial}{\partial x}(x\tilde{\psi})\right) = 2|E_0|\tilde{\psi},$$

$$\hat{L}\tilde{\psi} = 2\tilde{\psi}^3, \qquad (14)$$

$$\hat{L}(x^2\tilde{\psi}) = 2x^2\tilde{\psi}^3 + 4\frac{\partial}{\partial x}(x\tilde{\psi}).$$

Using Eqs. (10) and (14), we transform Eq. (13) for λ to a comparatively simple form:

$$\frac{\lambda}{2}\frac{\partial}{\partial t}(\lambda^2\beta^2)\int_0^\infty dx\, x\left(\tilde{\psi}^2 - \frac{1}{2|E_0|}\tilde{\psi}^4\right)$$

$$+ \lambda\frac{\partial}{\partial t}(\lambda^2\dot{\lambda}\beta)\int_0^\infty dx\, x\left\{\frac{3}{4}(x\tilde{\psi})^2 - \frac{1}{2|E_0|}(\tilde{\psi}^2 + x^2\tilde{\psi}^4)\right\}$$

$$+ \frac{1}{32}(\lambda^2\dot{\lambda}^3 + \lambda^3\dot{\lambda}\ddot{\lambda}) \qquad (15)$$

$$\times \left\{ 10\int_0^\infty dx\, x(x^4\tilde{\psi}^2) - \frac{7}{|E_0|}\int_0^\infty dx\, x(x\tilde{\psi})^4 \right\}$$

$$- \frac{1}{|E_0|}\left(\lambda^2\dot{\lambda}^3 + \frac{11}{8}\lambda^3\dot{\lambda}\ddot{\lambda} + \frac{1}{8}\lambda^4\dddot{\lambda}\right)\int_0^\infty dx\, x(x\tilde{\psi})^2 = 0.$$

Equations (14) lead to important integral relationships. The first of Eqs. (14) reduces to the equation

$$\int_0^\infty dx\, x\tilde{\psi}\left\{ \hat{L}\left(\frac{\partial}{\partial x}(x\tilde{\psi})\right) - 2|E_0|\tilde{\psi} \right\} = 0. \qquad (16)$$

With allowance for the second of Eqs. (14), Eq. (16) takes the form

$$\int_0^\infty dx\, x\tilde{\psi}^3\frac{\partial}{\partial x}(x\tilde{\psi}) = |E_0|\int_0^\infty dx\, x\tilde{\psi}^2. \qquad (17)$$

The integration by parts on the left-hand side of Eq. (17) gives the first relationship

$$\int_0^\infty dx\, x\tilde{\psi}^4 = 2|E_0|\int_0^\infty dx\, x\tilde{\psi}^2. \qquad (18)$$

Similarly, using the third of Eqs. (14), we find

$$
2|E_0| \int_0^\infty dx\, x (x^2 \tilde\psi) \frac{\partial}{\partial x}(x\tilde\psi)
$$

$$
= \int_0^\infty dx\, x \left(\frac{\partial}{\partial x}(x\tilde\psi) \right) \left[2x^2 \tilde\psi^3 + 4\frac{\partial}{\partial x}(x\tilde\psi) \right].
$$

(19)

Simple calculations with the use of Eq. (18) give the second relationship

$$
\frac{3}{2}|E_0| \int_0^\infty dx(x\tilde\psi)^2 = \int_0^\infty dx\, x \tilde\psi^2 + \int_0^\infty dx\, x(x^2\tilde\psi^4).
$$

(20)

Equations (18) and (20) mean that the quantity β does not enter into Eq. (15) in the approximation considered. The next substantial simplification of Eq. (15) is achieved by applying the exact relationship

$$
\frac{1}{x}\frac{\partial}{\partial x}\left(x\frac{\partial}{\partial x} \right)(x^4\tilde\psi)
$$

$$
= 16x^2\tilde\psi + 8x^3\frac{\partial\tilde\psi}{\partial x} + x^4(|E_0|\tilde\psi - \tilde\psi^3).
$$

(21)

Multiplying both sides of Eq. (21) by the function $(\partial/\partial x)(x\tilde\psi)$ and integrating with respect to $x\,dx$ over the interval $(0, \infty)$, we arrive at the relationship

$$
10|E_0| \int_0^\infty dx\, x(x^4\tilde\psi^2) - 7\int_0^\infty dx\, x(x\tilde\psi)^4 = 32\int_0^\infty dx(x\tilde\psi)^2.
$$

(22)

Using Eqs. (18), (20), and (22), we transform Eq. (15) for the parameter λ to the final form

$$
\dddot\lambda + 3\dot\lambda\ddot\lambda = 0,
$$

(23)

which can easily be integrated. The first integration reduces Eq. (23) to the following second-order equation with an arbitrary constant C:

$$
\ddot\lambda = C/\lambda^3.
$$

(24)

This equation also has the first integral

$$
\dot\lambda^2 = -C/\lambda^2 + C_1.
$$

(25)

The general solution to Eq. (25) with three arbitrary constants (C, C_1, t^*) has the form

$$
\lambda = [C_1(t^* - t)^2 + C/C_1]^{1/2}.
$$

(26)

For different signs of coefficients $\{C, C_1\}$, expression (26) allows the following types of solutions.

(i) $C > 0$ and $C_1 > 0$. The system is compressed, then reaches a minimum nonzero size, and finally is expanded.

(ii) $C < 0$ and $C_1 > 0$. Collapse arises in a finite time interval.

(iii) $C < 0$ and $C_1 < 0$. Collapse arises after a finite expansion interval.

(iv) $C = 0$. Talanov solution arises; i.e., it is the separatrix between the regions of collapse and expansion. The measure of this event is zero.

3. Weak collapse. In the critical case $\{\sigma = 1, D = 2\}$, Eq. (1) has weakly collapsing solutions. In this case, weakly collapsing solutions coincide with the collapsing solutions with the parameter $\nu = 1/2$ (see [8]). Weakly collapsing solutions have the form [8]

$$
\psi = \frac{1}{\lambda}\varphi(\rho/\lambda)\exp(i\chi),
$$

(27)

where the scale parameter $\lambda \equiv \lambda(t)$ and phase χ are determined as

$$
\lambda = \frac{\sqrt{t_0 - t}}{C}, \quad \chi = -\frac{C_1}{2}\ln(t_0 - t) + \tilde\chi(\rho/\lambda),
$$

(28)

where C and C_1 are constants. The absolute value φ and the phase $\tilde\chi$ are related to the function Z as

$$
\varphi = \sqrt{Z'}/\sqrt{y}, \quad \tilde\chi' = -y/4C^2, \quad y = \rho/\lambda.
$$

(29)

For $\{\sigma = 1, D = 2\}$, the function Z is a solution to the ordinary differential equation

$$
Z''' - \frac{(Z'')^2}{2Z'} + \frac{Z'}{2y^2} + \frac{1}{C^2}\left(\frac{y^2}{8C^2} - C_1 \right)Z' + \frac{2(Z')^2}{y} = 0.
$$

(30)

Setting

$$
Z' = \phi,
$$

(31)

we arrive at the following second-order equation for the function ϕ:

$$
\phi'' - \frac{(\phi')^2}{2\phi} + \frac{\phi}{2y^2} + \frac{1}{C^2}\left(\frac{y^2}{8C^2} - C_1 \right)\phi + \frac{2\phi^2}{y} = 0.
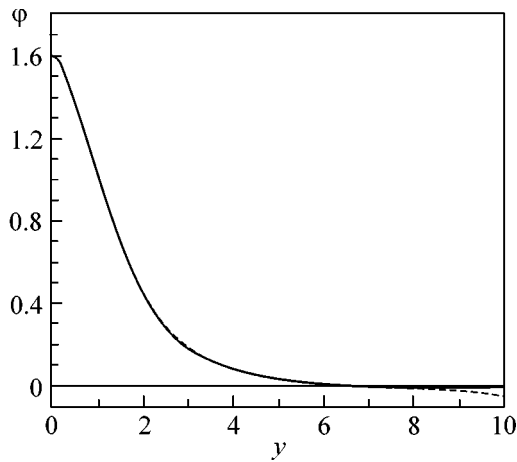$$

(32)

For small y values, this equation gives

$$
\phi = A\left\{ y + \left(\frac{C_1}{4C^2} - \frac{A}{2} \right)y^3 \right.
$$

$$
\left. + \frac{y^5}{128}\left(-\frac{1}{C^4} + \left(\frac{C_1}{C^2} - 2A \right)\left(3\frac{C_1}{C^2} - 10A \right) \right) + \dots \right\}.
$$

(33)

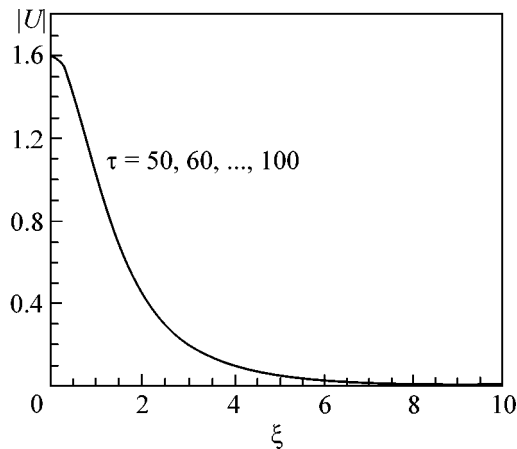For $y \longrightarrow \infty$, the general solution to Eq. (32) is represented as

$$
\phi = B\phi_0\left[1 + \sin\left(\frac{1}{2C^2}\int\frac{dy}{\phi_0} \right) \right] + \phi_1,
$$

(34)

where the function ϕ_0 is the solution to the linear equation

$$
\phi_0''' + \frac{\phi_0'}{y^2} - \frac{\phi_0}{y^3} + \frac{2\phi_0}{C^2}\left(\frac{y^2}{8C^2} - C_1 \right) + \frac{y}{4C^4}\phi_0 = 0,
$$

(35)

Fig. 1. Function φ corresponding to two sets of the parameters $\{A, C, C_1, C_2\}$: the solid line corresponds to $\{A = \varphi^2(0) = 1.6^2, C \longrightarrow \infty, C_2 = -4.0682, C_1/C^2 = 2A + C_2\}$ and the dashed line, to $\{A = 1.6^2, C = 2, C_2 = -4.041, C_1/C^2 = 2A + C_2\}$.

Fig. 2. Profile of the solution $|U|$ obtained numerically in [9] for $|U(0)| = 1.6$ in the interval $(0, 10)$.

which has the following asymptotic behavior at infinity:

$$\phi_0 = \frac{1}{y}\left\{1 + \frac{4C_1C^2}{y^2} + \frac{8C^4(3C_1^3 - 1)}{y^4}\right. \tag{36}$$
$$\left. + \frac{32C_1C^6(5C_1^2 - 7)}{y^6} + \dots\right\}.$$

The function ϕ_1 is small and can be found using the perturbation theory. We do not represent it here.

The substitution

$$\phi = y\varphi^2 \tag{37}$$

reduces Eq. (32) to the following equation describing the collapse with $\nu = 1/2$ [8]:

$$\varphi'' + \frac{\varphi'}{y} + \frac{y^2\varphi}{16C^4} - \frac{C_1}{2C^2}\varphi + \varphi^3 = 0. \tag{38}$$

For $C \longrightarrow \infty$ and the fixed value $\varphi(0)$ [see Eqs. (2), (3)], there is a finite C_2 value such that the function φ decreases exponentially at infinity for $C_1/C^2 = 2A + C_2$. The numerical solution to Eq. (38) gives the following values for parameters $\{\varphi(0), C_2\}$:

$$\varphi(0) = 1.6, \quad C_2 = -4.0682. \tag{39}$$

Figure 1 shows the function φ corresponding to two sets of parameters $\{A, C, C_1, C_2\}$ in the interval $y = [0, 10]$: the solid line corresponds to $\{A = \varphi^2(0) = 1.6^2, C \longrightarrow \infty, C_2 = -4.0682, C_1/C^2 = 2A + C_2\}$ and the dashed line, to the set $\{A = 1.6^2, C = 2, C_2 = -4.041, C_1/C^2 = 2A + C_2\}$.

Figure 2 shows the profile of the solution $|U|$ obtained numerically in [9]. Note that the limiting function φ ($\varphi(C \longrightarrow \infty)$) differs from the function $\lambda(t)$ only for large y values, i.e., in the region where both functions are small and the function $\varphi(C \longrightarrow \infty)$ is not universal. In addition, numerical calculation shows that, when $C \geq 1$, there is a narrow C_2 region (near the point $C_2 = -4.0682$) where the weakly collapsing solution differs only slightly from the limiting function $\varphi(C \longrightarrow \infty)$ at $y < 6$–7. This property can likely be used to construct a multiparameter collapsing solution.

In the adiabatic approximation, we obtained a third-order nonlinear differential equation for the scale factor $\lambda(t)$ determining the time dependence of the solutions to the nonlinear Schrödinger equation. The set of solutions involves a solution collapsing in finite time and solutions corresponding to the compression to a small nonzero size with further expansion. It was shown that the Talanov solution lies on the separatrix between the regions of collapse and convenient regular behavior.

It follows from Eq. (18) that the total energy ϵ of stationary state (2) is zero:

$$\epsilon = \frac{1}{2}\int d^2r\left\{|\nabla\tilde\psi|^2 - \frac{1}{2}|\tilde\psi|^4\right\} = 0.$$

When applying the nonlinear Schrödinger equation with attraction to the problems of solid state physics, one should remember that this equation is approximate and derived under certain assumptions which determine the field of its applicability. In any case, the degree of determined by the parameter $\lambda(t)^{-1}$ cannot be infinitely large and has an upper limit whose value is determined by a specific physical problem.

REFERENCES

1. V. I. Talanov, Pis'ma Zh. Éksp. Teor. Fiz. **11**, 303 (1970) [JETP Lett. **11**, 199 (1971)].

2. V. E. Zakharov, Zh. Éksp. Teor. Fiz. **62**, 1746 (1972) [Sov. Phys. JETP **35**, 908 (1972)].

3. G. M. Fraiman, Zh. Éksp. Teor. Fiz. **88**, 390 (1985) [Sov. Phys. JETP **61**, 228 (1985)].

4. M. J. Landman, G. C. Papanicolaou, C. Sulem, and P. L. Sulem, Phys. Rev. A **38**, 3837 (1988).

5. A. I. Smirnov and G. M. Fraiman, Physica D (Amsterdam) **52**, 2 (1991).

6. D. Pelinovskii, Physica D (Amsterdam) **119**, 301 (1998).

7. G. Perelman, in *Nonlinear Dynamics and Renormalization Group*, Ed. by I. M. Sigal and C. Sulem (American Mathematical Society, Providence, 2001), CRM Proceedings and Lecture Notes, Vol. 27, p. 147.

8. Yu. N. Ovchinnikov and I. M. Sigal, Zh. Éksp. Teor. Fiz. **116**, 67 (1999) [JETP **89**, 35 (1999)].

9. Catherine Sulem and Pierre-Louis Sulem, *The Nonlinear Schrödinger Equation: Self-Focusing and Wave Collapse* (Springer-Verlag, New York, 1999).

Translated by R. Tyapaev